Multi-cue image integration for cardiac tissue characterization

Antonio Reyes Porras Pérez

TESI DOCTORAL UPF / 2015

Directors: Dr. Gemma Piella
Prof. Alejandro F. Frangi

Departament de Tecnologies de la Informació i les Comunicacions
Universitat Pompeu Fabra

Directors:

Dr. Gemma Piella	Associate Professor Universitat Pompeu Fabra, Barcelona, Spain
Prof. Alejandro F. Frangi	Professor of Biomedical Image Computing University of Sheffield, Sheffield, United Kingdom

Review Committee (Main):

Prof. Daniel Rückert	Imperial College London
Prof. Miguel Ángel González	Universitat Pompeu Fabra
Dr. Manuel Desco	Universidad Carlos III de Madrid

Review Committee (Reserve):

Prof. Ferrán Marqués	Universitat Politècnica de Catanlunya
Dr. Noemí Carranza	Centre for Genomic Regulation

This work was carried out in the *Departament de Tecnologies de la Informació i les Comunicacions* at the *Universitat Pompeu Fabra*, Barcelona, Spain. This work was supported by the Spanish Government with a *Beca de Formación de Profesorado Universitario* (AP2010-3684).

"The future has many names: For the weak, it means the unattainable. For the fearful, it means the unknown. For the courageous, it means opportunity"

Victor Hugo

Abstract / Resumen

Abstract:

Cardiovascular diseases are the main cause of death in the western world. A complete and accurate characterization of the heart is essential to help diagnosing and treating any potential problems. To characterize cardiac function from different perspectives, large amounts of data of different nature are often acquired in clinical practice from the same patient, thus providing complementary information that is useful for heart assessment.

Cardiac motion analysis has proven to be helpful for cardiac function assessment. It can be estimated and quantified non-invasively using several imaging techniques and, among all of them, ultrasound imaging is the most used. With this technique, different types of images, such as B-mode and tissue Doppler, are normally acquired for cardiac motion assessment. Since all of them provide different information, cardiac motion analysis is normally performed independently from each of them.

Beside motion information, electrical data acquired using either non-invasive (electrocardiography) or minimally invasive techniques (electro-anatomical mapping) are often used to assess cardiac activation. In the latter case, electrical information is acquired intra-operatively and the possibility of using it together with other types of information is constrained by the compatibility between the different instruments and devices. Pre-operative information can also be used to guide the intervention, but this information is not updated after any change that might occur during the procedure.

Although the different data obtained from each patient are often analyzed separately to assess cardiac function from different perspectives, the effective combination of this heterogeneous information may be useful for a better insight into the heart's anatomy and function. The main objective of this thesis is to develop methods to integrate information of different nature for a more accurate and complete cardiac tissue characterization. The contributions of this work can be summarized as: (1) the development of a method to integrate B-mode and tissue Doppler ultrasound information for an accurate estimation and quantification of cardiac motion, (2) the extension of this methodology to use multi-plane information to assess motion in the whole left ventricle, (3) the development of a method to estimate cardiac motion intra-operatively using electro-anatomical mapping information, and (4) the implementation of a framework that integrates tissue viability information with intra-operative motion and electophysiological information for cardiac tissue characterization. Each of these contributions has led to an article submitted or published in a peer-reviewed international journal.

Resumen:

Las enfermedades cardiovasculares son la principal causa de muerte en el mundo occidental. Una caracterización completa y precisa del corazón es esencial para ayudar en el diagnóstico y tratamiento de problemas potenciales. Para caracterizar la función cardíaca desde diferentes perspectivas, en la práctica clínica, se adquieren grandes cantidades de datos de distinta naturaleza sobre un mismo paciente, proporcionando información útil para la evaluación del corazón.

El análisis del movimiento del corazón ha demostrado ser útil para la evaluación de la función cardíaca. Se puede estimar y cuantificar de manera no invasiva utilizando varias técnicas de adquisición de imagen y, entre todas ellas, la imagen por ultrasonidos es la más utilizada. Con esta técnica, distintos tipos de imágenes, como B-mode y Doppler tisular, se adquieren normalmente para evaluar el movimiento cardíaco. Como todas proporcionan información diferente, el análisis del movimiento cardíaco se suele realizar de forma independiente a partir de cada una de ellas.

A parte de la información de movimiento, los datos eléctricos adquiridos utilizando técnicas no invasivas (electrocardiografía) o mínimamente invasivas (mapeo electro-anatómico) se suelen utilizar para evaluar la activación cardíaca. En el segundo caso, la información eléctrica se adquiere de forma intra-operatoria y la posibilidad de utilizarla junto con otros tipos de información está restringida por la compatibilidad entre los distintos instrumentos y dispositivos. También se puede utilizar información pre-operatoria para guiar la intervención, pero esta información no se actualiza tras cualquier cambio que se pueda producir durante el procedimiento.

Aunque los distintos datos obtenidos de cada paciente se suelen analizar por separado para evaluar la función cardíaca desde diferentes perspectivas, la combinación efectiva de esta información heterogénea podría ser útil para tener una mejor visión de la anatomía y la función cardíaca. El objetivo principal de esta tesis es el desarrollo de métodos para integrar información de distinta naturaleza para una caracterización del tejido cardíaco más completa y precisa. Las contribuciones de este trabajo se pueden resumir en: (1) el desarrollo de un método para integrar información de imágenes de ultrasonidos B-mode y Doppler tisular para una estimación y cuantifición precisa del movimiento cardíaco, (2) la extensión de esta metodología utilizando información multi-plano para evaluar el movimiento en todo el ventrículo izquierdo, (3) el desarrollo de un método para estimar el movimiento cardíaco de forma intra-operatoria utilizando información de mapeo electro-anatómico, y (4) la implementación un marco donde se integran información de viabilidad del tejido con información electrofisiológica y de movimiento intra-operatoria para la caracterización del tejido cardíaco. Cada una de estas contribuciones representa un artículo enviado o publicado en una revista internacional con revisión de expertos.

Contents

List of Figures

List of Tables

List of acronyms

DE-MR	Delayed-Enhancement Magnetic Resonance
EAM	Electro-Anatomical Map
EAMS	Electro-Anatomical Mapping System
ECG	Electrocardiogram
IC	Ischemic Cardiomyopathy
ICP	Iterative Closest Point
LBFGS-B	Limited memory Broyden-Fletcher-Goldfarb-Shannon with simple Bounds
MR	Magnetic Resonance
PDM	Point Distribution Model
PRF	Pulse Repetition Frequency
SOFA	Simulation Open Framework Architecture
TD	Tissue Doppler
TDFFD	Temporal Diffeomorphic Free Form Deformation
US	Ultrasound
VT	Ventricular Tachycardia

Preface

This thesis would not have been possible without the support of many people. First, I would like to thank my supervisors, Gemma Piella and Alejandro Frangi, for offering me the opportunity to work in such a good research environment. I would also like to express my gratitude for their guidance and financial support during these years.

I would like to thank all the people who have been part of the CISTIB and SIMBioSys research groups. In particular, Mathieu de Craene and Nicolas Duchateau, for making everything easier for me and for their valuable scientific support. I also want to thank to the PMO team for their administrative support, and the developers team for creating such a good software framework that facilitated my work.

I would like to express my gratitude to Prof. Jan D'hooge, who gave me the opportunity to have a three-months research stay at the Laboratory of Cardiovascular Imaging and Dynamics, K. U. Leuven, Belgium. Special mention to all members of the Medical Imaging Research Center and, in particular, I would like to thank Martino Alessandrini for his availability and good work.

Then to my friends Xènia and Veronika for the many hours of conversations that were of great help in the not-so-good moments. I also appreciate the support of my other friends in the department and the "Tampa" people for those many good moments.

Finally, I want to express my gratitude to the very nice people I found in Barcelona and who, even though were not directly involved in my thesis, gave me the personal support I needed during these years, specially David, Eva and Carlos.

CHAPTER 1

Introduction

1.1 The heart

The heart is a muscular organ located in the thoracic cavity that acts as a pump, making the blood flow through the circulatory system. It is enclosed in the pericardium, which constitutes a sac with a small amount of fluid with the objective of protecting the heart.

The heart contains four different cavities, two atria and two ventricles, as represented in Figure 1.1. The deoxygenated blood from all organs but the lungs, called systemic circulation, comes into the right atrium through the vena cava. This blood is ejected to the right ventricle, which pumps it to the lungs to be oxygenated. The left atrium gathers the oxygenated blood from the lungs through the pulmonary veins and pumps it into the left ventricle. This ejects the blood to the rest of the organs through the aorta. As the cardiac cells need to be supplied oxygen and nutrients, there is also a coronary circulation to this end. In particular, the left and right coronary arteries supply the left and right parts of the heart, respectively.

The cardiac wall is divided into three layers. The inner layer is the endocardium and is composed mainly by endothelial cells that protect the cardiac chambers. The next layer is the myocardium, which is composed by cardiomyocites. The coordinated activation of these cardiac cells is what makes the heart contract and pump the blood out. Finally, the outer layer is called epicardium. It is composed by connective tissue and provides an outer protective layer for the myocardium.

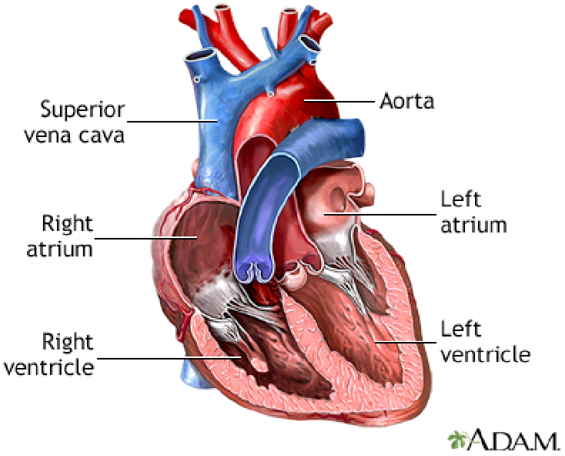

Figure 1.1: Heart anatomy. The four chambers and the main vessels are represented. [1]

---

[1] Source: MedlinePlus.gov. Retrieved 03 Feb. 2015 from http://www.mybwmc.org/library/2/19612.

1.1.1 Electrical conduction system

As previously indicated, the synchronous activation of the cardiomyocites is what makes the cardiac wall contract. Since the heart needs to pump blood periodically, there must be a periodical activation of those cells. The electrical conduction system of the heart, represented in Figure 1.2, is responsible for this activation.

The sinoatrial node is a tissue located at the right atrium that is able to generate the electrical impulse as a physiological pacemaker. The generated impulse is propagated to the rest of the right atrium and through the Bachmann's bundle to the left atrium, thus producing the activation of both atria.

The atrioventricular node is located at the top of the ventricles. It produces a delayed activation of the ventricles with respect to the atria, which is essential for an efficient blood ejection. The bundle of His is a part of this node that splits at septal level into the right and left bundle branches, which are responsible of the activation of the right and left ventricles, respectively. In particular, these branches are connected to the Purkinje fibers, conducting the electrical impulse to different groups of cells in the ventricles.

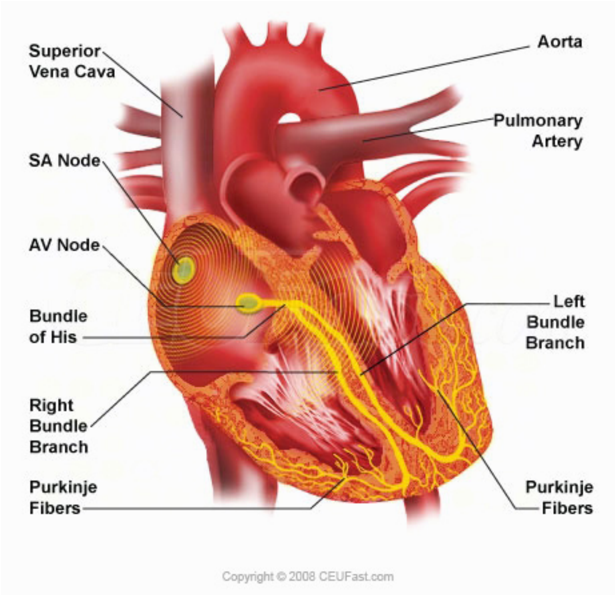

Figure 1.2: Electrical conduction system of the heart. [2]

---

[2] Source: CEUfast.com. Retrieved 03 Feb. 2015 from http://www.ceufast.com/courses/viewcourse.asp?id=239.

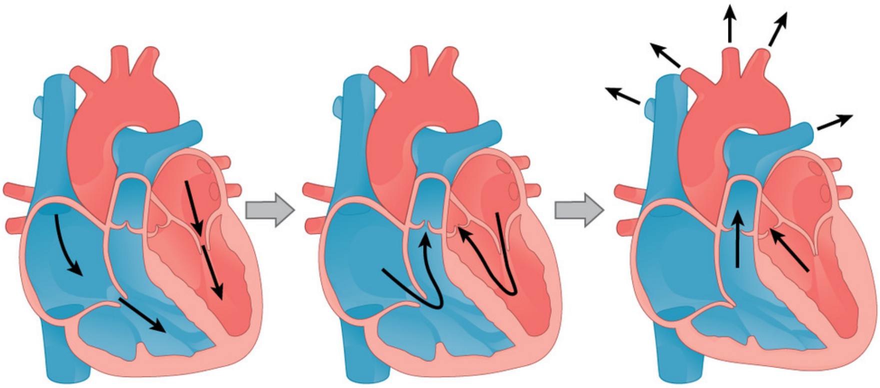

(a) Cardiac diastole: all chambers are relaxed, and blood flows into the heart.

(b) Atrial systole, ventricular diastole: atria contract, pushing blood into the ventricles.

(c) Atrial diastole, ventricular systole: after the atria relax, the ventricles contract, pushing blood out of the heart.

Figure 1.3: The three main stages of the cardiac cycle. [3]

1.1.2 Contraction during the cardiac cycle

Cardiac activation, contraction and relaxation in a healthy heart is periodical. Figure 1.3 shows the three main stages of the cardiac cycle. Taking as a reference the instant when the ventricles are contracted and the blood is ejected, the cycle starts with the relaxation of the ventricles and the opening of the valves separating them from the atria. The difference of pressure between the atria and the ventricles produces the blood filling of the ventricles as they relax. The subsequent atrial contraction ejects most of the remaining blood in the atria to the ventricles. At ventricle activation, the tricuspid and mitral valves, which separate the ventricles and the atria, close. The pressure increase in the ventricles produces the opening of the aortic and the pulmonary valves and the ejection of the blood to the circulatory system. In addition, the blood from the circulatory system also comes into the atria as they relax.

1.2 Quantification of cardiac motion

The main goal of the heart is to pump blood to provide oxygen and nutrients to the rest of the body, so it must be able to eject the blood volume the body needs to work. The stroke volume depends on the way the heart contracts, which in turn depends on its electrical activation. Therefore, studying

---

[3] Source: “The Cardiac Cycle.” Boundless Biology. Boundless, 14 Nov. 2014. Retrieved 03 Feb. 2015 from https://www.boundless.com/biology/textbooks/boundless-biology-textbook/the-circulatory-system-40/mammalian-heart-and-blood-vessels-226/the-cardiac-cycle-852-12097/.

cardiac motion provides insight into cardiac function [1].

Cardiac motion assessment is normally done non-invasively from image data. Among the different available techniques (magnetic resonance, computed tomography...), ultrasound (US) imaging is the most used because of its low cost, non-invasiveness and good temporal resolution. From echocardiographic images, it is possible to estimate different local and global parameters for heart assessment.

The ejection fraction is used to globally assess ventricle function and it is defined as the fraction of the volume of blood contained in the relaxed ventricle (end diastole) that is ejected after contraction (end systole). It can be estimated using M-mode images [2], 2D images [3] and 3D images [4]. This parameter gives information about the cardiac output, but not about how the heart produces this output.

For a deeper insight on cardiac mechanics, different parameters giving local information about heart contraction are used. The displacement of a specific point in the cardiac wall can be estimated by tracking 2D or 3D gray-scale echocardiographic images. The velocity can also be estimated using Tissue Doppler (TD) images, but only its component on the US beam direction [5]. The deformation can be estimated by calculating the strain, which gives information about how neighboring points in the cardiac wall change their position with respect to each other. Finally, the strain rate is the velocity at which the strain changes in time. Figure 1.4 represents the relation between these four parameters.

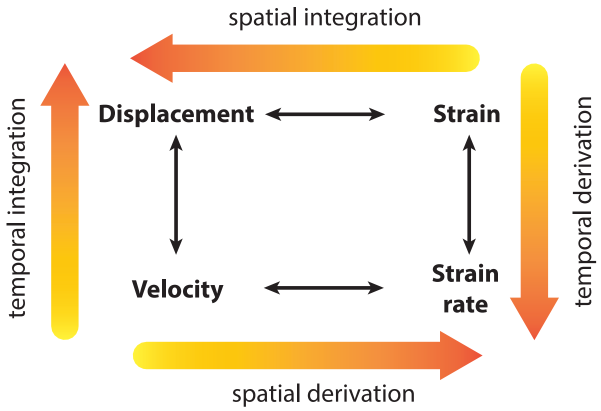

Figure 1.4: Parameters for motion quantification. The scheme shows the spatial and temporal relations between displacement, strain, strain rate and velocity.

1.2.1 Ultrasound imaging modalities

Theoretically, knowing one of the parameters from Figure 1.4, it is possible to estimate the others. However, the accuracy in the estimation of any of them is compromised by the limitations of the acquisition system and the spatial and temporal resolution of the acquired data. In particular, in US imaging, there is always a tradeoff between spatial and temporal resolution, so increasing one of them is done at the expense of reducing the other one.

2D B-mode echocardiographic images have been used for heart motion assessment by tracking the speckles in the image sequence. However, there are some problems that are intrinsic to the image nature, as the presence of artifacts, reverberations, curvature dependency and the limited spatiotemporal resolution [6]. In addition, it is necessary to consider that the motion estimation is dependent on the tracking method used.

2D TD images, on the other hand, measure the projection of the real velocity of the structures imaged on the beam direction. However, problems like the presence of random noise and aliasing are also present in this imaging modality.

Technical advances during the last years have allowed for the acquisition of 3D gray-scale US images. With this approach, small volumetric information is acquired during consecutive cardiac cycles. Then, all the acquired information is integrated for the reconstruction of the whole 3D volume. However, the spatial and temporal resolution of the acquired information is low in comparison with the resolution of 2D US data. In addition, since information from different beats is integrated, its interpretation from patients presenting unstable heart rhythms is challenging [7].

1.3 Integration of information for heart assessment

In clinical practice, large volumes of information from different nature are normally obtained from the same patient. Most of the data acquired are often used separately to assess cardiac function. Since the data from different sources provide complementary information, the integration of these heterogeneous data may be useful to have a better insight into cardiac function.

Methods fusing cardiac US images to produce another image with higher quality that improved image analysis were proposed in several papers [8, 9]. In other approaches [10, 11, 12], the data from different images, which were not necessarily from the same nature, were directly used together to quantify cardiac motion. However, the combination of different information is still challenging, since the different images normally present different spatiotemporal resolutions, provide complementary information and may lead to inconsistencies.

In the particular case of US imaging, B-mode and TD images are the most used techniques to assess cardiac motion. The combination of the information provided by each modality should let overcoming the drawbacks of using each of them separately. In [13], TD images are used for tracking along the US beam, while speckle tracking from B-mode images is used for tracking transverse to the US beam. Another approach is the simultaneous analysis of B-mode and TD images proposed in [14] where they estimate a 2D velocity field using a spatial affine velocity model inside a sliding window.

In many cases, mechanical abnormalities are directly related to electrophysiological problems. However, local electrophysiological information cannot be obtained directly by using non-invasive imaging techniques, so other approaches are needed. Electro-Anatomical Mapping Systems (EAMS) are used in clinical practice as a minimally invasive technique to record local electrical information from the cardiac wall. The integration of the recorded electrical activity with mechanical information from the heart would provide a more complete characterization of the myocardial tissue. The possibility of estimating mechanical information using an EAMS and its potential applications has been explored in [15, 16, 17, 18, 19].

Beyond mechanical and electrical assessment, tissue viability information is also considered to diagnose and treat different cardiomyopathies. In particular, images from Delayed-Enhancement Magnetic Resonance (DE-MR) are acquired to identify injured areas in the myocardium. The administration of a contrast agent (i.e., gadolinium) results in its uptake into normal and injured myocardium. While in the normal myocardium there is an early washout of the contrast agent, it is slower in injured myocardium. This is translated into images where non-healthy tissue is depicted as areas with high signal intensity, while healthy myocardium presents low signal intensity.

1.4 Objective of the thesis

The global aim of this thesis was to integrate different types of images and information for a better cardiac tissue characterization. This was structured in:

- Development of a method to integrate information from different US image modalities for an accurate assessment of cardiac motion. In particular, B-mode and tissue Doppler ultrasound images were integrated, thus minimizing the drawbacks of using each of them separately.

- Development of a method to integrate intra-operatively electrical and motion information for cardiac tissue characterization.
- Development of a framework to integrate tissue viability, electrical and motion information for a more complete cardiac tissue characterization.

1.5 Contributions of this thesis

This thesis presents four main contributions, with one chapter dedicated to each contribution:

- Chapter 2 presents a diffeomorphic registration framework that integrates 2D B-mode and TD images for an improved cardiac motion estimation. The continuous representation of the transformation both in time and space allows considering each type of information at the location and time it is acquired. Increased accuracy is achieved compared to using a single modality.
- Chapter 3 builds on the previous framework to integrate multi-plane B-mode and TD images for simultaneous motion estimation in the whole left ventricle. This is useful for an accurate motion analysis in the ventricle in those cases where a useful 3D US image cannot be acquired. In addition, it incorporates the use of quantitative information (i.e., Doppler velocities) for motion estimation, which is not available in 3D US imaging.
- Chapter 4 presents a method to estimate cardiac motion intra-operatively using catheter position information from an EAMS to help decision making during catheter-guided interventions.
- Chapter 5 uses the previous method to estimate cardiac motion from EAMS data and integrates it with electrophysiological and DE-MR information for catheter ablation planning and guidance.

Each of these 4 chapters is self-contained and is an adaptation of articles that are published or submitted to peer-reviewed journals. Therefore, some of the concepts introduced in this chapter may be repeated or reformulated according to the particular interests of each chapter.

CHAPTER **2**

Improved myocardial motion estimation combining tissue Doppler and B-mode echocardiographic images

This chapter presents a technique for myocardial motion estimation based on image registration using both B-mode echocardiographic images and tissue Doppler sequences acquired interleaved. The velocity field is modeled continuously using B-splines and the spatiotemporal transformation is constrained to be diffeomorphic. A comparison between using polar and Cartesian transformation models is performed. The proposed dissimilarity measure penalizes the disagreement between tissue Doppler velocities and the estimated velocity field. In addition, a measure including speckle statistics to track motion in the B-mode sequence is tested against using a more traditional mean-squared-error-based measure. Registration accuracy is evaluated and compared to other alternatives using a realistic synthetic dataset, obtaining mean displacement errors of about 1 mm. Finally, the method is demonstrated on data acquired from 6 volunteers, both at rest and during exercise. Results show that our method provides a robust motion estimate in cases with low image quality and reduced number of frames due to fast heart rates.

The content of this chapter is adapted from the following publication:

A. R. Porras, M. Alessandrini, M. De Craene, N. Duchateau, M. Sitges, B. H. Bijnens, H. Delingette, M. Sermesant, J. D’hooge, A. F. Frangi, and G. Piella. Improved myocardial motion estimation combining tissue Doppler and B-mode echocardiographic images. IEEE Transactions on Medical Imaging, vol. 33, no. 11, pp. 2098-2106. 2014.

2.1 Introduction

As introduced in Section 1.2, quantification of cardiac motion and strain has proven to be helpful for cardiac function assessment, providing information on how a given pathology affects global and local mechanics of the myocardium [1, 5, 20]. Among the different imaging techniques available to quantify cardiac motion, US imaging is one of the most used, since it captures a large range of information (e.g., valve flows and tissue velocities) dynamically and at a reasonable cost. Novel trends in the acquisition process, as the use of shear waves [21] and ultrafast imaging through planar waves [22], are believed to lead to significant improvements in spatiotemporal resolution. These advances will also enrich the spectrum of functional information that can be captured by this modality.

Many approaches for tracking anatomical structures in B-mode echocardiography were proposed during the last years. Speckle-tracking-based approaches [23] use block matching algorithms to track local speckle patterns along US sequences under the assumption that they are stable between consecutive frames. These algorithms do not make use of the temporal information in the whole image sequence and may require regularizations, which are performed in post-processing steps.

Several image registration approaches were explicitly designed as spatiotemporal registration schemes [24, 25, 26]. In these papers, temporal continuity of displacements is guaranteed. However, since the displacement at a given time instant does not functionally depend on the displacement at previous time instants, the temporal continuity of the recovered velocity is not guaranteed. To overcome this limitation, a transformation based on the velocity field was proposed in [27], calculating displacements by integrating velocities at all previous time instants. To preserve the topology and orientation of the anatomical structures, the transformation was constrained to be diffeomorphic (smooth, invertible and with smooth inverse) [28]. An additional regularization term minimizing the compressibility of the myocardium was also added to the cost function. Other approaches to guide and constrain cardiac tracking including shape information were proposed in [29, 30, 31].

Complementary to B-mode echocardiographic images, TD imaging is widely used in clinical practice. It allows an objective quantification of true tissue velocities with normally higher temporal resolution than B-mode and better signal-to-noise ratio [5]. Estimating a displacement field from TD data can be done by temporally integrating the measured velocities. However, only the projection of the velocity along the beam direction is available and, due to the low spatial resolution of TD images, local changes may not be captured. In addition, the noise present in the images is accumulated at each integration step, possibly leading to strong drift artifacts.

Some approaches have been proposed to overcome the problems of each technique by using both B-mode and TD images together for a better quantification of heart motion. In [13], TD information was used to track heart motion along the beam direction, while B-mode sequences were used to track in the direction perpendicular to the beam. These two components were estimated separately and no additional regularization was performed. In [14], an optical flow based registration method was proposed, modeling the velocity using a spatial affine model. Registration was performed considering pairs of frames, so temporal coherence was not guaranteed. Furthermore, the evaluated B-mode and TD frames had to coincide in time. Therefore, either temporal interpolation of the B-mode sequence was necessary or TD frames had to be discarded, thus losing temporal resolution. A similar optical flow based method was also presented in [32]. Recently, some authors have introduced the possibility of estimating tissue velocities in two directions using transverse oscillation images [33, 34], although this technique is not yet ready for clinical use.

In this chapter, a registration framework that takes into account both B-mode images and TD velocities, acquired interleaved with the same probe, is proposed to calculate a single continuous spatiotemporal diffeomorphic transformation. In this case, TD sequences and B-mode data coincide in space, so no further spatial alignment is required.

In the proposed approach, the velocity field was modeled continuously using B-spline kernels. All frames were registered simultaneously by estimating a single spatiotemporal transformation to preserve both spatial and temporal consistency, as in [27]. To estimate this transformation, the agreement between the velocity field estimated projected on the beam direction and the velocities obtained from TD images was measured. Moreover, an image dissimilarity measure to track anatomical structures in the B-mode sequence was used. In our implementation, the estimated transformation was constrained to be diffeomorphic, thus being smooth, invertible and with smooth inverse at every spatiotemporal location.

The proposed method was validated using a realistic US simulator and the performance of different image dissimilarity measures was tested. In addition, the feasibility of using the current method for clinical cases was also shown. Stress echocardiography aims at understanding the relation between cardiac function and functional capacity during effort [35, 36]. In this protocol, image quality and temporal resolution may be low. The robustness of our method in this clinical setting was demonstrated. Results obtained with the proposed method were compared to results using only B-mode images. Our method allowed estimating a realistic motion field in cases where tracking using one modality failed due to the quality of the data

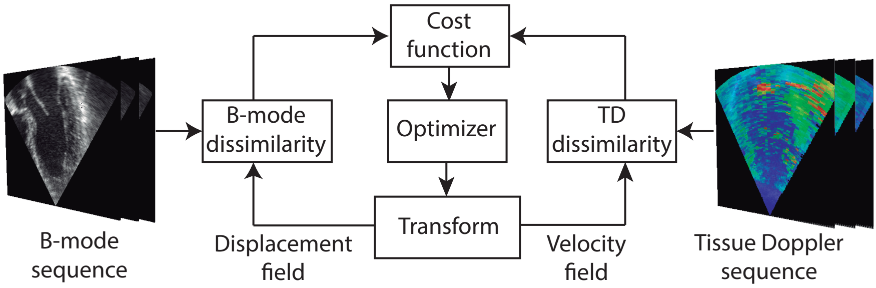

Figure 2.1: Registration scheme. The optimizer finds the optimal parameters of the transformation by combining a pixel intensity based dissimilarity and a measure of the disagreement between the estimated velocities projected on the beam direction and the ones obtained from TD images.

from this protocol.

2.2 Methodology

A basic scheme describing the proposed methodology is shown in Figure 2.1. In the following sections, each component in the registration scheme is described.

2.2.1 The transformation

The proposed approach models the velocity field continuously in time and space using B-spline kernels, as proposed in [27]:

$$\mathbf{v}(\mathbf{x},t;\mathbf{p}) = \sum_{i,j,k} B\left(\frac{x-q^i}{\Delta^i}\right) B\left(\frac{y-q^j}{\Delta^j}\right) B\left(\frac{t-q^k}{\Delta^k}\right) \mathbf{p}^{i,j,k}, \tag{2.1}$$

where $\mathbf{x} = (x,y)$ are the spatial coordinates of the point whose velocity is evaluated, $B(\cdot)$ is a cubic B-spline kernel function, $\mathbf{Q} = \left(q^i, q^j, q^k\right)$ represents the grid of uniformly spaced control points, $\Delta = \left(\Delta^i, \Delta^j, \Delta^k\right)$ are the spacings between control points, and $\mathbf{p}$ is a vector containing the B-spline coefficients, which correspond to the velocities associated to each control point.

To map a point from $t = t_0$ to a time instant $t = T$, it is then necessary to integrate the velocity field:

$$\varphi_{t_0}(\mathbf{x},T;\mathbf{p}) = \mathbf{x} + \int_{t_0}^{T} \mathbf{v}\big(\varphi_{t_0}(\mathbf{x},t;\mathbf{p}),t;\mathbf{p}\big)dt. \tag{2.2}$$

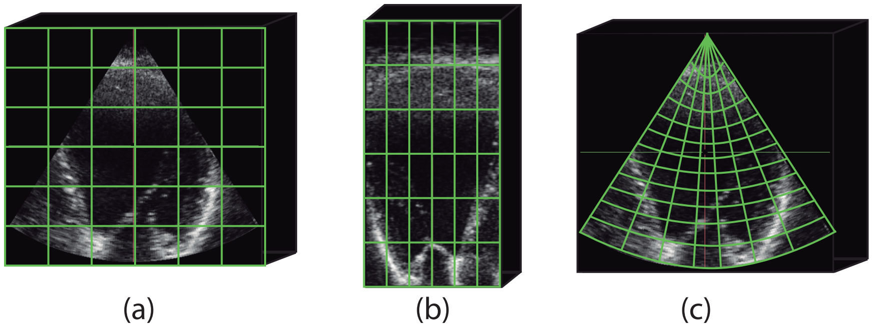

Figure 2.2: Grid topology. (a) Grid of control points in Cartesian coordinates. (b) Grid of control points in polar coordinates. (c) Representation of the image from (b) in Cartesian coordinates.

To compute the integral in Equation 2.2, a forward Euler integration scheme was used. Thus, the transformation was approximated by:

$$\varphi_{t_0}(\mathbf{x},t_n;\mathbf{p}) = \mathbf{x} + \sum_{k=0}^{n-1} \mathbf{v}\big(\varphi_{t_0}(\mathbf{x},t_k;\mathbf{p}),t_k;\mathbf{p}\big)\Delta t_k, \tag{2.3}$$

where $\Delta t_k = t_{k+1} - t_k$.

With this approach, the temporal sampling used to approximate the integration of the velocity field has to be small enough for a good estimation of the trajectory. In [27], a time interval of $1/2$ the spacing between B-mode frames was found to be small enough. In our implementation, it was reduced to $1/4$ the temporal spacing between consecutive TD frames to increase the accuracy when estimating displacements. To ensure invertibility of the transformation, the determinant of its spatial Jacobian was constrained to be positive. To achieve this, if a negative value was detected, the temporal sampling was divided by a factor of 2 until no negative values were found [27].

Grid topology

Most of the B-spline based image tracking methods use a Cartesian grid on the US images, as shown in Figure 2.2(a). However, the acquisition of echocardiography images is performed in polar coordinates. For this reason, we compared the use of a Cartesian grid with a polar one, as in Figure 2.2(b). Setting a grid in polar coordinates allows processing images before scan conversion, thus avoiding unnecessary interpolations. As it can be observed in Figure 2.2, while the Cartesian spacing between control points in a Cartesian grid is uniform, the Cartesian spacing between polar control points increases with their distance to the transducer at the origin of the field of view.

2.2.2 The dissimilarity measure

Unlike the case of B-mode US image registration, not only image voxel intensities are considered but also tissue velocities. Therefore, the cost function proposed takes into account two different terms, one for each information source considered:

$$M(\mathbf{p}) = (1-\lambda)U(\mathbf{p}) + \lambda D(\mathbf{p}), \tag{2.4}$$

where $U(\mathbf{p})$ represents the matching between the registered B-mode frames, $D(\mathbf{p})$ measures the agreement between the estimated velocity field and the velocity values provided by TD images, and λ is a term balancing the contribution of $U(\mathbf{p})$ and $D(\mathbf{p})$. Note that $U(\mathbf{p})$ and $D(\mathbf{p})$ contribute independently to estimate a single and continuous transformation. Therefore, B-mode and TD frames do not need to coincide at specific discrete locations, so data interpolation is not required to compensate for different resolutions.

Scan converted images

For the term $U(\mathbf{p})$ in Equation 2.4, a squared difference of pixel intensities between the reference frame and the rest of frames can be used, as proposed in [27]:

$$U(\mathbf{p}) = \sum_{n=0}^{N} \sum_{\mathbf{x}\varepsilon\Omega_{I_0}} \left(I_n\Big(\varphi_{t_0}(\mathbf{x}, t_n, \mathbf{p})\Big) - I_0(\mathbf{x}) \right)^2, \tag{2.5}$$

where $N+1$ is the number of B-mode frames in the sequence, $I_n(\mathbf{x})$ is the pixel intensity value from B-mode frame n at coordinates $\mathbf{x}$, and Ω_{I_0} is the spatial domain of I_0. This dissimilarity term can be used under the assumption that tissue intensities are globally preserved during the cardiac cycle.

In contrast with Equation 2.5, a dissimilarity measure comparing consecutive frames can also be used to track anatomical structures. In particular, under the assumption that speckle patterns can be represented as a multiplicative Rayleigh distributed noise, and that they are preserved between consecutive frames, a dissimilarity term based on [37] can also be used, similar to [12]:

$$U(\mathbf{p}) = \sum_{n=1}^{N} \sum_{\mathbf{x}\in\Omega_{I_{n-1}}} \ln\left(e^{2\Delta_{n-1}^{n}(\mathbf{x};\mathbf{p})} + 1\right) - \Delta_{n-1}^{n}(\mathbf{x};\mathbf{p}), \tag{2.6}$$

where $\Delta_{n-1}^{n}(\mathbf{x};\mathbf{p}) = I_{n-1}(\mathbf{x}) - I_n\left(\varphi_{t_{n-1}}(\mathbf{x},t_n;\mathbf{p})\right)$.

For the second term in Equation 2.4, $D(\mathbf{p})$, a dissimilarity term measuring the disagreement between the velocities provided by the TD images and the velocity field estimated projected on the beam direction was proposed:

$$\begin{aligned} D(\mathbf{p}) \quad &= \sum_{m=0}^{M} \sum_{\mathbf{x}\in\Omega_{V_0}} \Big(\mathbf{b}\left(\varphi_{t_0}(\mathbf{x},t_m;\mathbf{p})\right) \cdot \mathbf{v}\left(\varphi_{t_0}(\mathbf{x},t_m;\mathbf{p}),t_m;\mathbf{p}\right) \\ &\qquad -V_m\left(\varphi_{t_0}(\mathbf{x},t_m;\mathbf{p})\right)\Big)^2, \end{aligned} \tag{2.7}$$

where $\mathbf{b}(\varphi_{t_0}(\mathbf{x},t_m;\mathbf{p}))$ is a unitary vector in the beam direction, $V_m(\mathbf{x})$ is the velocity value provided at location $\mathbf{x}$ by frame m from the TD image sequence, $M+1$ is the number of TD frames, and Ω_{V_0} corresponds to the spatial domain of the first TD frame.

Non-scan converted images

The terms in Equation 2.5, 2.6 and 2.7 were designed to work with data in Cartesian coordinates. However, some changes are necessary to use them with polar coordnates. When using a traditional B-spline based registration approach with Cartesian images (as shown in Figure2.2(a)), all samples in the image contribute equally to find the optimal velocity value at each control point. In this case, the magnitude of the displacement error at one pixel is independent from its location. When working with images in polar coordinates as shown in Figure2.2(b), the Cartesian space represented by each sample is not homogeneous and increases with its distance to the transducer, as seen in Figure2.2(c). An error of one pixel far from the transducer is larger in Cartesian units (in the physical space) than an error of one pixel close to it. Thus, it is necessary to compensate for this difference.

The relation between a displacement error of a sample at two different locations is proportional to the relation between the Cartesian space between samples at these locations in the direction perpendicular to the beam. Since this space is a function of the distance between the samples and the transducer, an approach weighting each sample contribution depending on its distance to the transducer is proposed. With this approach, the dissimilarity terms proposed previously can be re-written as:

$$U(\mathbf{p}) = \sum_{n=0}^{N} \sum_{\mathbf{x}\varepsilon\Omega_{I_0}} w_U(\mathbf{x}) \left(I_n\left(\varphi_{t_0}(\mathbf{x},t_n,\mathbf{p})\right) - I_0(\mathbf{x}) \right)^2 \tag{2.8}$$

for the dissimilarity term comparing each frame with a reference frame, and:

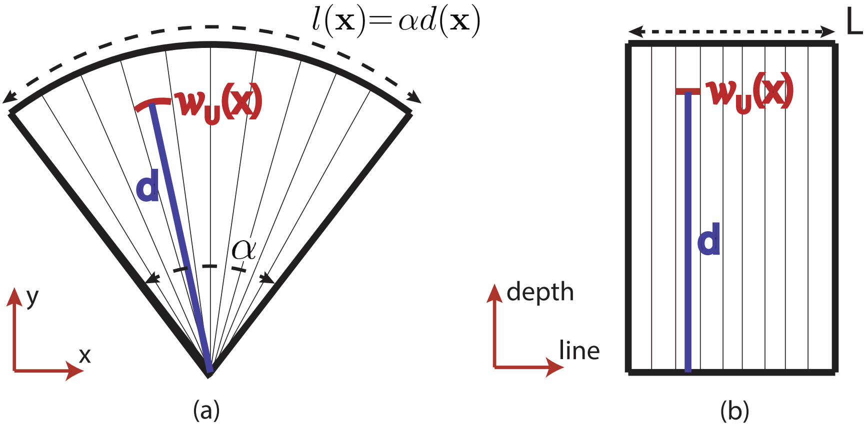

Figure 2.3: Representation of $w_U(\mathbf{x})$ in (a) scan converted and (b) non-scan converted format.

$$U(\mathbf{p})=\sum_{n=1}^{N}\sum_{\mathbf{x}\in\Omega_{I_{n-1}}} w_U(\mathbf{x})\left(\ln(\mathrm{e}^{2\Delta_{n-1}^{n}(\mathbf{x};\mathbf{p})}+1)\right.$$
$$\left.-\Delta_{n-1}^{n}(\mathbf{x};\mathbf{p})\right) \tag{2.9}$$

for the dissimilarity term comparing consecutive frames in the B-mode sequence. In these equations, $w_U(\mathbf{x})$ represents the weight applied to each sample in the B-mode images. The proposed weighting function was:

$$w_U(\mathbf{x})=\frac{l(\mathbf{x})}{L}=\frac{\alpha d(\mathbf{x})}{L}, \tag{2.10}$$

where $l(\mathbf{x})$ is the length of the arch perpendicular to the beam at position $\mathbf{x}$, L is the number of US beams, α is the angle of the whole field of view in radians and $d(\mathbf{x})$ is the distance between $\mathbf{x}$ and the origin of the field of view, as represented in Figure 2.3. In the implementation, $w_U(\mathbf{x})$ was normalized so that $\sum w_U(\mathbf{x})=1$.

For the term comparing the estimated velocities and the velocities from the TD sequence, the same weighting approach was used:

$$D(\mathbf{p})=\sum_{m=0}^{M}\sum_{\mathbf{x}\in\Omega_{V_0}} w_D(\mathbf{x})\Big(\mathbf{b}\left(\varphi_{t_0}(\mathbf{x},t_m;\mathbf{p})\right)\cdot\mathbf{v}\left(\varphi_{t_0}(\mathbf{x},t_m;\mathbf{p}),t_m;\mathbf{p}\right)$$
$$-V_m\left(\varphi_{t_0}(\mathbf{x},t_m;\mathbf{p})\right)\Big)^2, \tag{2.11}$$

where $w_D(\mathbf{x})$ is the weight function applied to each sample in the TD data similar to $w_U(\mathbf{x})$ in Equation 2.10.

Finally, to find the minimum of the proposed dissimilarity metric, the L-BFGS-B (Limited memory Broyden-Fletcher-Goldfarb-Shannon with simple Bounds) [38] optimizer was chosen, which is a limited memory quasi-Newton algorithm for solving large nonlinear optimization problems with simple bounds on the variables.

2.3 Experiments

For the validation of the proposed method, a realistic synthetic dataset including simulations of healthy and pathologic hearts was used. The performance of the method using scan converted and non-scan converted images was compared. In addition, a comparisong between using a speckle-statistics-based approach (Equations 2.6 and 2.9), and comparing each frame in the sequence with a reference frame (Equations 2.5 and 2.8) was performed. Finally, the method was applied to 6 real cases to show that it is able to estimate a realistic motion field in situations where the use of one single modality is challenging.

For all the experiments, a grid of 6 B-spline control points in each spatial dimension was used. In [27], it was demonstrated that increasing the number of temporal control points resulted in higher accuracy, and that taking more temporal control points than the number of frames would oversample the velocity field. For the following experiments, we set the number of temporal control points equal to the number of B-mode frames. In our dataset, the patient with the least number of B-mode frames at rest had 25 frames. Therefore, we constrained the maximum number of temporal control points to 25 for a fair analysis between patients.

2.3.1 Generation of synthetic data

Synthetic B-mode and TD data were generated using a modification of the pipeline described in [39] and summarized in Figure 2.4. A realistic 3D volumetric tetrahedral mesh (as shown in Figure 2.5(a)) was built from the segmentation of a Magnetic Resonance (MR) image acquired from a healthy volunteer. From this volumetric mesh, one cardiac cycle was simulated at a frame rate of 90 Hz, starting from end diastole, using the SOFA (Simulation Open Framework Architecture) [40] simulation framework. This applies the Bestel-Clement-Sorine electromechanical model [41] to the 3D heart geometry to simulate cardiac motion.

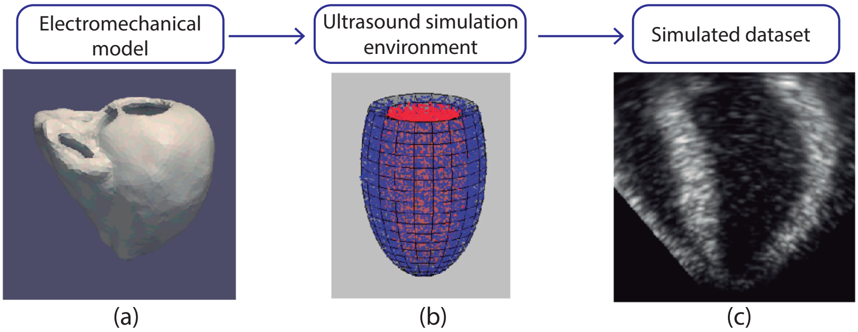

Figure 2.4: Schematic of the pipeline for the simulation of cardiac US sequences in [39].

By modifying the value of the mechanical parameters of the model at a segmental level, several degrees of ischemia can be simulated. In particular, the same 9 cases considered in [39] were included in the present study: one normal case; two cases with ischemia (one mild and one severe) in the proximal region of the left anterior descending artery (LADprox); two cases with ischemia (one mild and one severe) in the distal region of the left anterior descending artery (LADdist); two cases with ischemia (one mild and one severe) in the region of the right coronary artery (RCA); two cases with ischemia (one mild and one severe) in the region of the left circumflex coronary artery (LCX).

The output meshes from the electromechanical simulation were used to displace a cloud of point scatterers mimicking the acoustic tissue response of the myocardium. From each scatter map, US radiofrequency lines were generated by convolving the cloud of scatter points with the point spread function (PSF) of the imaging system. Note that scatterers do not move during the simulation of a single frame, so the acquisition is supposed to be instantaneous. As in [39], COLE [42] was adopted as a fast US simulation environment due to its high computational efficiency. From each time variant scatter map, a B-mode and a TD sequences were generated. In particular, 2D apical four chamber views were considered in this study. For both modalities, the simulated system implemented a 1D phased array with 64 elements, each element of width $\lambda/2$, height 14 mm and a kerf of $\lambda/10$. The simulated probe had a center frequency (f_0) of 4 MHz, a -6 dB relative bandwidth of 65% and a sampling frequency of 50 MHz. The scan angle was 75 degrees, scan depth was 14 cm and the focus was positioned at 7 cm. Note that all the settings of the synthetic system were chosen to be the closest to the real setup used in the in-vivo evaluation (see Table 2.2 and Table 2.3).

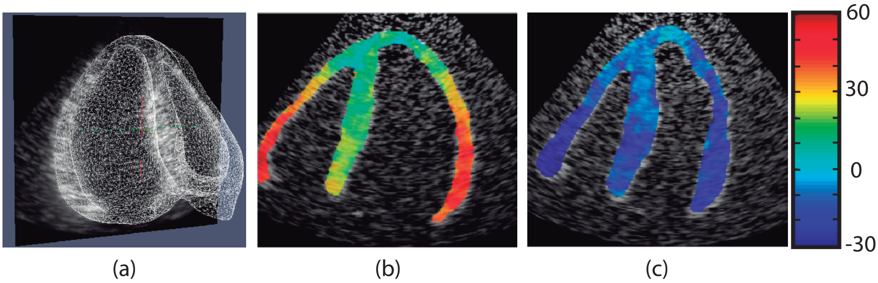

Figure 2.5: (a) A simulated US frame together with the wireframe of the mesh from the electromechanical model are represented. Example of TD images are shown in (b) early systole and (c) early diastole. Colors represent the velocity in mm/s, which is considered positive when directed towards the transducer. Color image in the Appendix, page xvii.

Simulation of B-mode images

One mesh out of three from the electromechanical simulation was considered, leading to an imaging frame rate of 30 Hz. From the associated scatter map, 100 radiofrequency lines were acquired by uniformly sweeping through the scan angle. As such, after envelope detection, log-compression and scan conversion, a set of B-mode images were obtained (pixel size = 0.34x0.34 mm^2). Figure 2.4(b) and Figure 2.4(c) show an example of point scatterers and simulated B-mode image, respectively.

Simulation of TD

All meshes from the electromechanical simulation were considered, leading to a frame rate of 90 Hz. For each frame, 20 scan lines were simulated by uniformly sweeping through the scan angle. For each scan line, a set of four radiofrequency lines were simulated with a pulse repetition frequency (PRF) of 2 KHz. This led to a Nyquist velocity of $\sim$19 cm/s:

$$v_{Nyq} = \frac{c \cdot PRF}{4 f_0}, \tag{2.12}$$

where c is the sound speed in the tissue ($\sim$1540 m/s) and f_0 is the center frequency. Tissue motion between two successive firings in the same direction was simulated by linearly interpolating the position of the scattering centers in the considered frame and the following one. For each scan line and each depth, the tissue velocity was computed from the corresponding package of four signals by means of a standard phase shift based estimator [43]. After color rendering of the computed velocity and scan conversion, TD images, as the ones of Figure 2.5 (b)(c), were obtained.

Table 2.1: Summary of the methods compared using the synthetic dataset.

Method	**Image format**	**B-mode dissimilarity**
M1	Non-scan converted (Figure 2.2(b))	US-specific (Eq. 2.9)
M2	Scan converted (Figure 2.2(a))	US-specific (Eq. 2.6)
M3	Non-scan converted (Figure 2.2(b))	Mean squared error (Eq. 2.8)
M4	Scan converted (Figure 2.2(a))	Mean squared error (Eq. 2.5)

2.3.2 Selection of the weighting parameter λ

The weighting parameter λ balances the contribution of each term in the dissimilarity measure (see Equation 2.4). A high value of λ gives more importance to $D(\mathbf{p})$, while a low value gives more importance to $U(\mathbf{p})$.

To choose an adequate value of λ, two main aspects have been considered: (i) the confidence on the value provided by each term, and (ii) the way each term converges to its minimum. The former was considered to be equivalent to the confidence on the data provided by each modality. The latter was related to the slope of the function that is minimized during the optimization. Thus, an adequate value of λ would balance the magnitude of the slope of both terms. Considering these two aspects, we set λ as:

$$\lambda = \gamma\zeta, \tag{2.13}$$

where γ is the ratio between the confidence on the TD data and the B-mode images, and ζ is the ratio between the slope of the two terms in the dissimilarity measure. In our experiments, the confidence ratio was set to 1, thus assuming the same quality for TD and B-mode images. ζ was approximated as the magnitude of the initial derivative (with respect to the transformation parameters) of $U(\mathbf{p})$ divided by the derivative of $D(\mathbf{p})$.

2.3.3 Validation with synthetic data

The proposed method was applied to the previously described synthetic dataset to evaluate its accuracy in terms of displacement. The possible combinations between the dissimilarity measure in Equation 2.5 and the one in Equation 2.6, and between using Cartesian and polar data were tested, as summarized in Table 2.1. Figure 2.6 shows the mean error and the standard deviation of the displacements calculated from the first frame for all the synthetic patients during one cardiac cycle implementing these different alternatives.

Results from Figure 2.6 show that using both non-scan converted images

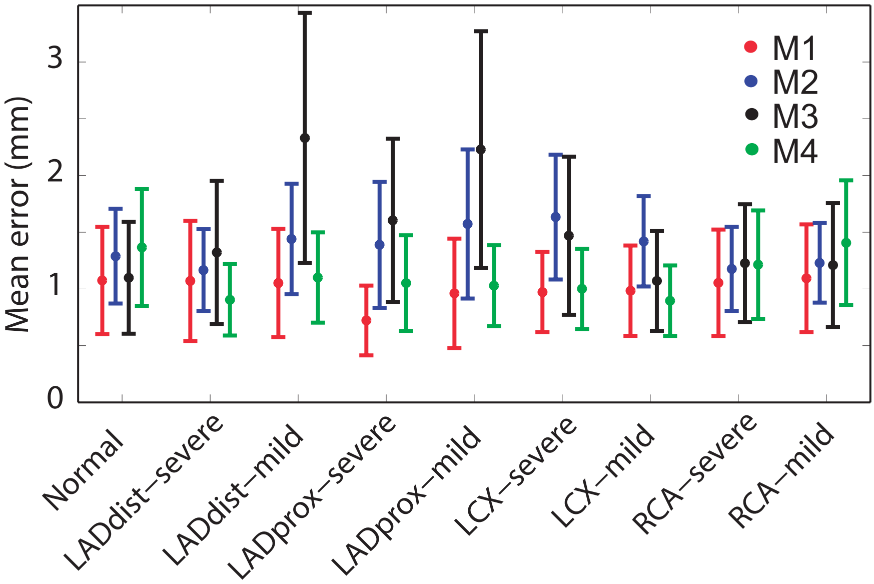

Figure 2.6: Mean errors (circles) and standard deviations (lines) calculated for the 9 synthetic datasets during one cardiac cycle with the methods summarized in Table 2.1. Color image in the Appendix, page xvii.

and a dissimilarity measure including speckle distribution statistics gives better performance in average than the other three alternatives evaluated, reducing the mean error of the displacements estimated with methods M2, M3 and M4 by 35%, 48% and 10%, respectively. Mean differences between the method M1 and the methods M2 and M3 were found to be statistically significant with $p < 0.05$ using a Student's t-test, assuming a normal distribution of the errors. Normality assumptions were checked using a Lilliefors test. Mean differences between methods M1 and M4 were not found to be statistically significant, obtaining a p-value of 0.15.

Figure 2.7 compares displacement error results obtained with M1 with respect to the results obtained taking into account only the B-mode images, using Equation 2.9. The results show that integrating B-mode images and TD velocities results in a more accurate estimation of the displacement field. Differences between the mean displacement error obtained by integrating B-mode and TD data, and the error obtained using only B-mode were found to be statistically significant with $p < 0.05$.

2.3.4 Experiments with clinical data

The method was also applied to a set of US images acquired from 6 volunteers (age 30 ± 5.5, males) with a Vivid-Q system (GE Healthcare Mil-

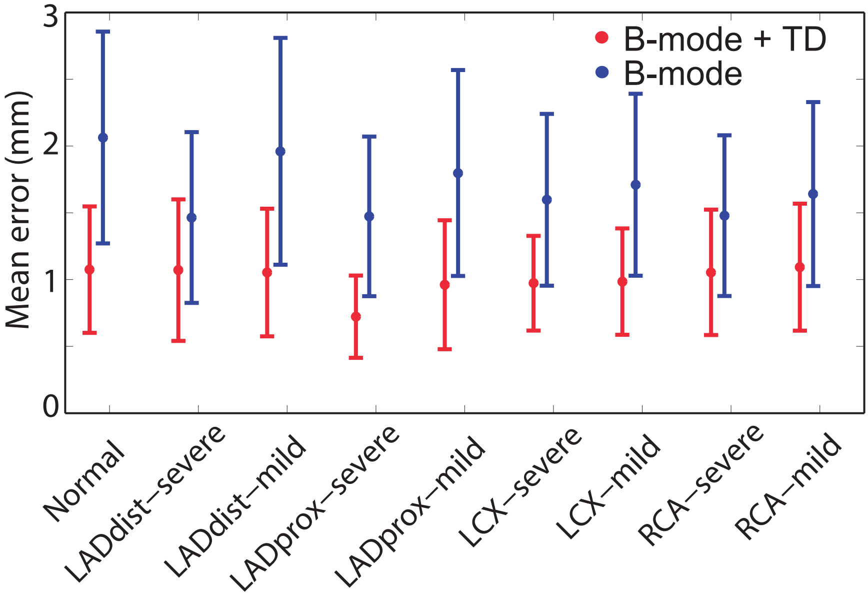

Figure 2.7: Mean errors (circles) and standard deviations (lines) calculated for the 9 synthetic patients during one cardiac cycle with method M1 (red) and using only B-mode images (blue). Color image in the Appendix, page xviii.

waukee, WI) and a GE Healthcare M4S probe (1.7/3.4 MHz frequency). For each case, both B-mode and TD images of the left ventricle were acquired at rest. Afterwards, stress echocardiography was performed with an ergometric bicycle and images were acquired at maximum effort. Table 2.2 and Table 2.3 show the mean values and standard deviation for the different parameters of the acquired B-mode and TD images, respectively. Our method integrating both B-mode and TD information for motion estimation was applied to the acquired images and results were compared to the ones obtained by using only B-mode images.

Figure 2.8 shows the result of tracking a set of landmarks placed on the left ventricle along one cardiac cycle using only B-mode images (yellow), and integrating both B-mode and TD (red) with the proposed method, for one patient at rest. As it can be observed, most of the differences between both methods lay on the lateral wall. Figure 2.10 shows the displacements calculated using the two methods in both beam and azimuth directions. Spatiotemporal color maps were used to visualize the results. An illustration to understand this kind of map is shown in Figure 2.9. The vertical axis represents spatial locations along the myocardium (which has been unfolded inspired from anatomical M-mode echocardiographic images) and the horizontal axis represents time in the cardiac cycle. Positive beam displacement

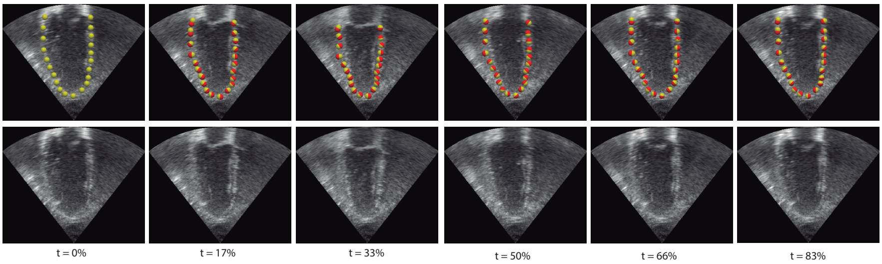

Figure 2.8: The top row shows a set of landmarks placed on the left ventricle and displaced according to the transformation calculated using only B-mode (yellow), and using both B-mode and TD together (red) at different times of the cardiac cycle for one example patient at rest. The bottom row shows the corresponding B-mode images. Color image with larger size in the Appendix, page xx.

Table 2.2: Comparison between B-mode image information for real cases at rest, during exercise and for synthetic data.

	Rest	**Exercise**	**Synthetic**
Frames/cycle	39 ± 9	14 ± 2	27
Frame rate (Hz)	35 ± 9	34 ± 7	30
Beams	92.3 ± 9.4	85.7 ± 18.9	100
Samples/beam	577 ± 47.9	584.2 ± 64.9	248
Opening angle (°)	70 ± 7	65 ± 14.1	75
Depth (mm)	133 ± 11	135 ± 15	140

Table 2.3: Comparison between TD image information for real cases at rest, during exercise and for synthetic data.

	Rest	**Exercise**	**Synthetic**
Frames/cycle	105 ± 28	45 ± 7	79
Frame rate (Hz)	116 ± 28	107 ± 22	90
Beams	14 ± 3.1	15.3 ± 2.7	20
Samples/beam	190.5 ± 180.4	194.7 ± 21.4	248
Opening angle (°)	69 ± 8.4	60.5 ± 12.4	72
Depth (mm)	133 ± 11	135 ± 15	140
Nyquist vel. (cm/s)	18.1 ± 3	31.6 ± 1.5	19
PRF (Hz)	1125 ± 191	1958.3 ± 93.2	2000

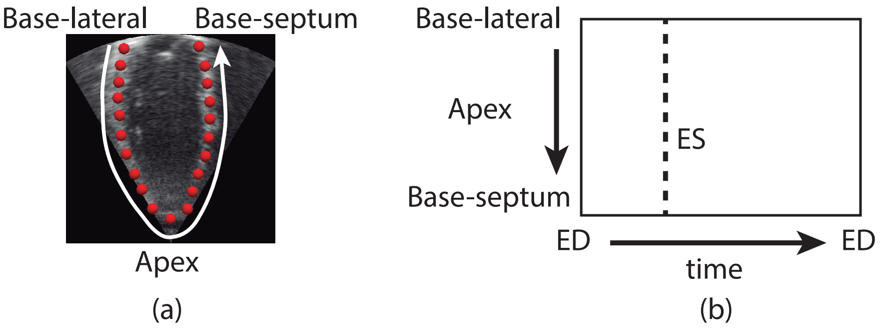

Figure 2.9: Schematic describing a spatiotemporal map. (a) shows a curved line placed along the myocardium in a B-mode image and (b) shows the corresponding spatiotemporal map. The vertical axis represents spatial locations along the myocardium and the horizontal axis represents time in the cardiac cycle extracted between consecutive R-peaks in the ECG. The dotted vertical line indicates end systole. ED and ES stand for end diastole and end systole, respectively.

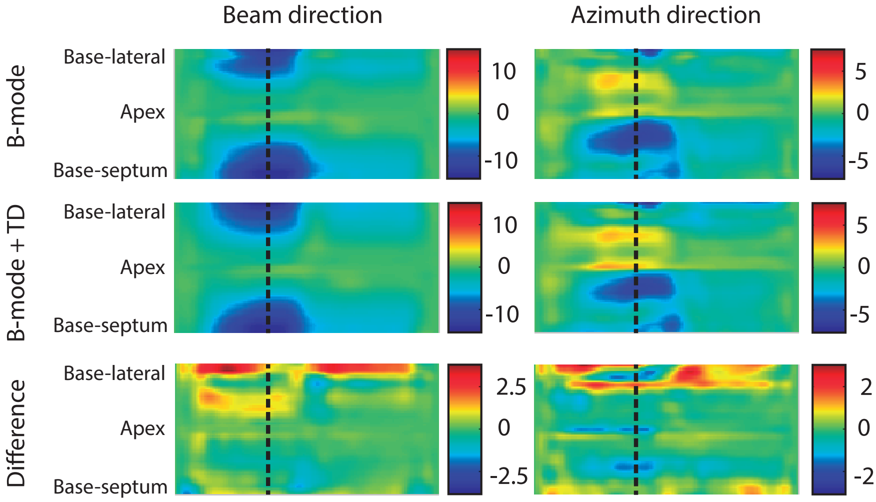

Figure 2.10: Displacements (in mm) estimated using only B-mode images (top row), using B-mode and TD together (middle row) and the difference between both approaches (bottom row) for one patient at rest. Color image in the Appendix, page xviii.

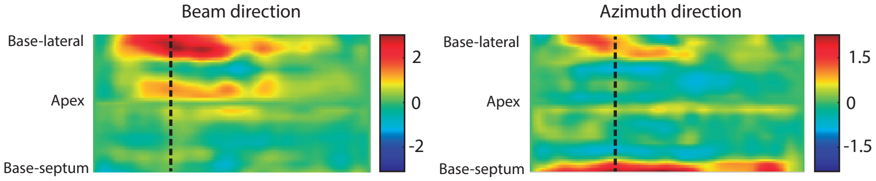

Figure 2.11: Mean difference between displacements (in mm) estimated using only B-mode and using both B-mode and TD at rest. Color image in the Appendix, page xix.

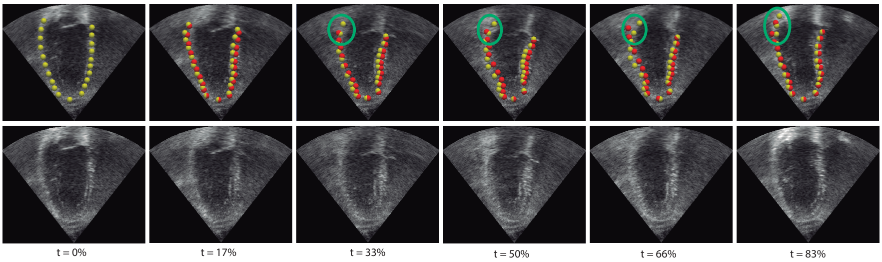

Figure 2.12: The top row shows a set of landmarks placed on the left ventricle and displaced according to the transformation calculated using only B-mode (yellow), and using both B-mode and TD together (red) at different times of the cardiac cycle during exercise for the patient in Figure 2.8. Green circles indicate where tracking using B-mode only has problems due to image quality. The bottom row shows the corresponding B-mode images. Color image with larger size in the Appendix, page xxi

was defined from apex to base, while positive displacement on the azimuth direction was defined from lateral wall to septum. One can see that the difference between the displacements estimated with the two methods is larger at the base of the lateral wall.

Figure 2.11 shows the mean displacement differences between the two methods for the 6 patients analyzed at rest. Results show that the displacement estimated at end systole using only B-mode images is lower, in average, than the displacement estimated with the proposed method, and with maximum difference located at the base of the ventricle. These results are in line with the results obtained for the patient shown in Figure 2.10.

Figure 2.12 shows the result of tracking a set of landmarks placed on the left ventricle with the two methods for the patient presented in Figure 2.8, using the data acquired during exercise. Figure 2.13 also shows the displacements calculated during exercise for this patient. As it can be observed, displacement differences between the two approaches are increased with respect to the results obtained at rest. Moreover, the displacement pattern estimated using only B-mode images in Figure 2.13 does not look physio-

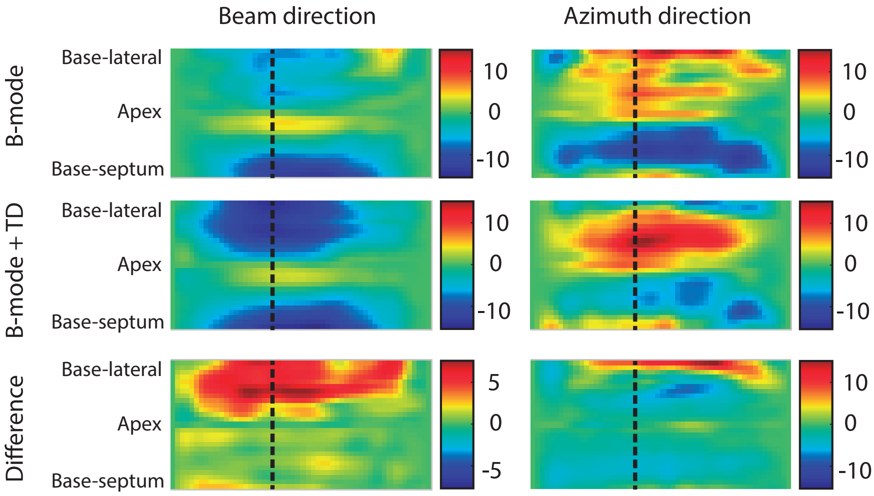

Figure 2.13: Displacements (in mm) estimated using only B-mode images (top row), using B-mode and TD together (middle row) and the difference between both approaches (bottom row) for one patient during exercise. Color image in the Appendix, page xix.

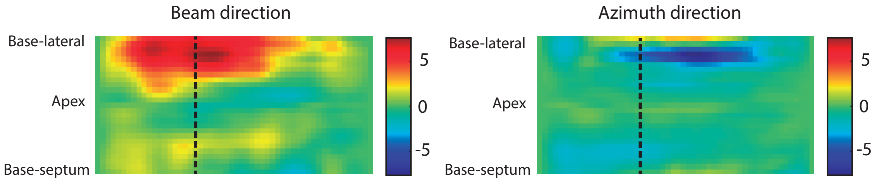

Figure 2.14: Mean difference between displacements (in mm) estimated using only B-mode and using both B-mode and TD during exercise. Color image in the Appendix, page xix.

logically realistic.

The mean displacement differences between the two approaches were finally calculated using the data acquired during exercise for the 6 patients analyzed, as shown in Figure 2.14. It is possible to see that the magnitude of the mean difference is increased when compared to the differences from the data acquired at rest. In addition, most of these differences are located at the base of the lateral wall.

2.4 Discussion

The proposed method was validated using a synthetic dataset and the alternatives shown in Table 2.1 were compared. Results in Figure 2.6 show that the method M1 performs better, in average, than the other tested alternatives. Furthermore, M1 uses non-scan converted images, so the registration process is computationally less expensive because the number of samples in the images before scan conversion is lower. In addition, it is not necessary to mask the field of view, since all samples in the images provide valuable information.

From the results in Figure 2.6, one can conclude that, among the generated synthetic cases, M4 performs better in those cases where ischemia is simulated close to the Left Anterior Descending (LAD) artery and the Left Circumflex (LCX). The 2D simulated images include the areas in the septum and lateral wall that are more affected by the ischemia in the LAD and LCX regions, respectively. Since local motion in ischemic regions is reduced, local changes between consecutive frames are also reduced. Method M4 uses a dissimilarity measure that compares all frames with a reference frame, so its performance varies depending on how similar each frame is to the reference. Therefore, in those cases where motion is reduced, the performance of M4 may improve, producing slightly better results than M1 in ”LADdist-severe” and ”LCX-mild” cases. Method M2 likely fails because it applies a speckle statistics-based measure to Cartesian B-mode images. This kind of metric uses the Rayleigh distribution to model the speckles. However, when working with Cartesian images, many pixels in the image contain interpolated information, resulting in a speckle patterns whose properties may differ from the Rayleigh statistics. Finally, M3 performs worse than the others. The dissimilarity measure used by this method compares each frame, in non-scan converted format, to a reference frame using a mean squared error-based approach. In this case, if the tissue structures imaged in the reference frame fall completely or partially out of the US lines, since there is no interpolation, this information will be completely lost. Thus, M3 could fall into a local minimum during the optimization process, not being able to recover an accurate displacement field.

The proposed method was also applied to 6 healthy volunteers, acquiring images both at rest and during exercise. Since the quantitative parameters extracted from echocardiographic sequences [1] are highly conditioned by the accuracy of the tracking, clinical studies targeting a better understanding of cardiac function during exercise may benefit from the improvements of the proposed method. These protocols are currently receiving more attention to understand the cardiac function contribution to the functional capacity during effort and to prevent from any potentially high-risk impairment [35, 36].

Results from Figure 2.11 show the differences between displacements estimated using only B-mode and integrating both B-mode and TD at rest. As it can be seen, the magnitude of the difference in the displacements on the beam direction is low in average, being higher in the lateral wall with a maximum of 2.5 mm at end systole. Displacement differences on the azimuth direction are lower than in the case of displacements on the beam direction as expected, since TD only gives information on the beam direction. Most of the differences in the azimuth direction are accumulated at the base and differences may occur as a consequence of different estimations on the beam direction. Figure 2.8 and Figure 2.10 show the displacements estimated for one example case using only B-mode and using both B-mode and TD. These results are in line with the average results previously discussed.

Displacements were also estimated for these 6 volunteers during exercise. In this situation, the quality of the B-mode images acquired is worse due to the difficulty of the acquisition, as it can be observed in Figure 2.12. This, added to the reduced number of frames because of higher heart rates, makes displacement estimation using only B-mode images challenging. In the present study, the number of frames during exercise was reduced to 41% of the number of frames acquired at rest. Results from Figure 2.14 show larger differences between the displacements estimated using only B-mode and using both B-mode and TD together when compared with the results obtained at rest. These larger differences are more visible at the base of the lateral wall, with a maximum error of about 6 mm at end systole. The basal level (mitral annulus) and the lateral wall are subject to lower image quality (border of the echocardiographic window, reflections, and position of the valve with respect to the myocardium). Green circles in Figure 2.12 indicate a region where tracking using B-mode only is prone to large errors. Our method might also lead to inaccuracies in such challenging cases (radial motion tends to be overestimated at the apical lateral level). However, due to the use of TD data, these artifacts are more localized and along the azimuth direction only. The example case displayed in Figure 2.13 also shows large differences in the estimation of displacements in the lateral wall, in line with the average results.

A limitation of this study is the number of real cases included, which is not enough to obtain conclusions about the clinical improvements of the proposed method. However, the primary objective was to show the feasibility and the added value of this approach as compared to the ones considering a single modality.

2.5 Conclusions

A method to integrate B-mode images and TD velocities in a single registration framework has been proposed. Unlike other methods to integrate these two modalities [14, 13, 32], B-mode and TD samples are evaluated independently and they do not have to coincide in time, so temporal/spatial interpolation is not needed to calculate a single and continuous transformation.

The improvements of using both modalities together instead of a single modality were demonstrated. Results from validation with synthetic data showed that using speckle statistics information and data before scan conversion outperforms the results obtained by using a classical pixel intensity-based dissimilarity measure, such as a mean-squared-error approach. Experiments with real cases also showed that integrating both modalities gives a realistic motion estimation in cases where using only B-mode images is challenging.

CHAPTER **3**

Integration of multi-plane tissue Doppler and B-mode echocardiographic images for left ventricular motion estimation

Although modern ultrasound acquisition systems allow recording of 3D echocardiographic images, tracking anatomical structures from them is still challenging. In addition, since these images are typically created from information obtained across several cardiac cycles, it is not yet possible to acquire high-quality 3D images from patients presenting varying heart rhythms. In this chapter, the method proposed in Chapter 2 is extended to estimate the motion field from multi-plane echocardiographic images of the left ventricle, which are acquired simultaneously during a single cardiac cycle. The method integrates tri-plane B-mode and tissue Doppler images acquired at different rotation angles around the long axis of the left ventricle. It uses a diffeomorphic continuous spatiotemporal transformation model with a spherical data representation for a better interpolation in the circumferential direction. This framework allows exploiting the spatial relation among the acquired planes. In addition, higher temporal resolution of the transformation in the beam direction is achieved by uncoupling the estimation of the different components of the velocity field. The method was validated using a realistic synthetic dataset including healthy and ischemic cases, obtaining errors of 0.14 ± 0.09 mm for displacements, 0.96 ± 1.03 % for longitudinal strain and 3.94 ± 4.38 % for radial strain estimation. The method was also demonstrated on a healthy volunteer and two patients with ischemia.

The content of this chapter is adapted from the following publication:

A. R. Porras, M. Alessandrini, O. Mirea, J. D'hooge, A. F. Frangi, and G. Piella. Integration of multi-plane tissue Doppler and B-mode echocardiographic images for left ventricular motion estimation. *Submitted to IEEE Transactions on Medical Imaging*.

3.1 Introduction

Ultrasound (US) imaging is the standard modality used to assess cardiac motion and deformation. Tissue Doppler (TD) images are normally used in clinical practice to measure the velocity of moving anatomical structures. The recorded information corresponds to the velocity component on the direction of the US beam, so only a velocity field with one-dimensional information can be reconstructed [5]. Complementarily, B-mode echocardiographic images are used to estimate cardiac motion and strain from 2D images. However, it is necessary to acquire 6 different views to obtain longitudinal, circumferential and radial components in all the left ventricle segments [23]. Some works have also explored the possibility of using 2D B-mode and TD images acquired interleaved for an improved tracking [44, 14, 32].

During the last few years, technology improvements have allowed the acquisition of 3D US images by integrating small volumetric information acquired during consecutive cardiac cycles. However, the wider field of view is achieved at a cost of spatial and temporal resolution, so motion estimation from 3D US images is challenging. Moreover, since information from different regions is acquired during different cardiac cycles, 3D US is not suitable for patients with varying heart rhythms.

Modern US imaging systems allow for the acquisition of a set of 2D image sequences with different orientations simultaneously [45]. This type of images have been used to assess cardiac mechanics in different areas of the left ventricle at the same time. In [46], tri-plane acquisitions were demonstrated to be feasible and sensitive to detect coronary artery disease. In [47], cardiac motion was assessed from tri-plane images and results were compared with the ones obtained from conventional 2D B-mode US images. Accuracy was very similar between both methods. However, since tri-plane US images are acquired simultaneously, the acquisition time is shorter. Tri-plane TD images were also used in [48] to predict acute response to cardiac resynchronization therapy. However, motion was computed independently at each plane and spatial coherence was not considered. Moreover, the method used only either the B-mode or the TD image sequence. In Chapter 2, it has been shown that integrating both types of information outperforms the use of each one separately. In the current chapter, this method is extended to estimate motion in the whole left ventricle, ensuring spatial coherence of the motion field between the planes where information is available by using a spherical coordinate system. Furthermore, increased temporal resolution in the beam direction is achieved by using different temporal resolutions in the estimation of the different components of the velocity field, while keeping the temporal continuity and consistency between them. The

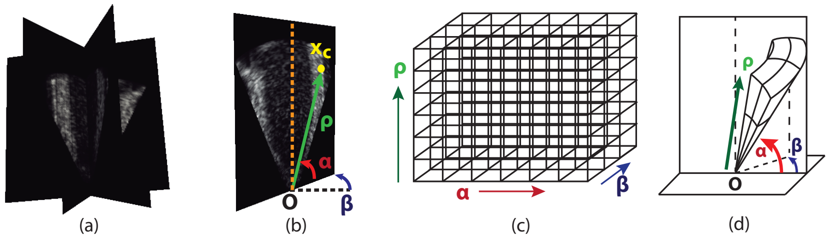

Figure 3.1: (a) Apical view example of tri-plane US images. (b) Representation of a 2D point from one view in 3D spherical coordinates. (c) Representation of a 3D grid of control points in spherical coordinates. (d) Section of the grid from (c) in the Euclidean space.

method is validated using a realistic synthetic dataset, and its utility to detect ischemia in real cases is illustrated. Moreover, strain accuracy is evaluated.

3.2 Methodology

In this section, a description of the proposed registration framework is presented.

3.2.1 Coordinate system

Tri-plane data consist in three sequences of US images acquired interleaved at different rotation angles around the long axis of the left ventricle (Figure 3.1(a)). Every point from one of the 2D planes can be mapped to a reference 3D space using a rigid transformation:

$$\mathbf{x_E} = \mathbf{x_c}\mathbf{R_c}, \tag{3.1}$$

where $\mathbf{x_c}$ represents the spatial coordinates of a 2D point in the view c, $\mathbf{R_c}$ is the known rotation matrix about the long axis and $\mathbf{x_E}$ represents the 3D coordinates of the point in the Euclidean reference space.

As in conventional 2D US imaging, it is possible to acquire TD images at different orientations together with the B-mode frames in multi-plane US imaging. In Chapter 2, a method that integrates 2D B-mode and TD images through a similarity measure that considers both sequences for an improved motion estimation was proposed. That method could be used to estimate motion independently at each of the acquired planes. However, only in-plane motion would be estimated and spatial coherence between planes would not be considered. The method from Chapter 2 could also be extended to 3D by using a 3D+t transformation model and evaluating only the information available from the 3 planes acquired. Since motion interpolation between planes depends on the topology of the B-spline grid of

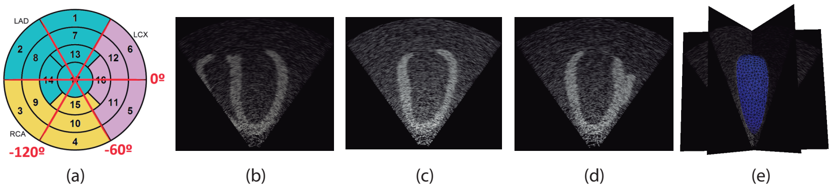

Figure 3.2: (a) Bull's eye plot of the left ventricle for the healthy synthetic case, divided according to American Heart Association's proposal [49]. Red lines indicate the three planes simulated at (b) 0°, (c) 60°, and (d) 120°. (e) is the 3D representation of the tri-plane data and the mesh segmented at end-diastole.

control points, we propose to use a spherical coordinate system to model the transformation. This topology provides an interpolation in the circumferential direction that adapts better to the left ventricle shape than a traditional Euclidean topology. The relation between the Euclidean coordinates of one point $\mathbf{x_E} = (x, y, z)$ and its spherical coordinates $\mathbf{x_s} = (\rho, \alpha, \beta)$ is:

$$\begin{aligned} x &= \rho\, cos(\alpha)\, cos(\beta) \\ y &= \rho\, sin(\alpha) \\ z &= \rho\, cos(\alpha)\, sin(\beta), \end{aligned} \tag{3.2}$$

where $\rho \in [0, L]$ represents the radial distance of the point to the origin of the field of view for a maximum depth L, $\alpha \in [0, \frac{\pi}{2}]$ represents the angle in the azimuth direction on the 2D plane and $\beta \in [-\pi, \pi]$ the rotation angle in the circumferential direction. The origin of both the Euclidean and the spherical coordinate systems corresponds to the origin of the field of view.

3.2.2 The transformation

To estimate a 3D motion field from tri-plane data, we adapted the transformation model from [27] to spherical coordinates. The transformation mapping a point at coordinates $\mathbf{x_s}$ from time t_0 to T can be written as:

$$\varphi_{t_0}(\mathbf{x_s}, T, \mathbf{p}) = \mathbf{x_s} + \int_{t_0}^{T} \mathbf{v}(\varphi_{t_0}(\mathbf{x_s}, t, \mathbf{p}), t, \mathbf{p})dt, \tag{3.3}$$

where $\mathbf{v}(\mathbf{x_s}, t, \mathbf{p})$ is the velocity of the point at spherical coordinates $\mathbf{x_s}$ and time t, and $\mathbf{p}$ is the transformation parameters vector. The velocity field is modeled continuously both in space and time using cubic uniform B-spline kernel functions, similar to [27].

The typically acquired B-mode images usually have higher spatial resolution than the TD images, while the latter normally have higher temporal resolution. Therefore, one advantage of using both modalities together is the increased temporal resolution in the beam direction because of the use of TD information. In [27], it was shown that using as many control points as possible in the temporal dimension to model the transformation improved the accuracy of the results. However, when using more temporal control points than frames available, the performance of the method decreases due to data oversampling. In Chapter 2, when integrating 2D B-mode and TD images for motion estimation, the number of temporal control points was then constrained to the number of B-mode frames available to avoid oversampling in the azimuth direction (since no information from TD is provided in this direction), even though the temporal resolution of the TD images was higher. Using a spherical coordinate system to define the transformation model allows for the separation of the velocity component in the beam direction from the other two spatial directions. This makes possible to model the different components using different grid resolutions. Therefore, the velocity of a point $\mathbf{x_s}$ at a time instant t in the direction d is represented as:

$$\begin{aligned}\mathbf{v}^d(\mathbf{x_s},t,\mathbf{p}^d) &= \sum_{i,j,k,l} B\left(\frac{\rho-q_i^d}{\Delta_i^d}\right)B\left(\frac{\alpha-q_j^d}{\Delta_j^d}\right)\\ &\qquad B\left(\frac{\beta-q_k^d}{\Delta_k^d}\right)B\left(\frac{t-q_l^d}{\Delta_l^d}\right)\mathbf{p}^d_{i,j,k,l},\end{aligned} \tag{3.4}$$

where $\Delta^d = (\Delta_i^d,\Delta_j^d,\Delta_k^d,\Delta_l^d)$ is the spacing between the B-spline control points modeling the velocity component on the direction d, $\mathbf{Q}^d = (q_i^d,q_j^d,q_k^d,q_l^d)$ represents the location of the control points, $B(\cdot)$ is a cubic B-spline kernel function, and $\mathbf{p}^d_{i,j,k,l}$ is the B-spline coefficient at index (i,j,k,l). Since the velocity at $\beta=-\pi$ and $\beta=\pi$ should be the same for fixed ρ and α, the B-spline was designed to be cyclic in the circumferential angle direction β by letting the B-spline polynomials wrap around this direction, similar to the anatomically oriented grid proposed in [50]. Figures 3.1(c) and 3.1(d) illustrate the grid topology represented in spherical and Euclidean coordinates, respectively.

3.2.3 The dissimilarity measure

Since both B-mode and TD images from each 2D view are integrated, a global measure including the contribution of both the B-mode and the TD sequences is proposed based on Equation 2.4 (page 19):

$$M(\mathbf{p}) = \sum_{c=0}^{2} \left((1-\lambda_c)\, U_c(\mathbf{p}) + \lambda_c D_c(\mathbf{p}) \right), \tag{3.5}$$

where $U_c(\mathbf{p})$ is a measure for the dissimilarity between each B-mode frame and the first frame from view c, $D_c(\mathbf{p})$ compares the estimated velocities in the beam direction with the velocity values provided by the TD images from view c, and λ_c is a term balancing the contribution of $U_c(\mathbf{p})$ and $D_c(\mathbf{p})$.

The term $U_c(\mathbf{p})$ was modeled using a mean-squared-error approach:

$$U_c(\mathbf{p}) = \sum_{n=0}^{N_c} \sum_{\mathbf{x_s} \in \Omega_{I_0^c}} \left(I_n^c\Big(\varphi_{t_0}(\mathbf{x_s}, t_n, \mathbf{p})\Big) - I_0^c(\mathbf{x_s}) \right)^2, \tag{3.6}$$

where $N_c + 1$ is the number of B-mode frames from view c, $I_n^c(\mathbf{x_s})$ is the pixel intensity value at B-mode frame n from view c at coordinates $\mathbf{x_s}$, and $\Omega_{I_0^c}$ is the spatial domain of the first frame from view c. This dissimilarity term was chosen under the assumption that tissue intensities are globally preserved during the cardiac cycle. Although this kind of measure has demonstrated to provide good results when working with 3D US data in [27], another type of dissimilarity could have been used. In particular, in Chapter 2, a measure considering consecutive pairs of frames and including speckle statistics information was proposed. We discarded this type of measure in multi-plane images because the temporal resolution of the B-mode images at each view is lower than in typical 2D B-mode US images and, therefore, speckles are not well preserved between consecutive frames.

The second term of the proposed global dissimilarity measure was:

$$\begin{aligned} D_c(\mathbf{p}) \quad &= \sum_{m=0}^{M_c} \sum_{\mathbf{x_s} \in \Omega_{V_0^c}} \Bigg(\mathbf{b}\Big(\varphi_{t_0}(\mathbf{x_s}, t_m, \mathbf{p})\Big) \cdot \\ &\mathbf{v}\Big(\varphi_{t_0}(\mathbf{x_s}, t_m, \mathbf{p}), t_m, \mathbf{p}\Big) - V_m\Big(\varphi_{t_0}(\mathbf{x_s}, t_m, \mathbf{p})\Big)\Bigg)^2, \end{aligned} \tag{3.7}$$

where $M_c + 1$ is the number of TD frames from view c, $\mathbf{b}(\mathbf{x_s})$ is the beam direction at coordinates $\mathbf{x_s}$, $V_m(\mathbf{x_s})$ is the velocity value provided by TD frame at $t = t_m$ and location $\mathbf{x_s}$, and $\Omega_{V_0^c}$ is the spatial domain of the first frame from view c.

The weighting term λ_c used for each view c in Equation 3.5 was modeled in terms of confidence (γ_c) and convergence (ζ_c), as in Equation 2.13 (page 25):

$$\lambda_c = \gamma_c \zeta_c. \tag{3.8}$$

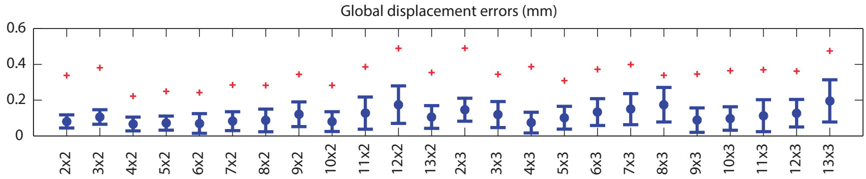

Figure 3.3: Displacement errors using different grid resolutions. Circles represent the displacement error averaged for all points in the left ventricle during the cardiac cycle, lines represent the standard deviation. Crosses represent the mean error at end systole. The horizontal axis represents each of the experiments performed with different grid resolutions, labeled as ρ x α.

As in Chapter 2, γ_c was set to 1, thus assuming the same confidence for TD and B-mode images. The convergence ratio ζ_c was approximated as the magnitude of the initial derivative with respect to the transformation parameters of $U_c(\mathbf{p})$ divided by the derivative of $D_c(\mathbf{p})$.

To find the transformation parameters that minimize the value of the proposed dissimilarity measure, the L-BFGS-B (Limited memory Broyden-Fletcher-Goldfarb-Shannon with simple Bounds) [38] optimizer was chosen, as in Chapter 2.

3.3 Experiments

3.3.1 Synthetic dataset generation

A realistic synthetic dataset was used to validate the proposed method. The pipeline designed for its generation was similar to the one developed in the STRAUS poject [39, 51], but adapted to simulate multi-plane images. A magnetic resonance image acquired from one healthy subject was manually segmented, thus generating a 3D volumetric mesh. This segmentation was then used as an input to the SOFA (Simulation Open Framework Architecture) software package [40], which allows simulating one cardiac cycle by applying the Bestel-Clement-Sorine electro-mechanical model [41]. One healthy and 4 ischemic cases were simulated by modifying the value of the mechanical parameters of the model at segmental level. In particular, the 4 ischemic cases were generated to simulate ischemia in the proximal region of the left anterior descending artery (LADprox), the distal region of the left anterior descending artery (LADdist), the left circumflex coronary artery (LCX) and the right coronary artery (RCA).

A cloud of point scatterers mimicking the acoustic tissue response of the myocardium was displaced using the output meshes of the electro-mechanical simulation. COLE [42] was used as an US simulation framework to gen-

Table 3.1: Specifications of the synthetic B-mode and TD images.

	B-mode	**TD**
Frames/cycle	14	98
Frame rate (Hz)	14	98
Beams	128	28
Samples/beam	547	197
Opening angle (°)	70	70
Depth (mm)	160	160
Nyquist velocity (cm/s)	–	23.3
PRF (Hz)	–	2000

erate the final images. In particular, three 2D US sequences, including B-mode and TD images, were generated as 4-chambers, 3-chambers, and 2-chambers apical views, with an angle of 60° between planes about the long axis, as represented in Figure 3.2. The specifications of the generated B-mode and TD image sequences are detailed in Table 3.1.

3.3.2 Validation with synthetic data

To validate the proposed method, it was first necessary to optimize the number of control points used for each spatiotemporal dimension. To this end, a set of experiments using different number of control points for the beam (ρ) and azimuth (α) directions were performed with the healthy synthetic case. The transformation estimated using the proposed method was applied to the segmented left ventricle to recover its motion during one cardiac cycle, and longitudinal and radial displacement errors were calculated at every vertex in the volumetric mesh. Note that the circumferential component cannot be recovered with apical long axis views, since it is orthogonal to the imaging planes. The mean displacement error magnitude and standard deviation for all points in the left ventricle during the cardiac cycle using different grid resolutions is represented in Figure 3.3, together with the mean displacement error calculated at end systole.

As it can be observed from Figure 3.3, the lowest displacement errors, both at end systole and averaging the whole cardiac cycle, were obtained when using 2 control points in the azimuth direction and 4-6 in the beam direction. These results are similar to the ones obtained in [27] with a Euclidean grid of control points using 3D US images. In our case, we obtained the lowest mean error (0.0668 ± 0.0386 *mm*) and end-systolic error

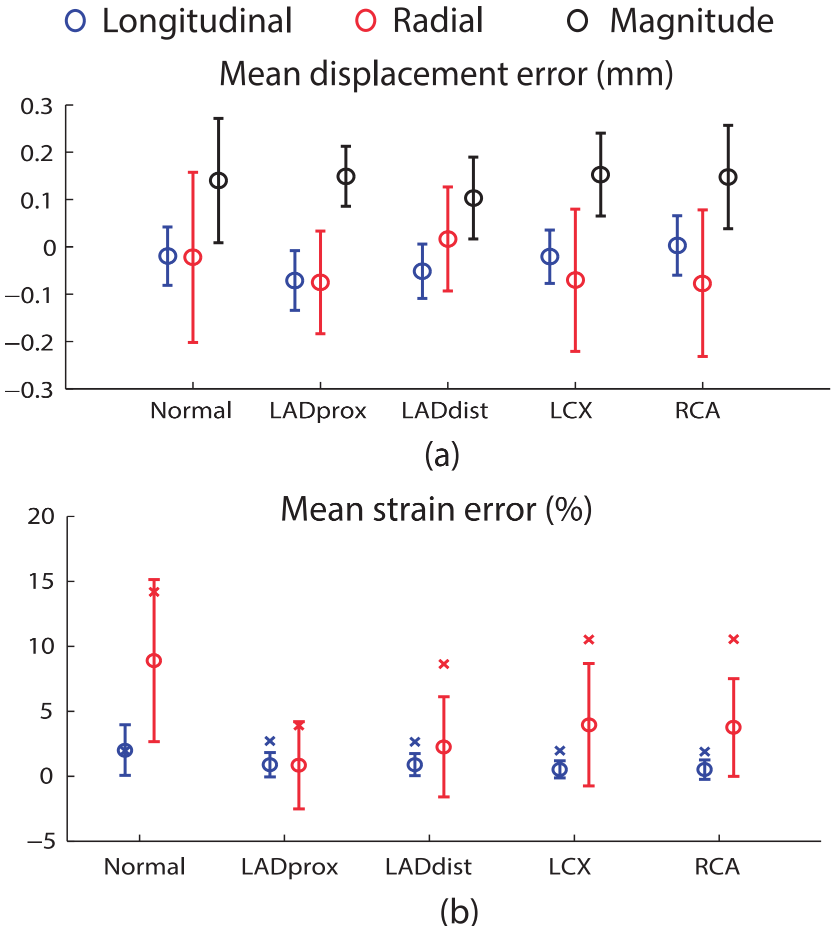

Figure 3.4: (a) Mean displacement and (b) strain errors and standard deviations for each synthetic case. The crosses in (b) represent the end-systolic strain errors for each case. Color image in the Appendix, page xxii.

(0.22 *mm*) when using 4 control points in the beam direction and 2 in the azimuth direction, so this setting was used for the rest of the experiments. In these experiments, as many spatial control points as intersections with image planes on the circumferential direction were used in the direction of β. Since 3 planes were acquired, 6 control points were used in that direction. Finally, as many temporal control points as B-mode frames available were used to model the velocity component perpendicular to the beam, and as many temporal control points as TD frames to model the velocity component in the beam direction.

Once the number of control points was optimized, we applied the proposed method to the synthetic cases simulating ischemia in different areas

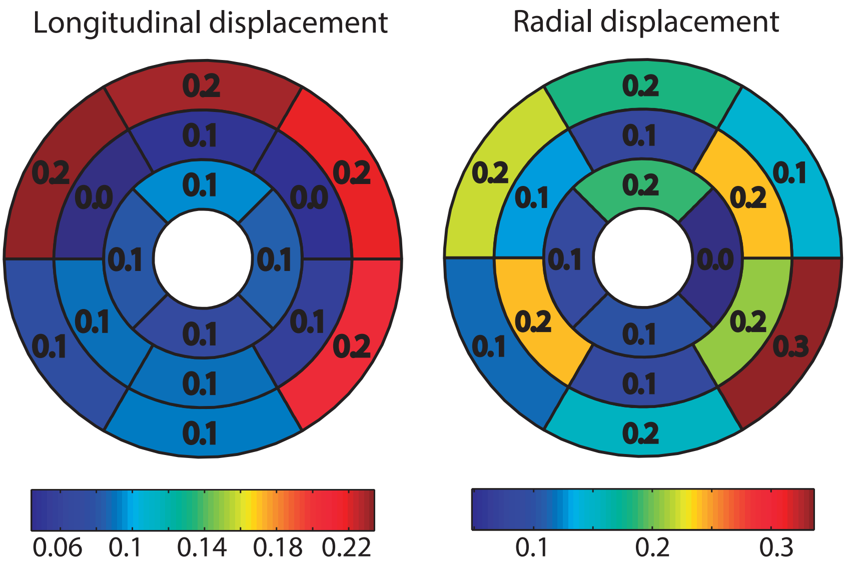

Figure 3.5: Absolute value of mean displacement errors (mm) averaged for all the synthetic cases. Color image in the Appendix, page xxiii.

of the left ventricle. After applying the estimated transformation to the segmented volumetric mesh, displacements and strains were calculated. In particular, for each tetrahedron, the displacement estimated at its vertices was interpolated at the cell center. Then, the Green-Lagrangian strain tensor was approximated as:

$$\varepsilon = \frac{1}{2}\left(\nabla\mathbf{u}^{T} + \nabla\mathbf{u} + \nabla\mathbf{u}^{T}\nabla\mathbf{u}\right), \tag{3.9}$$

where $\nabla\mathbf{u}$ represents the spatial derivative of the displacement vector. This approach was chosen to keep the coherence with the way the strain was approximated in the ground truth meshes. However, it could have been estimated by calculating the derivative of the continuous displacement field estimated at each vertex. Directional strains were calculated by projecting the strain tensor on the longitudinal and radial directions.

Figure 3.4 shows the longitudinal and radial displacement and strain errors, together with the magnitude of the displacement error (discarding the circumferential component) during the cardiac cycle for all the synthetic cases. Note that displacements and strains are calculated in the whole ventricle, not only in the areas where image data are available (i.e., the imaging planes). The mean displacement error for all the simulated cases was 0.14 ± 0.09 mm (-0.03 ± 0.06 mm in the longitudinal direction and -0.05 ± 0.14 mm in the radial direction). The mean longitudinal strain er-

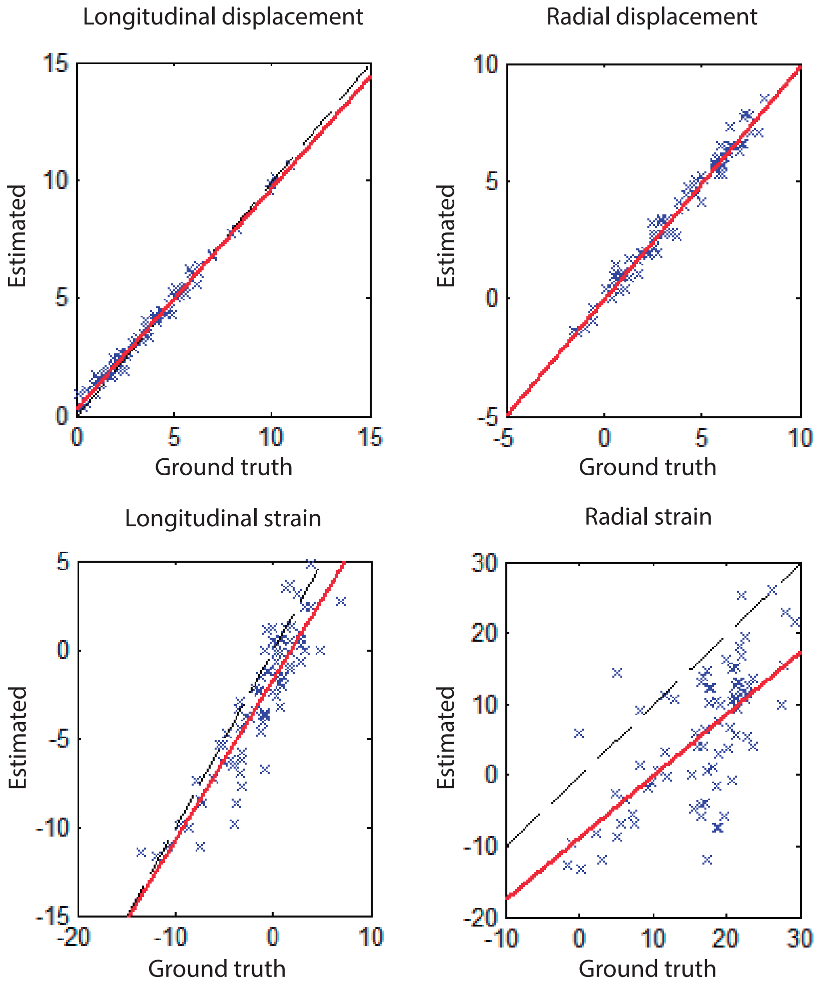

Figure 3.6: Linear regression for longitudinal and radial strain values.

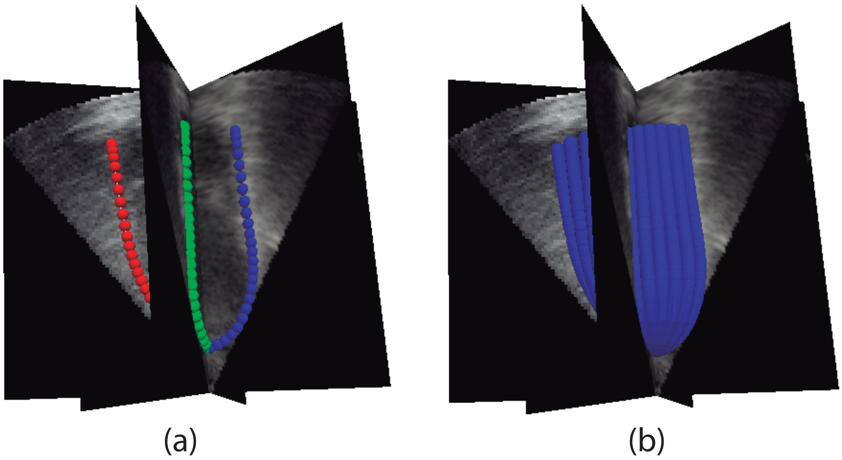

Figure 3.7: Example of the 3D interpolation to calculate segmental strain and displacements for one patient. (a) shows the initial segmented points at each plane, representing each of the segmentations with a different color. (b) represents the 3D interpolated shape of the left ventricle. Color image in the Appendix, page xxiii.

ror was 0.96 ± 1.03 % and the mean radial strain error was 3.94 ± 4.38 %. Figure 3.5 shows the spatial distribution for the absolute value of the directional displacement errors averaged for the 5 synthetic cases analyzed. In general, it can be observed that the maximum errors are located at the base of the wall, where the spatial resolution of the US images is lower.

Figure 3.6 represents the linear regression analysis of the end-systolic longitudinal and radial displacements and strains for each segment from the synthetic cases. A Pearson correlation coefficient of 0.99 was obtained for both the longitudinal and radial displacements, while values of 0.90 and 0.67 were obtained for the longitudinal and radial strains, respectively. A Student's t-test was used to compare the estimated displacements and strains with the ground truth values under the assumption that they are normally distributed. Normality assumptions were checked using a Lilliefors test for directional displacement and strain distributions. The Student's t-test concluded that the mean of the estimated and ground truth end-systolic displacement values were not significantly different for $p < 0.05$. In the case of the longitudinal and radial end-systolic strain values, we found that means were significantly different. In this case, a bias of $-2.24 \pm 0.41\%$ was obtained for longitudinal strains and $-9.56 \pm 3.74\%$ for radial strains.

Finally, experiments testing the influence of the orientation of the planes acquired on the results were also performed. In this case, for each synthetic case, a dataset where the images were rotated 30° in the circumferential

Table 3.2: Specifications of the B-mode images acquired from real cases.

	1	2	3
Frames/cycle	16	19	14
Frame rate (Hz)	11.47	11.71	11.64
Beams	132	132	132
Samples/beam	529	488	407
Opening angle (°)	74.66	74.66	64.8
Depth (mm)	130	120.24	100

direction with respect to the previous dataset was generated. Differences between the displacements and strains estimated with both datasets were lower than the average errors obtained previously. In particular, mean displacement differences of 0.10 ± 0.07 mm (0.01 ± 0.05 mm in the longitudinal direction, and 0.03 ± 0.09 mm in the radial direction) were found. The mean strain differences between both datasets were 0.11 ± 0.28 % in the longitudinal direction and 2.96 ± 2.70 % in the radial direction.

3.3.3 Experiments with real data

The proposed method was also tested on multi-plane image data from three real subjects. Table 3.2 and Table 3.3 show the specifications of the images acquired from every patient. For each case analyzed, the centerline of the left ventricular wall was delineated from each acquired plane using a cubic B-spline curve. To delimit the three-dimensional area where displacements and strains were estimated, linear interpolation between the delineated curves was done in the circumferential direction (β) using spherical coordinates. Figure 3.7 shows an example of 3D interpolation for one patient. After image registration, the strain tensor was calculated for all the points using Equation 3.9. This was then projected on the longitudinal and radial directions to obtain directional strain values.

The first case corresponds to a 58 years old male patient who presented a dilated ischemic cardiomyopathy after a transmural infarction in the lateral wall of the left ventricle. Visual analysis by clinical experts from the US images revealed a dilated left ventricle with slight reduction in the global systolic function. The patient also presented akinesia/dyskinesia in the lateral wall. Images from a Delayed Enhancement Magnetic Resonance (DE-MR) imaging study showed increased intensity in the middle and base of the lateral wall.

The presented method was applied to the sequence of US multi-plane B-

Table 3.3: Specifications of the TD images acquired from real cases.

	1	2	3
Frames/cycle	126	147	103
Frame rate (Hz)	97.09	98.04	99
Beams	32	32	32
Samples/beam	194	179	150
Opening angle (°)	74.66	74.66	65
Depth (mm)	130	120.68	100
Nyquist velocity (cm/s)	16	16	16
PRF (Hz)	1000	1000	1000

mode and TD images acquired. The strain curves calculated and averaged at every segment are shown in Figure 3.8. As it can be observed, reduced longitudinal strain values at end systole were found in the mid-lateral and antero-lateral wall because of the presence of ischemia (segments 7, 11 and 12). In this case, the reduction of the longitudinal strain at the base of the lateral wall is not as significant as in the mid-lateral area. One can also observe that not all segments contract synchronously, with the presence of post-systolic strain in the lateral and inferior wall (segments 4, 5 and 6). The radial strain curves also show a delayed thickening of the antero-lateral area (segments 1, 6, 7 and 12) with respect to the rest of the segments, reaching to higher radial strain value after end-systole at the base. Although the longitudinal strain curves obtained in the apical region are normal (ischemia was not found in the apical segments), the radial curve obtained for segment 13 (apical-anterior) shows an abnormal pattern. This could be due to tethering to the surrounding regions with abnormal radial strain patterns (segment 7).

The second case corresponds to a 49 years old male presenting scar at the base of the inferior wall and also ischemia and an aneurysm in the apical part of the inferior wall, with hypertrophic functional myocardium in the medial region. A DE-MR study of this patient presented increased intensity in the inferior wall. Figure 3.9 shows the strain curves obtained from the analysis of the multi-plane US images acquired for this patient. As it can be observed, reduced longitudinal contraction was found in the base of the infero-septal, inferior and infero-lateral wall (segments 3, 4 and 5, respectively), which was expected because of the presence of a scar. A globally reduced radial strain was also found in the whole inferior wall (segments 3, 4, 5, 9, 10 and 15). In the medial wall regions, high longitudinal contraction was estimated in segment 10, corresponding to the hypertrophic area of the

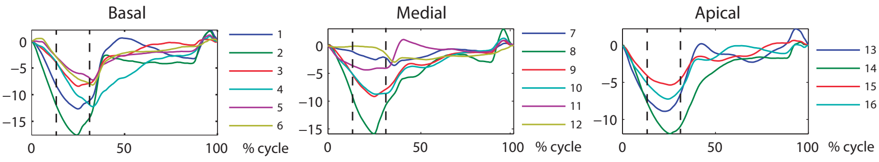

(a) Longitudinal strain curves

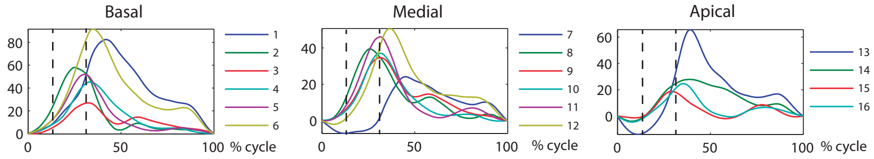

(b) Radial strain curves

Figure 3.8: (a) Longitudinal and (b) radial strain curves estimated for Case 1 (58 years old patient with ischemia in the infero-lateral wall). For each plot, the first dotted vertical line indicates aortic valve opening, while the second one indicates aortic valve closing. Color image in the Appendix, page xxiv.

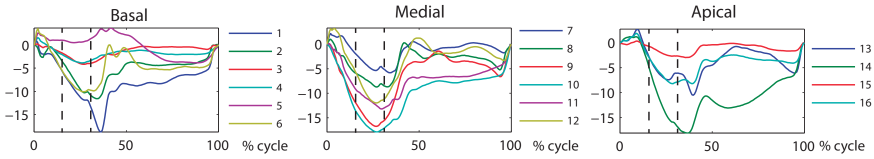

(a) Longitudinal strain curves

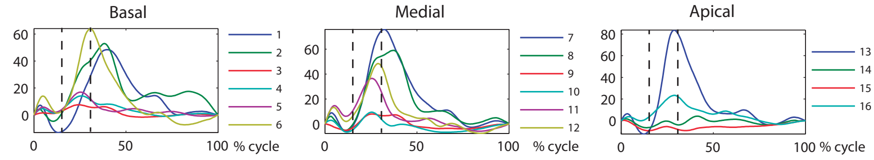

(b) Radial strain curves

Figure 3.9: (a) Longitudinal and (b) radial strain curves estimated for Case 2 (49 years old patient with ischemia in the inferior wall). For each plot, the first dotted vertical line indicates aortic valve opening, while the second one indicates aortic valve closing. Color image in the Appendix, page xxv.

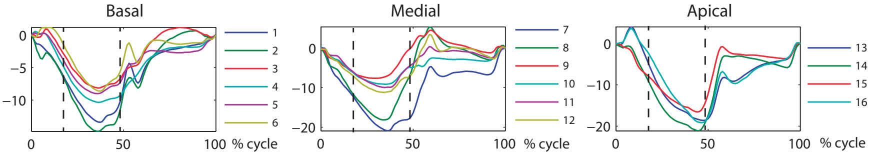

(a) Longitudinal strain curves

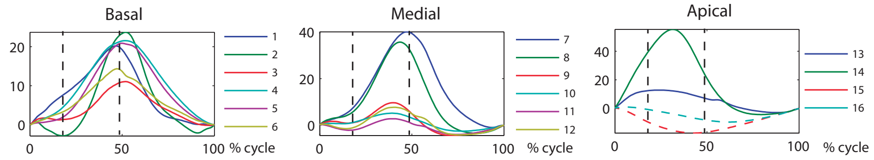

(b) Radial strain curves

Figure 3.10: (a) Longitudinal and (b) radial strain curves estimated for Case 3 (31 years old healthy volunteer). For each plot, the first dotted vertical line indicates aortic valve opening, while the second one indicates aortic valve closing. Dotted strain curves indicate areas that are not visible in the B-mode image sequence. Color image in the Appendix, page xxvi.

inferior wall. Abnormal strain patterns were found in the apical segments. In particular, segment 14 presented low radial strain and increased contraction during diastole, being its motion affected by the apical aneurysm. In the case of segment 15, almost no longitudinal contraction and radial tickening were found, which was also expected because of the ischemia identified in the inferior part of the apex.

Finally, a 31 years old healthy female volunteer was also analyzed. Results are presented in Figure 3.10. In this case, the B-mode image quality was very low in the medial and apical regions of the tri-plane images at 0 and -60 rotation degrees, being the apical region not visible in these planes as shown in Figure 3.11. Although radial strain could not be reliably estimated in segments 15 and 16, using TD images allowed estimating the longitudinal strain component. Radial strain patterns obtained at the medial segments were realistic. However, their magnitude at end systole may be underestimated because of the of low image quality close to segments 15 and 16 (i.e., segments 9, 10, 11 and 12). As it can be observed, neither pathological strain patterns nor dyssychrony between segments were found in this case, in contrast with Cases 1 and 2.

3.4 Discussion

The proposed method allows integrating multi-plane B-mode and TD images acquired interleaved for longitudinal and radial estimation of motion in the left ventricle. In contrast to most methods for motion assessment from US images, not only grayscale information is considered, but also quantita-

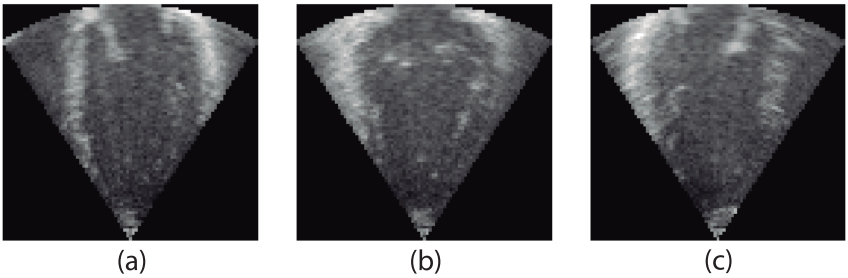
(a) (b) (c)

Figure 3.11: Multi-plane images of Case 3 at (a) 0, (b) -60, and (c) -120 rotation degrees (see Figure 3.2(a)).

tive information from TD. Since each type of information (B-mode and TD) as well as each plane are acquired interleaved and at different spatiotemporal resolutions, using a continuous representation both in time and space allows evaluating each of the data at the time and position it was acquired. This is in contrast to most approaches integrating different modalities and/or views [13], [14].

The proposed spherical representation of the transformation has two advantages on multi-plane images. First, it provides a topology in the circumferential direction that is very similar to the left ventricle's shape, allowing a more natural interpolation of information between the planes acquired. Second, one of the three orthogonal directions defining the spherical coordinate system corresponds to the beam direction. Since modeling a vector field using product tensor B-splines is equivalent to modeling each component of the vector separately, different grids can be used to model each component of the velocity field (see Equation 3.3 and 3.4). This separation between components lets us make use of the higher temporal resolution of TD images (since they provide information only in the beam direction) without being constrained by the lower temporal resolution of B-mode images in that direction, unlike in the method from Chapter 2.

Results from validation with a realistic synthetic dataset are presented in Figure 3.4, 3.5 and 3.6. In US apical images of the left ventricle, the cardiac wall is more aligned with the beam direction (as it can be observed from Figure 3.2), which is the direction in which TD provides information. Since the temporal sampling of multi-plane TD images is usually higher than B-mode images (see Tables 3.1, 3.2 and 3.3) and TD provides objective and quantitative information, the performance in the longitudinal direction was better compared to the radial direction. Although radial and longitudinal displacements accuracy is similar (mean errors of -0.05 ± 0.14 mm and -0.03 ± 0.06 mm for radial and longitudinal displacements, respectively), strain is very affected by small displacement errors and its estimation in the radial direction is less accurate than longitudinal strain (mean errors of 3.94 ± 4.38 % and 0.96 ± 1.03 % for radial and longitudinal strain, respectively). Different displacement and strain error magnitudes between the normal and pathological simulated cases can be explained because the ischemic simulations present globally reduced motion. Furthermore, displacement and strain differences in the results obtained by changing the orientation of the planes acquired were lower than the estimation error, so the method is robust to image rotations.

The method has also been applied to real data to show its applicability in a clinical environment. In particular, it has been shown that the motion estimation performed with the proposed framework can be useful to assess patients presenting ischemic cardiomyopathy. We also included results from one healthy volunteer where no pathological strain patterns were found. This example was also useful to show the benefits of using both B-mode and TD images together, since it was possible to assess longitudinal contraction in areas that were not visible in the B-mode image sequence (see Figure 3.10, segments 15 and 16).

In clinically available 3D US acquisition systems, images are created by integrating small volumetric information from different cardiac cycles. In some cases, such as patients with arrhythmia associated to ischemic cardiomyopathy, it is not possible to recover a useful 3D image because of the heart rate variability. Using the proposed method would be useful to overcome this limitation, since all the information comes from the same cardiac cycle. In addition, the use of information acquired simultaneously at different areas of the left ventricle allows assessing temporal relations between events that occur at different regions. For example, it can be observed from Figure 3.8 (a) that segments 4, 5 and 6 reach their maximum longitudinal contraction when the remainder basal segments already started to relax.

The limitations of the framework are related to the sparse spatial information that is available. Although our experiments showed that ventricular motion can be estimated using tri-plane images, the circumferential component cannot be recovered with the presented approach. Moreover, if a small akinetic/dyskinetic region is present between two planes acquired, it would not be possible to detect it.

3.5 Conclusions

A continuous registration framework integrating multi-plane B-mode and TD images acquired interleaved with different orientations and spatiotemporal resolutions has been presented. Higher temporal resolution in the beam direction was achieved by modeling separately the different components of the velocity field. The experiments with synthetic data showed that displacement and strain estimation is accurate and experiments with real patients illustrated the applicability of the proposed method to clinical cases.

CHAPTER 4

Interventional endocardial motion estimation from electro-anatomical mapping data

Scar presence and its characteristics play a fundamental role in several cardiac pathologies. To accurately define the extent and location of the scar is essential for a successful ventricular tachycardia ablation procedure. Nowadays, a set of widely accepted electrical voltage thresholds applied to local electrograms recorded are used intra-operatively to locate the scar. Information about cardiac mechanics could be considered to characterize tissues with different viability properties. In this chapter, a novel method to estimate endocardial motion from data obtained with an electro-anatomical mapping system together with the endocardial geometry segmented from pre-operative 3D magnetic resonance images is proposed, using a statistical atlas constructed with bilinear models. The method was validated using synthetic data generated from ultrasound images of 9 volunteers and was then applied to 7 ventricular tachycardia patients. Maximum bipolar voltages, commonly used to intra-operatively locate scar tissue, were compared to endocardial wall displacement and strain for all the patients. The results show that the proposed method allows estimating endocardial motion and strain, and that areas with low voltage electrograms also present low strain values.

The content of this chapter is adapted from the following publication:

A. R. Porras, G. Piella, A. Berruezo, C. Hoogendoorn, D. Andreu, J. Fernandez-Armenta, M. Sitges, and A. F. Frangi. Interventional endocardial motion estimation from electroanatomical mapping data: Application to scar characterization. IEEE Transactions on Biomedical Engineering, vol. 60, pp. 1217-1224. 2013.

4.1 Introduction

Both ischemic (IC) and non-ischemic cardiomyopathy can lead to myocardial necrosis and ventricular tachycardia (VT). Necrosed myocardium is replaced by fibrotic tissue constituting myocardial scars. Because of a low blood supply, areas of fibrosis appear in the myocardium. These fibrotic/scarred areas are characterized by low voltage in intracardiac electrograms and low contractility. It is currently well established that the underlying cause of VT is the presence of conducting channels, which are corridors of border zone tissue connecting healthy myocardium and surrounded by dense fibrotic tissue, also called “scar core”. These conducting channels create a re-entrant circuit where electrical impulse is propagated slowly. When VT cannot be successfully controlled with antiarrhythmic drugs, catheter ablation targeted to these slow conduction channels has been demonstrated to be a good option to treat the tachycardia [52, 53]. Therefore, intra-operative scar characterization is a key factor for an effective treatment.

In the last years, the use of Electro-Anatomical Mapping Systems (EAMS) as an aid in the treatment of this pathology has increased considerably. These systems are used to guide radio-frequency ablation procedures using a catheter. This catheter is introduced into the left ventricle through the blood vessels and, by means of an external tracking system, the position of the catheter tip at every sampled instant is captured.

The catheter also records the local electrogram when it is in contact with the endocardial wall and then, according to these electrograms, tissues with different electrical properties are identified. However, this method has inherent limitations to accurately characterize the tissue, such as the far-field effect, catheter positioning and orientation, inter-electrode distance and the mapping resolution. Therefore, there is a mismatch between the scar tissue characterization based on standard voltage thresholds and based on DE-MR imaging [54, 55, 56], which is a widely used modality to locate the scar pre-operatively. As a result, scar characterization solely based on voltage electrogram criteria highly depends on the electro-physiologist’s expertise.

Mechanical tissue properties could provide additional information to improve scar characterization. Specifically, deformation information could help to characterize scar in patients with IC, since scar regions may present normal displacement due to tethering to normally contracting adjacent regions [57], while deformation will be solely affected by the mechanical properties and real shortening and lengthening of the myocardium. These are directly related to the characteristics of local electrical activation.

However, widely used EAMS do not show any endocardial motion information. In addition, because of the limited number of points that are usually acquired, the spatial resolution is too low to reconstruct the endocardial shape with enough accuracy, so data interpretation also depends on the cardiologist's experience.

4.1.1 State of the art

Recently, some research groups have been looking into different ways of using mechanical information obtained intra-operatively to guide catheter interventions. In [17], a novel technique to combine electrical activation and motion information from EAMs as part of the NOGA system (Biologics Delivery Systems Group, Cordis Corporation, Irwindale CA, USA) was presented. An indicator of endocardial contraction (linear local shortening) was proposed in [18] and many therapeutic utilities, such as revascularization and applications in gene therapy and cell transplantation, were discussed.

In [19], a methodology to obtain endocardial motion from EAMS was proposed, and the possibility of identifying motion patterns to predict septal flash was shown. In [16], a correlation between both circumferential shortening derived from NOGA system and the one obtained with US images was found. Their results showed the possibility to distinguish between normal, hyperkinetic and hipokinetic myocardium with an acceptable accuracy, even though an overlap between classes was found. The ability of electromechanical maps acquired with an EAMS to differentiate between infarcted and healthy myocardium was tested in [15], based on a reduction of both electrical and mechanical activity.

However, some studies conclude that the use of mechanical tissue properties directly estimated from EAMS has restrictions. The ability of left ventricle electromechanical mapping to distinguish between viable and non-viable myocardium in patients with IC was evaluated in [58]. According to their results, the linear local shortening calculated with NOGA did not differentiate accurately between viable and non-viable tissue. Moreover, the study of [55] demonstrated significant spatial heterogeneity of both endocardial voltage and linear local shortening derived from the NOGA system in normal and viable dysfunctional myocardium.

The main problem when evaluating tissue mechanical properties from EAMS is that catheter position data contains components not related to cardiac motion, such as respiration motion, catheter sliding over the endocardial wall and measurement errors of the tracking system. In addition, the amount of acquired points does not provide a reliable shape reconstruction, since it is too low. Moreover, the points are often very concentrated in a small region of interest.

We propose to extract the shape of the endocardium from a pre-operative

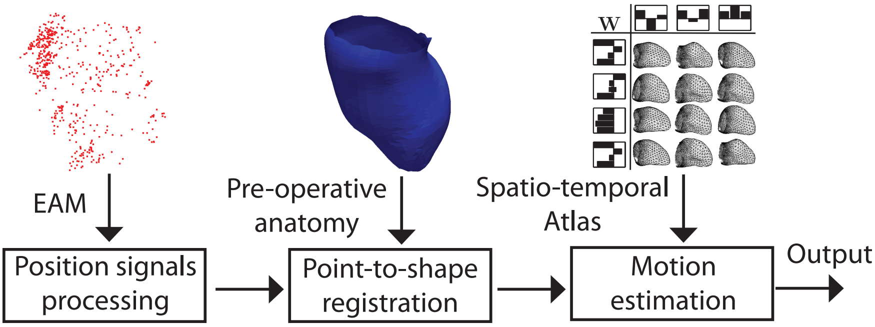

Figure 4.1: The basic workflow. Processed EAM data are registered to the segmented endocardial shape. An atlas is used to help reconstructing motion in areas where there is no motion information.

3D imaging modality and use it together with the temporal and the spatial information provided by an EAMS to reconstruct the endocardial motion for one cardiac cycle. To estimate motion in areas without information from the EAMS, a bilinear statistical atlas [59] of left ventricle endocardial shapes is used. The novelty of the proposed method consists in the use of prior knowledge of the patient's endocardial shape, and the application of a population-based atlas that encodes separately shape and motion, which allows estimating the endocardial motion at any point of the endocardium given the ventricle's shape and some localized motion information. This method could be used intra-operatively together with an EAMS for guidance during the intervention.

4.2 Methodology

The proposed method is composed of three stages, as shown in Figure 4.1. First, EAM data were processed to filter out undesired components in the position signals. The second step was oriented to project EAM information over a patient-specific endocardial shape extracted from any 3D pre-operative imaging technique. Finally, a statistical model was used to propagate motion in the regions where there is no information from the EAMS.

4.2.1 EAM data description

EAMs usually consist in a list of acquired points, each including both position and electrical information. Thus, during the acquisition of a point, an EAMS records the position of the catheter tip, the electrical signals acquired with the catheter electrodes, and the superficial ECG signals recorded for a period of time.

For this study, we used electro-anatomical data obtained with Carto (Biosense Webster, Haifa, Israel) EAMS. These maps consist of points with electrical signals sampled at 1 KHz during 2.5 s and 3D catheter position signals sampled at 100 Hz.

4.2.2 Position data processing

To compensate most of the artifacts present in the position signals, we applied a Butterworth band-pass filter [60]. The high-pass threshold used for each position signal varies depending on the heart beat duration when it is acquired. Heart rate is calculated from the ECG signals and is set as high-pass threshold for the filter, since all motion components must have a higher frequency. The low-pass threshold was set to 20 Hz to minimize the effect of the noise associated to high frequencies.

Both electrical and position signals are acquired synchronously, although with different sampling rates. However, since heart rate is not always the same, there is a lack of motion synchronization among different points away from the R peak of the electrocardiogram, which is the trigger the system uses to acquire information. Therefore, we identify one cardiac cycle for each point by looking for two consecutive R-peaks in the ECG signal. Then, the position signal during this cycle is extracted and resampled to 200 samples. Since position information is sampled at 100 Hz, no loss of information occurs for beat durations below 2 s.

4.2.3 Points-to-shape registration

Once EAM position signals are filtered and synchronized, endocardial motion for the points acquired with the EAMS is reconstructed. However, since these points are usually highly concentrated in a specific region of interest, it is not possible to accurately reconstruct the entire endocardial shape. Therefore, we obtained the geometry of the left ventricle endocardium from MR images by using a model-based segmentation algorithm based on [61], trained with MR datasets. We used this modality because its acquisition is included in the clinical protocol for electro-physiology interventions, but any other imaging modality could be used. The number of points in the segmented meshes was 880.

An Iterative Closest Point (ICP) [62] based registration algorithm is used to register the points from EAM data and the shape of the endocardium. For a better result, a landmark-based rigid registration was done for initialization before running the ICP algorithm. In this study, we set two landmarks close to the aorta and one in the apex manually.

4.2.4 Endocardial motion estimation

Motion signals from EAM data could be directly used to deform the endocardium after registration, interpolating those areas where no motion information is provided. However, because of the complexity of heart motion, it would not be realistic to interpolate motion on the remainder endocardium, so it is necessary to have some additional knowledge on the behavior of the endocardium in order to reconstruct its entire motion pattern.

To this end, a bilinear shape model [59] was used. This model codes separately shape and motion, as illustrated in Figure 4.2, so it is very appropriate to estimate motion given the shape of the subject's endocardium and some sparse motion information. Using this model, the shape of one subject's endocardium at a given phase of the cardiac cycle can be estimated as:

$$\mathbf{y_i^s} = (\mathbf{W}\mathbf{b_i})^{\mathbf{VT}}\mathbf{a^s} \tag{4.1}$$

where $\mathbf{y_i^s}$ is the vectorized shape of the subject s at the phase i of the cardiac cycle, $\mathbf{a^s}$ is a parameter vector representing the characteristics of the subject s, $\mathbf{b_i}$ is a parameter vector representing the phase i of the cardiac cycle, $\mathbf{W}$ is a constant matrix governing the interaction between the factors, and the superscript VT denotes the vector transpose operation as explained in [59]. The bilinear model used in this work has been constructed from 80 patients with different pathologies and dividing the cardiac cycle in 15 different phases.

The objective is to use the endocardial shape segmented from MR images to find the subject parameters $\mathbf{a^s}$. Once these parameter are known, we use the motion signals obtained from the EAM data to calculate the parameters $\mathbf{b_i}$ that describe the motion of the endocardium at the different phases of the cardiac cycle.

Since all shapes were aligned using Procrustes method when constructing the atlas, the segmented endocardial shape had to be re-scaled and aligned to the shapes used to build the atlas using a rigid-registration. Then, since the endocardial shape is acquired at end diastole, it can be used together with the $\mathbf{b_0}$ vector representing the end-diastolic phase in the atlas to solve for $\mathbf{a^s}$:

$$\mathbf{a^s} = \left((\mathbf{W}\mathbf{b_0})^{\mathbf{VT}}\right)^{-\mathbf{1}}\mathbf{y_0^s}. \tag{4.2}$$

Once the subject is instantiated (parameters in $\mathbf{a^s}$ are calculated), it is necessary to solve for the parameters describing the endocardial motion. After registering the cloud of points from the processed EAM data to the endocardial shape, there is a correspondence between the points in the cloud

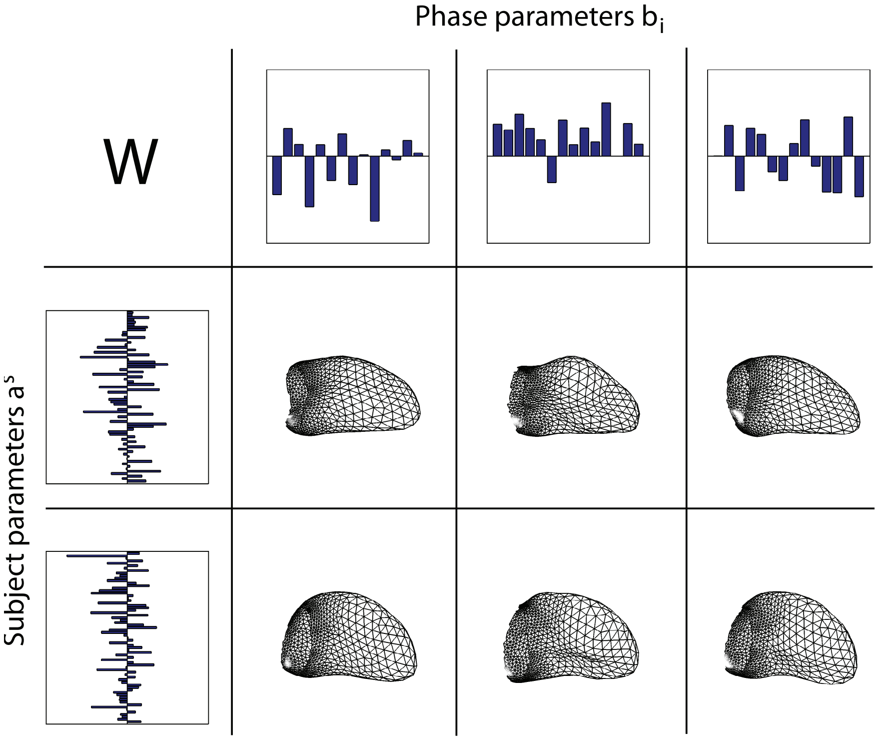

Figure 4.2: The structure of the bilinear model. Along the horizontal axis, three phases from the cardiac cycle are shown. Along the vertical axis, two different subjects are represented.

and the ones in the shape. Therefore, we have the motion signals of some sparse points in the endocardium and we can use them to solve for the phase parameters $\mathbf{b_i}$ according to the following equation obtained from Equation 4.1:

$$\mathbf{b_i} = \left((\mathbf{W}^{*\mathbf{VT}} \mathbf{a}^{\mathbf{s}})^{\mathbf{VT}} \right)^{-\mathbf{1}} \mathbf{y}_{\mathbf{i}}^{*\mathbf{s}}. \tag{4.3}$$

where $\mathbf{y}_{\mathbf{i}}^{*\mathbf{s}}$ contains only the points of the shape with motion information from the EAM data, and the $\mathbf{W}^*$ matrix contains only the interaction of the factors for those points included in $\mathbf{y}_{\mathbf{i}}^{*\mathbf{s}}$.

Once both $\mathbf{a}^{\mathbf{s}}$ and $\mathbf{b_i}$ parameters have been estimated, Equation 4.1 can be used to reconstruct the endocardium for every phase of the cardiac cycle. Thus, displacement and strain information can be estimated for one full cardiac cycle.

4.2.5 Endocardial strain estimation

Let **u** be the displacement vector of a point at certain phase of the cardiac cycle, obtained by using end-diastolic position as reference. Then, the Green-Lagrangian strain tensor ε can be calculated using the following equation:

$$\varepsilon = \frac{\mathbf{1}}{\mathbf{2}}(\bigtriangledown\mathbf{u}^{\mathbf{T}} + \bigtriangledown\mathbf{u} + \bigtriangledown\mathbf{u}^{\mathbf{T}} \bigtriangledown \mathbf{u}) \tag{4.4}$$

where $\bigtriangledown\mathbf{u}$ denotes the spatial derivative of the displacement vector. To calculate it, the displacement vector is interpolated in every triangle of the segmented mesh from the known displacement vectors of its vertices. Then, the displacement vector function is spatially derived at the center of the triangle.

The strain tensor was projected in both longitudinal and circumferential directions to obtain local directional strains. Radial direction vector was defined as the normal vector to each triangle. The longitudinal direction vector was estimated as perpendicular to radial direction and maximizing its scalar product with the base-apex vector. Then, the circumferential direction was calculated as vectorial product of radial and longitudinal direction vectors. The radial strain cannot be reliably estimated in this case because there is only endocardial motion information and, therefore, no information about wall thickening is available.

4.3 Experiments

The proposed method was validated using synthetic data and then applied to real cases.

4.3.1 Generation of synthetic data

We generated synthetic EAM data based on geometries extracted from 3D+t US images to validate our method. For this, we used image data from 9 volunteers. The endocardium was segmented from these images using the method presented in [63] and the Temporal Diffeomorphic Free Form Deformation (TDFFD) algorithm [27] was used to track endocardial motion. Then, from the estimated motion, a set of points simulating those acquired with an EAMS was generated.

The number of points generated for every dataset was chosen as a random number between 100 and 300, which is in accordance with the maps that are normally acquired in an electro-physiology intervention and with the data we used for the experiments with patient data. In addition, the location of every generated point was also selected randomly.

Since the points in an EAM are acquired independently, the heart rate varies when recording different points. Therefore, a random beat duration

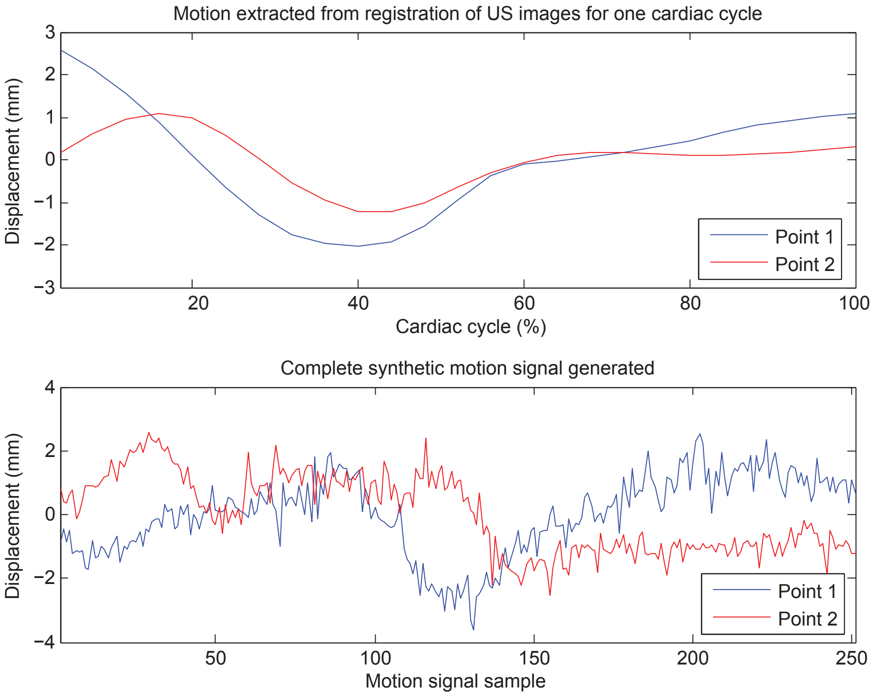

Figure 4.3: On the top image, motion signals extracted from 3D+t US images for 2 different points. On the bottom image, synthetic motion signals generated with 251 samples for the same points. Color image in the Appendix, page xxvii.

between 800 ms and 1.2 s has been assigned to every synthetic point. The motion signals for every point were created so that their duration is 2.5 s with a sampling rate of 100 Hz, to mimic the maps obtained from Carto. For the same reason, all motion signals were set so that they reach their end-diastolic position at t=2 s, which is the time instant Carto uses to synchronize all points.

After generating the motion signals, some undesired motion components (as the ones recorded when tracking catheter motion) have also been simulated and added to the motion signals:

1. Respiratory motion was simulated as a sine wave with a random duration between 1.6 s and 4 s, and a random phase.

2. Random position measurements noise was generated by creating random displacements at every sample in random directions with a maximum magnitude of 1 mm, according to the accuracy reported with Carto [64].

Finally, ECG synthetic signals were generated for every point, so that their R-peaks coincided with the end-diastolic position of the generated motion signals.

An example of synthetic motion signals generated for two different points in the endocardium is shown in Figure 4.3.

4.3.2 Validation with synthetic data

Five synthetic EAMs were created for each one of the nine volunteers used for this study. Then, the proposed method was applied to reconstruct endocardial motion during one cardiac cycle.

The ventricle was divided according to the AHA 17-segments model [49]. Displacement and strain curves were averaged in every segment and projected into the longitudinal, circumferential and radial directions. Normalized cross-correlation was calculated to compare the displacements and strains estimated using the proposed method against the curves obtained from TDFFD registration. Figs. 4.4 and 4.5 show the normalized cross-correlations obtained for displacement and strain curves respectively, projected into different directions.

To test whether our method was able to perform similar motion reconstructions for the same patient, the mean standard deviation between the curves obtained from the five different synthetic data generated for each patient was calculated. The distribution of these standard deviations for all the cases is shown in Figure 4.6 and 4.7 for both displacement and strain estimation.

4.3.3 Experiments with clinical data

Once the proposed methodology was validated using synthetic data, we applied it to 7 patients to test whether the endocardial motion reconstruction allowed identifying the presence of scar.

5 patients presented IC (4 with prior inferior myocardial infarction and one with anterior myocardial infarction) and 2 patients presented a non-ischemic cardiomyopathy. All patients were men with a mean age of 65.3 ± 11.5 years. The EAMs acquired contained 332 ± 141 points.

All patients underwent a cardiac magnetic resonance examination previously to the VT ablation procedure using a 3T clinical scanner (Magnetom Trio, Siemens Healthcare) equipped with cardiac dedicated software and a cardiac 12-element phased array coil. Image acquisition was ECG gated to end-diastole to minimize cardiac motion. Respiratory synchronization was performed for every other heart beat using a crossed pair navigator approach. The 3D slab was acquired in the transaxial direction, with a mi-

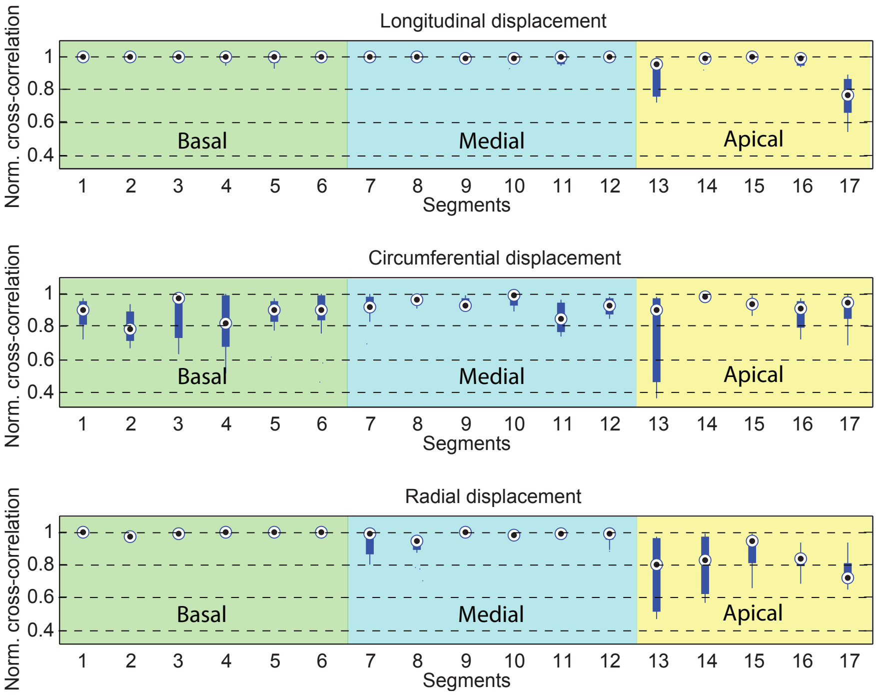

Figure 4.4: Distribution of the normalized cross-correlations between the reconstructed motion curves obtained from the synthetic data and the ones from the original data for every AHA model segment. Circles represent the median, thick lines represent the first and third quartile and thin lines represent the remainder values.

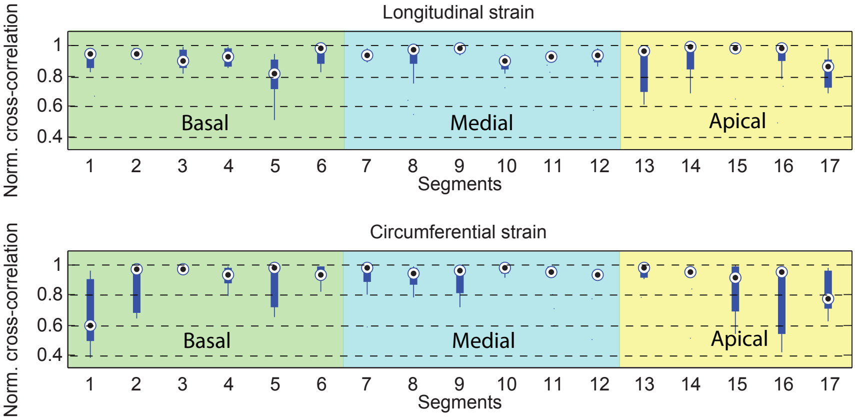

Figure 4.5: Distribution of the normalized cross-correlations between the reconstructed strain curves obtained from the synthetic data and the ones from the original data for every AHA model segment. Circles represent the median, thick lines represent the first and third quartile and thin lines represent the remainder values.

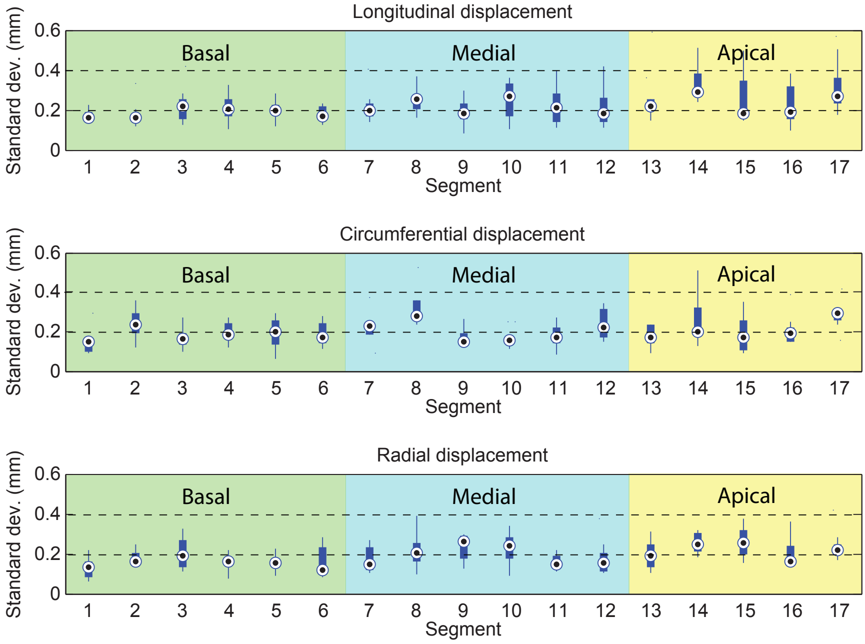

Figure 4.6: Distribution of the mean standard deviations between displacements estimated from the five different experiments performed for the same case. Circles represent the median, thick lines represent the first and third quartile and thin lines represent the remainder values.

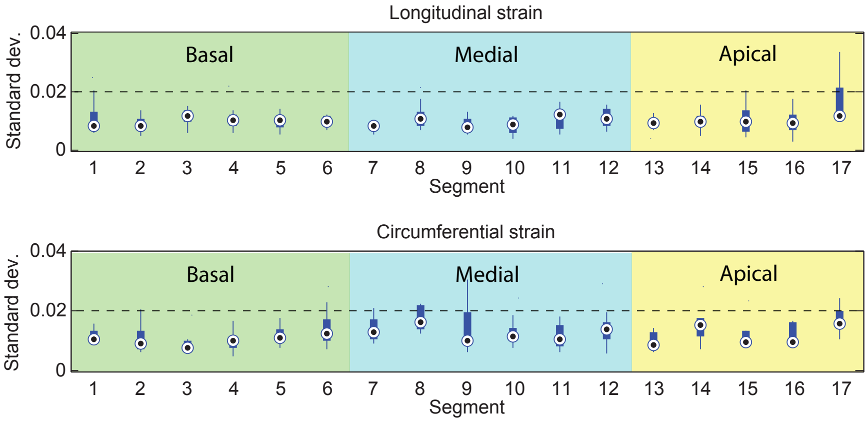

Figure 4.7: Distribution of the mean standard deviations between strains estimated from the five different experiments performed for the same case. Circles represent the median, thick lines represent the first and third quartile and thin lines represent the remainder values.

nimized field of view and a 256 x 256 pixels matrix size. Slice thickness was set at 1.4 mm with 20% overlap (0.28 mm) between slices to yield an isotropic spatial resolution of 1.4 x 1.4 x 1.4 mm and to allow for image reformatting in the left ventricle short axis orientation for subsequent image processing.

From each mapped point, one beat was extracted separately and local activation time and maximum bipolar and unipolar voltages were calculated from this. After points-to-surface registration, those electrical values were interpolated in the entire mesh using radial basis functions. Segments with scar core were defined as those with mean maximum bipolar voltage lower than 0.5 mV [65]. Segments without scar core were defined as those with mean maximum bipolar voltage higher than 1 mV [66]. Displacement projections in longitudinal, circumferential and radial directions, together with longitudinal and circumferential strains, were also averaged for every segment.

Mean longitudinal strain values were compared between segments defined as scar core and those defined as healthy with a Student's t-test, assuming the normal distribution of the values. Normality assumptions were checked using a Lilliefors test.

Longitudinal strain distributions and a 95% mean confidence interval for the true difference of the means are shown in Figure 4.8. Mean longitudinal strains for scar core and healthy segments were significantly different, with $p < 0.05$.

Circumferential strain values were also compared between scar core and healthy segments (Figure 4.9). In this case, mean circumferential strains for scar core and healthy segments were not found to be significantly different with $p < 0.05$.

As an illustrative example, Fig 4.10 shows longitudinal strain at end systole and both maximum bipolar and unipolar voltages at end diastole for one ischemic patient.

4.4 Discussion

A method has been presented to estimate endocardial motion from electroanatomical mapping data and the endocardial shape obtained from any preoperative 3D imaging modality.

Displacement and strain were estimated from synthetic data generated from 3D+t US images. Normalized cross-correlations between the estimated values and the ground truth were good in average. However, the obtained results were not homogeneous in all directions where displacement/strain were projected.

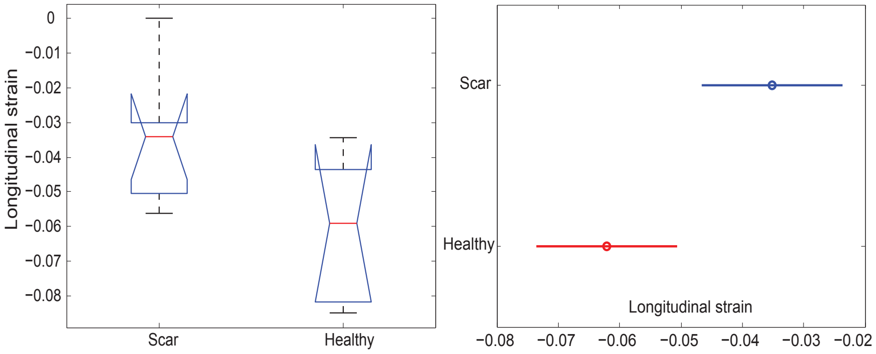

Figure 4.8: On the left, the distribution of longitudinal strain values for scar core and healthy segments. The central line indicates the median, the edges represent the first and third quartile, and the whiskers extend to the most extreme data values. On the right, 95% mean confidence interval for the true difference of mean longitudinal strains.

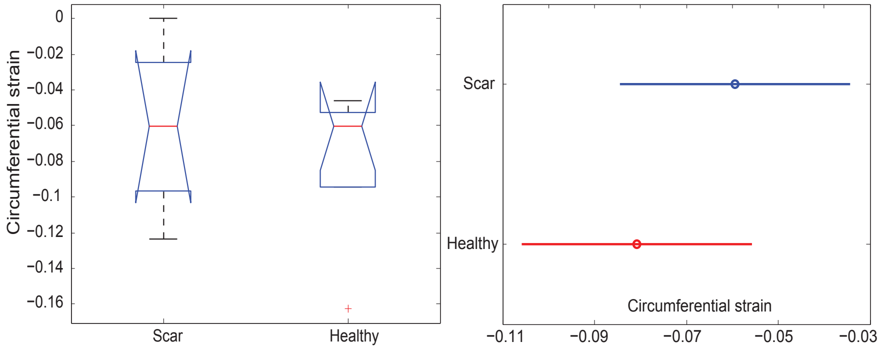

Figure 4.9: On the left, the distribution of circumferential strain values for scar core and healthy segments. The central line indicates the median, the edges represent the first and third quartile, and the whiskers extend to the most extreme data values. On the right, 95% mean confidence interval for the true difference of mean circumferential strains.

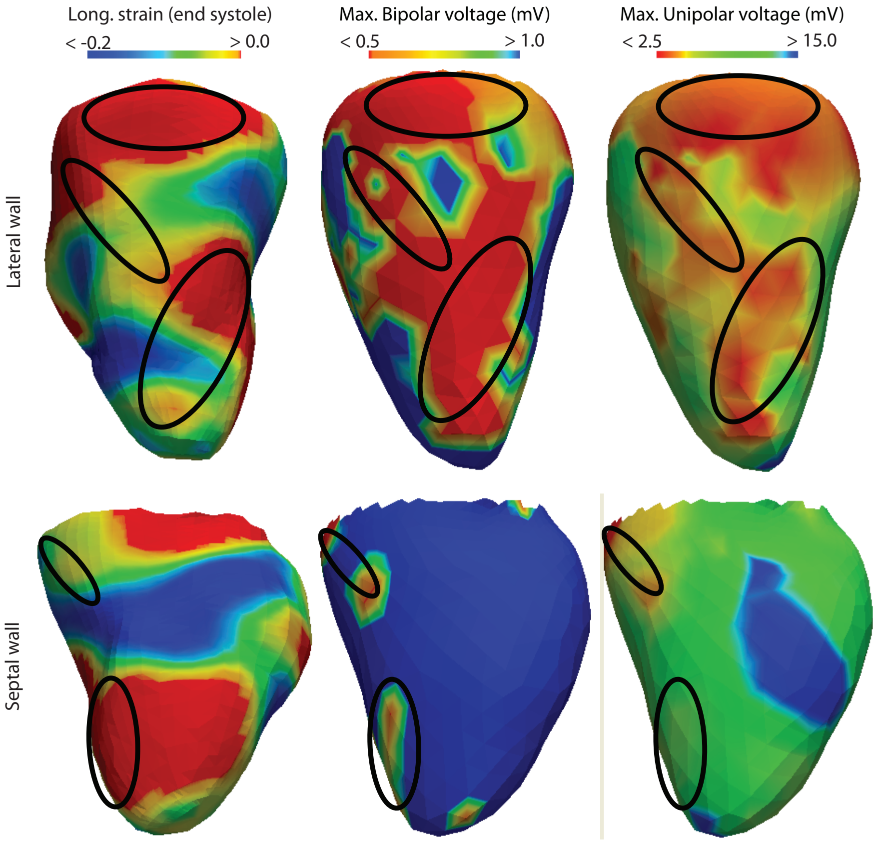

Figure 4.10: Comparison of longitudinal strain at end systole (left), maximum bipolar (center) and maximum unipolar (right) voltages interpolated at the end-diastolic phase for one ischemic patient. On the top row, a view of the left ventricle from the lateral wall. On the bottom row, a view from the septal wall. Red color represents tissue classified as scar core. Blue color represents tissue classified as healthy. Black oval lines represent the areas where scar core is present according to bipolar thresholds. Color image in the Appendix, page xxviii.

When looking at longitudinal displacements, the correlation was over 95% in most of the cases, being its behavior slightly worse in the apex (segment 17).

Regarding radial displacements, the results are similar to longitudinal displacement in the basal and medial segments. In the apical segments (segments 13 to 17), normalized cross-correlation can vary from 50% to 95%. It may be due to the fact that the apical region was not completely present in the US images used to generate the synthetic EAMs. This may have affected the performance of the TDFFD algorithm in this area, thus compromising the reliability of the ground truth in the apical segments.

Although the normalized cross-correlation for circumferential displacements is high in average (close to 90%), its variation is higher than in the other two directions. This may be explained because the bilinear atlas was built from CT images, which do not capture circumferential motion reliably. This problem can be alleviated by using another atlas constructed from US or tagged-MR images, which do capture circumferential motion, but at a cost of anatomical detail.

For longitudinal and circumferential strains, normalized cross-correlations present a similar behavior than in the case of the displacements, but with lower magnitudes. This is in accordance with the expected results, since the strain is a differential measure based in the displacement field.

The repeatability of the method was also tested by generating different synthetic EAM datasets on the same subject's geometry and checking whether the same motion reconstruction was obtained for all of them. The mean standard deviations of the estimated displacement and strain signals were calculated. Standard deviations for motion were always found to be below 0.6 mm. It can be considered a satisfactory result, taking into account that the random tracking error introduced had a magnitude of 1 mm [64]. Regarding strain, the mean standard deviation in both longitudinal and circumferential directions was also below 3%.

The results obtained for the studied patients show how the estimation of longitudinal strain can help to distinguish scar core regions from healthy areas according to maximum bipolar voltages, despite some overlapping between ranges. This is in agreement with other studies, where longitudinal strain is also used to delineate the scar [67, 68].

In the example shown in Figure 4.10, it can be observed how the presence of low longitudinal strain values in end systole is related to low bipolar and unipolar voltages, although with some mismatches as found in the results presented in Figure 4.8.

On the other hand, the estimated circumferential strain does not seem to discriminate well. One possible reason is that, as it was concluded before from the experiments with synthetic data, some errors are introduced in the circumferential direction. Hence, The circumferential strain estimated is not as reliable as the longitudinal strain. Moreover, possible errors introduced when recording local electrograms have to be considered, since electrical parameters derived from them are used to classify tissue as scar core or healthy.

Finally, it is worth mentioning that the proposed method could be used intra-operatively, as both registration and recalculation of the bilinear equations after the acquisition of every new electro-anatomical point can be done in a fraction of a second for the size of the model we are using. Furthermore, since the solution of the equations at every time instant is independent from the others, the method can be parallelized. In this particular case, each linear system of equations took less than one second to solve on an Intel Core i7 CPU 3 GHz with 6 GB of RAM, using a C++ implementation.

4.5 Conclusions

A novel method to estimate endocardial motion intra-operatively from electro-anatomical data has been proposed in this chapter. Validation against synthetic data shows that the proposed method is reliable and repeatable. Moreover, the results of its application to real cases show that the use of the estimated mechanical information can help to characterize endocardial tissue intra-operatively, which is of great importance for electro-physiology interventions such as catheter ablation.

CHAPTER 5

Pre to intra-operative data fusion framework for multimodal characterization of myocardial scar tissue

Merging multimodal information about myocardial scar tissue can help electrophysiologists to find the most appropriate target during catheter ablation of ventricular arrhythmias. In this chapter, a framework is presented to analyze and combine information from DE-MR imaging and electro-anatomical mapping data. Using this information, electrical, mechanical and image-based characterization of the myocardium is performed. The presented framework allows the left ventricle to be segmented from DE-MR images and the scar to be characterized prior to the intervention based on image information. It allows the electro-anatomical maps obtained during the intervention from a navigation system to be merged together with the anatomy and scar information extracted from DE-MR. It also allows for the estimation of endocardial motion and deformation to assess cardiac mechanics. Therefore, electrical, mechanical and image-based characterization of the myocardium can be performed. The feasibility of this approach was demonstrated on three patients with ventricular tachycardia associated to ischemic cardiomyopathy by integrating images from DE-MR and electro-anatomical mapping data in a common framework for intra-operative myocardial tissue characterization. The proposed framework has the potential to guide and monitor delivery of radiofrequency ablation of ventricular tachycardia. It is also helpful for research purposes, facilitating the study of the relationship between electrical and mechanical properties of the tissue, as well as with tissue viability from DE-MR.

The content of this chapter is adapted from the following publication:

A. R. Porras, G. Piella, A. Berruezo, J. Fernandez-Armenta, and A. F. Frangi. Pre to Intraoperative Data Fusion Framework for Multimodal Characterization of Myocardial Scar Tissue. IEEE Journal of Translational Engineering in Health and Medicine, vol. 2, pp. 1-11. 2014.

5.1 Introduction

Catheter ablation is a procedure used to treat some types of arrhythmia, when drug therapies are not effective. One type of arrhythmia that is usually treated with this procedure is Ventricular Tachycardia (VT) associated with Ischemic Cardiomyopathy (IC).

After a myocardial infarction, myocardial cells die because of the lack of oxygen supply, creating fibrotic areas where electrical impulses are not propagated. Around and through these areas of dense fibrosis, other areas with low-density fibrosis where the impulse is propagated with a low velocity appear. Sometimes, these areas of slow conduction represent corridors with at least two connections with healthy muscle, being the substrate for reentrant VTs. These slow conduction corridors or conducting channels are the target for VT ablation [52, 53].

Different information sources have been used during the last years to identify the conducting channels that are responsible for reentrant VTs. DE-MR imaging is used to find the ablation target prior to the intervention, while EAMS are used intra-operatively. In clinical practice, these two information sources are used separately to characterize cardiac tissue based on different properties. In this chapter of the thesis, a new framework that allows the integration of images from DE-MR, electrical measurements and mechanical properties estimated using an EAMS is presented.

5.2 Background

Recently, many approaches have been developed to characterize scar tissue from different information sources. In this section, a short review of methods for scar characterization from DE-MR images, electrical and mechanical information obtained from an EAMS is presented.

5.2.1 Pre-operative scar characterization

DE-MR imaging has become the standard modality to localize and quantify areas of scar, viable and healthy myocardial tissue pre-operatively [69, 70, 71]. The acquired images visualize the uptake of a contrast agent by the intracellular space after a given time from the administration of the contrast. Healthy myocardium and scar tissue have different uptake profiles and hence, are imaged differently (fibrotic areas appear brighter than healthy myocardium). DE-MR images could be used for ablation planning by identifying pre-operatively the target ablation areas during the procedure [72, 56, 73, 74]. However, the inherent limitations of MR leading to imaging artifacts can lead to errors when identifying scar tissue [72, 75]. In addition, the spatial resolution limits the detection of the border zone channels in the dense scar tissue, since these channels can be very narrow [73, 76].

Different segmentation methods from DE-MR images have been proposed during recent years [77, 78, 79]. Having the segmentation of the myocardium, the scar can be localized based on voxel intensities, since it appears significantly brighter than healthy myocardium. To recover the anatomical structure of the scar automatically, threshold-based methods have been proposed [69, 80]. Other approaches imposing geometrical constraints have been presented to improve the consistency of the results [81, 82]. Cluster-based and support vector machine methods have also been proposed [77, 83, 84].

5.2.2 Intra-operative electrical characterization

Different EAMS have been developed during recent years to guide catheter ablation. One such system is Carto (Biosense Webster, Haifa, Israel). It uses magnetic fields to track the position and orientation of the catheter. When the catheter is properly positioned, it allows the electrical activity at its tip to be recorded; then, based on the tracked position of the catheter tip, the system shows a spatial reconstruction of the mapped cavity, also providing the electrical signals recorded. It is also possible to use an additional software module that allows pre-operative images to be integrated for a better visualization and interpretation of the acquired information.

During the intervention, it is necessary to accurately locate and characterize the scar tissue to find the conducting channels responsible for the VT, which are the ablation target. Mapping during stable rhythm allows the characterization of the arrhythmogenic substrate. After the acquisition, different electrical parameters are used to identify the ablation target, such as the maximum bipolar and unipolar voltages, and the local activation time. Scar core, border zone and healthy tissue can be classified using voltage thresholds. However, there are no standard thresholds that can be used for all patients [54], which makes the cardiologist's expertise a key factor in a successful intervention. In addition, the data obtained from an EAMS have several limitations for a precise characterization of the arrhythmogenic substrate (i.e. far-field effect, time-consuming, poor tissue contact).

5.2.3 Intra-operative mechanical characterization from EAM data

Other types of information, such as myocardial mechanics, can also be considered to better characterize the scar [18] and, therefore, to improve the result of the ablation procedure. It is possible to assess cardiac mechanics during the intervention by using catheter tracking information to estimate cardiac contractility, as presented in Chapter 4 and in [16]. NOGA (Biologics Delivery Systems Group, Cordis Corporation, Irwindale CA, USA) was developed to estimate cardiac mechanics for tissue viability assessment. A technique to integrate electrical and motion information was described in [17] as part of this system and different clinical applications were proposed in [18]. In Chapter 4, a methodology to estimate 3D endocardial motion and deformation fields from electro-anatomical data and a pre-operative image was proposed.

The limitations of the aforementioned methods are related to the accuracy of the catheter tracking system and the presence of components in the recorded motion signals that are not directly related to cardiac motion (i.e., motion related to respiration commented in Chapter 4).

5.2.4 Integration of multi-modal information

Even though scar tissue can be characterized from different information sources, all of them have some limitations. In addition, the results obtained from different sources are based on different tissue properties, so the shape and extent of the scar identified using each modality is not necessarily the same [54, 55, 56].

The information from the different sources could be considered together for a better characterization of myocardial tissue. In [56, 76], a correlation between the conducting channels inside the scar detected by DE-MR and EAMS was found. In [15], it was shown that integrating electrical and mechanical information provided better results than using each type of information separately. In this chapter, a framework is presented where these three information sources (i.e., tissue viability from DE-MR, electrical and motion information from EAM data) are integrated for multi-modal left-ventricular myocardial tissue characterization.

5.3 Methods and procedures

The presented framework has a modular design, integrating three different modules to support the process of scar characterization: cardiac segmentation, image-based characterization and electrical/mechanical characterization from the data recorded with an EAMS. These modules were integrated in GIMIAS (www.gimias.org) [85], which is a workflow-oriented open-source environment that can be extended through the development of problem-specific plug-ins. The implementation was done in the C++ language.

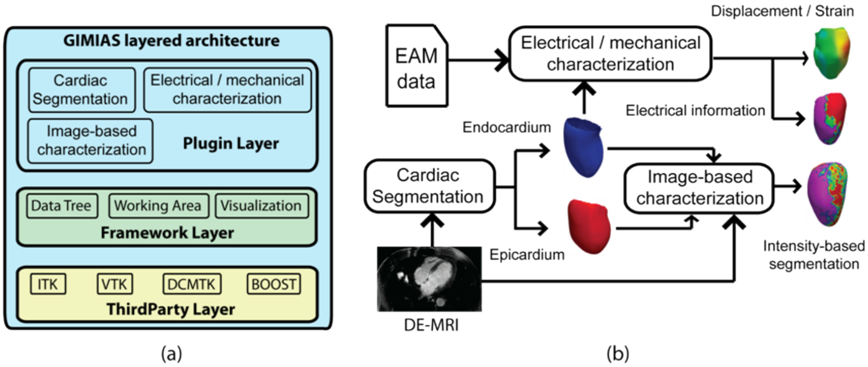

Figure 5.1: (a) Layered architecture of GIMIAS. The Plugin layer is on the top and plugins can interoperate through the elements at the framework layer. The Third Party layer is at the bottom, to which all modules have access. (b) Presented pipeline. Both endocardium and epicardium meshes are segmented from DE-MR images using the cardiac segmentation module. The output meshes are used by the image-based characterization module to characterize the scar based on voxel intensities. The segmented endocardium is also used, together with electro-anatomical mapping data, for electrical and mechanical characterization of the left ventricle. Color image in the Appendix, page xxix.

The layered architecture of GIMIAS is represented in Figure 5.1 (a). Each of the modules for scar characterization is located at the Plugin Layer and can be used independently of the others. Meshes, images, signals or any type of information are attached to the main data tree and are directly accessible by any other module. Figure 5.1 (b) shows a schematic describing how the presented modules inter-operate. In the following sections, each of the modules for scar characterization will be presented.

5.3.1 Cardiac segmentation

The cardiac segmentation module provides algorithms for a semi-automatic segmentation of 3D+t images of the heart from different modalities. The underlying methodology is the same for all modalities, which brings a great advantage when integrating multiple sources of image data.

The method uses a deformable model that encodes statistical information about the shape of the heart based on a Point Distribution Model (PDM). The PDM was built from 134 patients in 15 cardiac phases, totaling 2010 training volumes [86, 87]. The segmentation algorithm has been trained and evaluated on CT [86], SPECT [88], 3D US [63] and MR [89] datasets.

To segment the left ventricle, the user sets three landmarks in the images: one at the center of the aortic valve, one at the center of the mitral valve and another one at the apex. The software positions and scales the average shape in the PDM based on these three landmarks. This PDM contains both the endocardium and the epicardium, and acts as a template that is adapted to the geometry of each patient's heart [61]. Manual corrections can be performed to fix possible errors in the results from the automatic processing. These corrections can be applied either freely or by imposing statistical constraints.

5.3.2 Image-based characterization

The second module in the pipeline was designed for scar characterization from DE-MR images. It needs the model of the left ventricle to be segmented using the cardiac segmentation module as an input. This module divides the segmented ventricle into a number of layers that can be selected by the user from the endocardium to the epicardium, obtaining a 3D shell for each of the layers. One signal intensity map at each layer is obtained by summing the intensity of all the voxels between neighboring layers, as explained in [73]. This information is then projected onto each shell.

Scar areas can be differentiated from healthy myocardium based on the distribution of the intensities in the image, since scar tissue appears brighter in DE-MR images. Moreover, scar core and border zone can also be identified using thresholds, as previously reported in [56]. Based on this study, areas with signal intensities higher than 60% of the maximum are classified as scar core, while areas with signal intensities lower than 40% of the maximum are classified as healthy tissue. The remainder of the tissue is considered as border zone. However, since image artifacts may affect the intensity range in the image, these thresholds may need to be adjusted manually. Finally, this threshold-based classification can be visualized in 3D through color-coded maps in every transmural shell. Figure 5.2 shows one example of segmentation of a left ventricle with scar tissue characterized based on image intensity levels using the presented framework.

5.3.3 Electrical / Mechanical characterization

The third module in the pipeline allows both electrical and mechanical characterization of the tissue using EAM data and a left ventricle model segmented using the cardiac segmentation module. In particular, EAMs imported from the Carto system are used.

This module allows electro-anatomical data to be loaded and used intraoperatively in a catheter-guided intervention. It is possible to visualize all the electrical signals recorded, together with the catheter tracking information. The maximum bipolar voltage, maximum unipolar voltage and local activation time at each point are calculated for electrical characterization

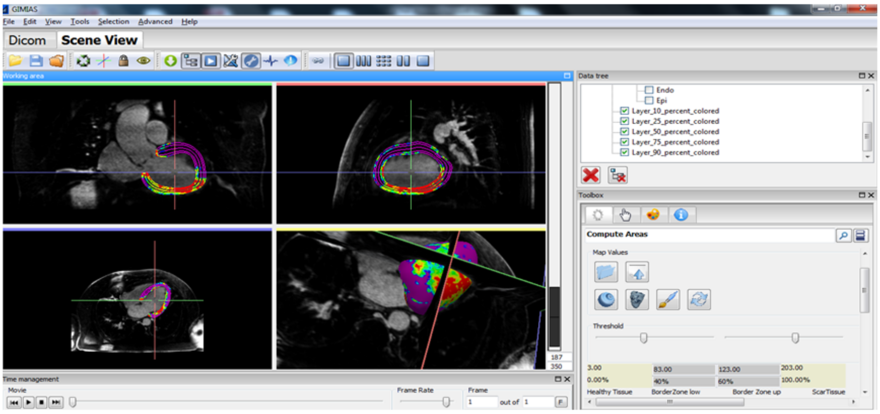

☐ Endo
☐ Epi
☑ Layer_10_percent_colored
☑ Layer_25_percent_colored
☑ Layer_50_percent_colored
☑ Layer_75_percent_colored
☑ Layer_90_percent_colored

Healthy Tissue	BorderZone low	Border Zone up	ScarTissue
3.00	83.00	123.00	203.00
0.00%	40%	60%	100.00%

Figure 5.2: Layers extracted from the left ventricle model segmented with the cardiac segmentation module. Tissue classification based on image intensities is color coded. Red represents dense scar tissue, green represents viable tissue (border zone) and purple represents healthy myocardium. Color image in the Appendix, page xxx.

of the tissue. The trajectory of the catheter (which is in contact with the endocardium) during the acquisition of the local electrograms can also be visualized (see Figure 5.3).

The cloud of points acquired during the intervention can be registered to the endocardial surface extracted from the cardiac segmentation module. This is done by selecting at least three landmarks in both the surface and the cloud of points. Then, an Iterative Closest Point (ICP) algorithm [62] can be used to improve the registration results. If ventricle segmentation is used intra-operatively to guide the intervention, it is also possible to load the transformation matrix calculated intra-operatively, getting the same registration used during the intervention. After registration, all the electrical parameters on the endocardial surface can be projected and interpolated. They can also be projected into any of the different layers with scar information obtained from DE-MR images, allowing the visualization of the information from both sources on the same surface.

Once the ventricle shape and the points from the EAMS are registered, it is also possible to estimate endocardial motion and deformation using the method presented in Chapter 4. This method extracts the catheter trajectories during one cardiac cycle and synchronizes the motion signals of all the points acquired. Then, catheter trajectories are projected into the endocardial mesh using a bilinear atlas to help interpolate motion in the areas where this information is not available. The result is a 3D+t endocardial mesh where both displacement field and directional strains are also calculated, providing mechanical information at each time point.

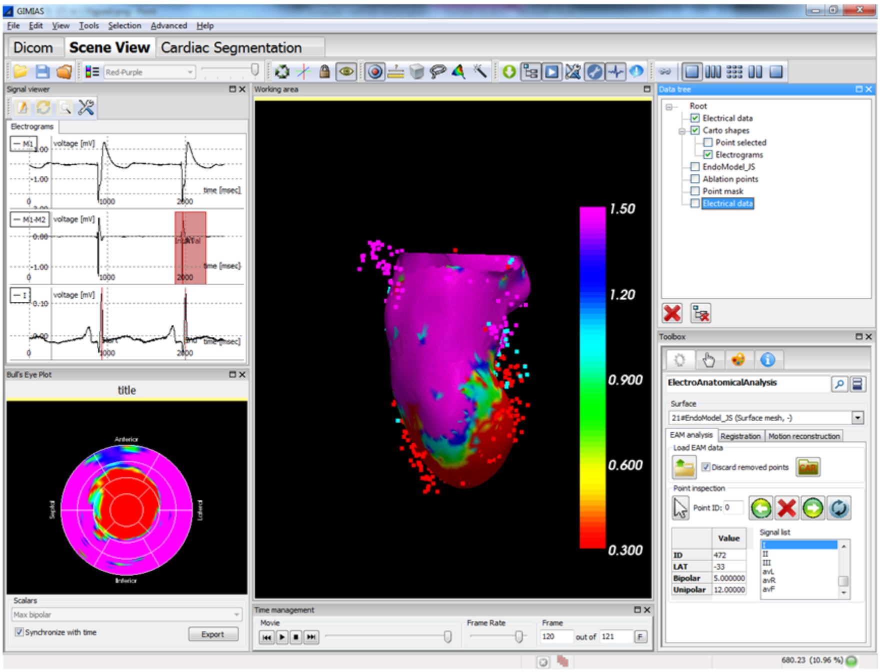

Figure 5.3: Electrical characterization of the tissue. EAM points are registered to the left ventricle endocardium. Electrical parameters derived from the recorded electrograms are interpolated on the mesh. The image shows the maximum bipolar voltage color coded. Purple color represents healthy tissue (> 1.5 mV) and red color represents dense scar (< 0.5 mV). The information is also represented using the 17-segments model proposed by the American Heart Association. Bipolar, unipolar electrograms and superficial ECG (lead I) are also shown in the upper left corner for one selected point. Color image in the Appendix, page xxxi.

Finally, all the information can be visualized into the 17-segments model proposed by the American Heart Association (AHA) [49]. Curves showing the evolution of displacement and strain can also be obtained and exported. As an illustration, Figure 5.3 shows a cloud of EAM points registered to a left ventricle segmentation, together with the electrical scar characterization.

5.3.4 DE-MR image acquisition protocol

All patients included in the study underwent a DE-MR exam prior to the ablation procedure (median 2 days, interquartile range 1 - 6 days). A 3-Tesla scanner (Magnetom Trio, Siemens Medical Solutions, Erlangen, Germany) equipped with advanced cardiac-dedicated software and a cardiac 12-element phased array coil was used. Patients were instructed to maintain shallow breathing during the acquisition. Seven minutes after intravenous administration of gadodiamide-DTPA (Omniscan®, Amersham Health) at a dose of 0.2 mmol/kg, a whole-heart, high spatial resolution, DE-MR study was conducted using a free-breathing, navigator-gated, 3D inversion-recovery, gradient echo technique [90]. The 3D slab was acquired in the transaxial direction. Slice thickness was 1.4 mm, with no gap between slices. The field of view (FOV) was set to 360 mm and matrix size was kept at 256 x 256 pixels to yield an isotropic spatial resolution of 1.4 x 1.4 x 1.4 mm. Image acquisition was ECG-gated to end-diastole to minimize cardiac motion. A standard delayed-enhanced dataset was obtained by applying a 2D IR-TurboFLASH sequence in sequential 5 mm slices with no gap between them, to cover both ventricles in the short-axis orientation in addition to the 2-, 3-, and 4-chamber views.

5.3.5 Electrophysiology and substrate mapping

The electrophysiology study was performed under conscious sedation. A tetrapolar diagnostic catheter was positioned at the right ventricular apex. Trans-septal or retro-aortic approaches were used for left ventricular access. An endocardial high-density 3D electro-anatomical bipolar voltage map of the left ventricle was obtained during stable sinus rhythm using the Carto system. Standard voltage thresholds ($< 0.5mV$ for the core and $< 1.5mV$ for the border zone) were used to define the scar on the EAM. The conducting channels on the EAM were visually identified as: (i) corridors of border zone (maximum bipolar voltage between 0.5 and 1.5 mV) within scar core areas or between a scar core area and the mitral annulus [91], or (ii) late potential channels. The latter were defined as regions with 2 or more consecutive endocardial electrograms presenting delayed components, localized in the scar area and connecting with healthy tissue, which are not possible to visualize using voltage thresholds [92].

5.4 Results

Results from three patients are presented to illustrate the framework's utility for catheter ablation planning and treatment. For these three cases, the left ventricle was segmented from DE-MR prior to the catheter ablation intervention using the cardiac segmentation module. Then, the module for image-based scar characterization was used to classify the scar core, border zone and healthy myocardium.

The meshes obtained pre-operatively were used during the intervention to guide the procedure. The EAMs obtained were then imported into the module for electrical and mechanical characterization from EAM data. Finally, electrical values were projected into the endocardial mesh and ventricular motion was reconstructed.

For each patient, a figure including different measurements obtained by integrating data using the presented framework is shown: segmentation of the left ventricle and scar characterization from DE-MR images, maximum unipolar voltage, maximum bipolar voltage, local activation time recorded with Carto and projected onto the ventricle shape, and longitudinal strain estimated at end systole as presented in Chapter 4. In addition, a comparison between the extension of the scar identified pre-operatively from DE-MR images and intra-operatively using the bipolar maps was also performed.

5.4.1 Results for Case 1

The first patient analyzed for this study was a 75 year old man with VT associated with IC. Figure 5.4 shows the results for this patient. In this case, a scar was identified pre-operatively from DE-MR images in the inferior wall of the left ventricle. Three areas were identified as conducting channels and, hence, possible ablation targets. After the electrophysiology study, the maximum bipolar voltage showed a very homogeneous scar in comparison with the scar shape obtained from DE-MR images. The scar area defined using the bipolar voltage map was 39% larger compared to the scar identified from DE-MR images, while the border zone area was 11% smaller.

The maximum unipolar voltage map showed a shape and extension of the scar very similar to the one from the maximum bipolar map. The local activation time showed a conduction delay in the areas around the dense scar, where electrical impulse was still propagated. As expected, spatially heterogeneous strain patterns were obtained. In particular, the longitudinal strain showed no contraction or stretching in the dense scar area while it reflected contraction in the surrounding areas.

Ablation was performed at the entrance of each one of the conducting channels identified pre-operatively from DE-MR images, resulting in a non-inducible arrhythmia and hence, a successful intervention.

5.4.2 Results for Case 2

The results for another patient (male, aged 69, VT with IC) are shown in Figure 5.5. The DE-MR study showed an infero-septal scar with a wide longitudinal line of border zone tissue. The bipolar map showed low voltages for the whole scar. The extension of the scar identified with the bipolar map was 23% larger than the one identified from DE-MR images. In this case, the bipolar map showed low voltage values for the whole base of the ventricle, while the scar defined from DE-MR images was only localized in

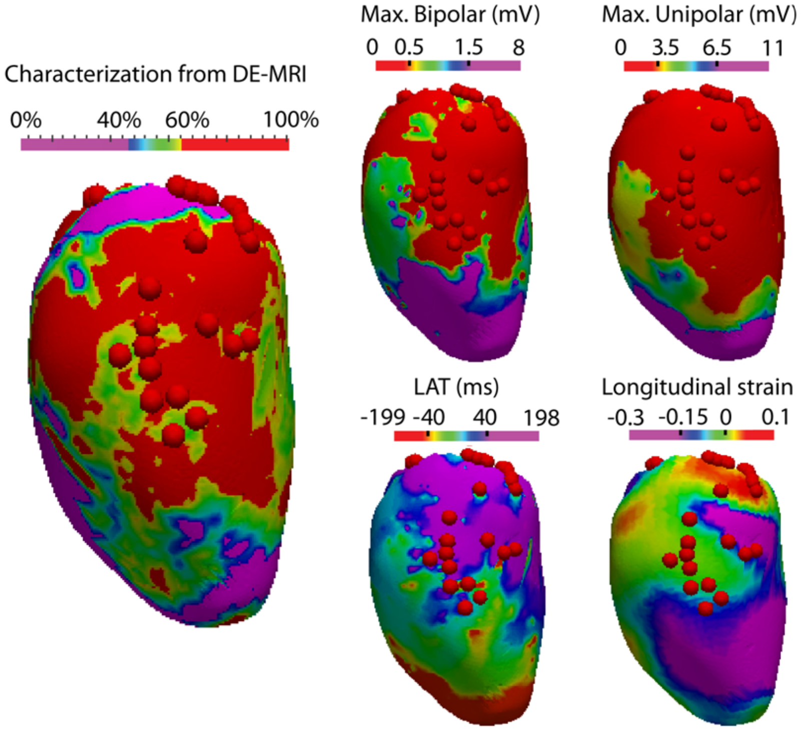

Figure 5.4: Information integrated by the framework for a 75-year-old man with VT associated with IC. In the scar characterization from DE-MR images, red color represents scar core, purple represents healthy tissue and the rest of the colors represent border zones according to the signal intensity maps. The electrical information is represented by the bipolar voltage map, the unipolar voltage map and the local activation time map. Longitudinal strain calculated at end systole is shown, where negative values represent contraction and positive values indicate stretching. End-systolic strain values are represented on the endocardium at end-diastolic phase to improve visual comparison with the other results. Red spheres represent the ablation targets identified pre-operatively from DE-MR images. Color image in the Appendix, page xxxii.

the inferior wall. The border zone area from the bipolar map was 65% larger compared to results from DE-MR, finding reduced voltage values in a large area of the ventricle.

The unipolar map showed low voltages for the whole scar, being higher at the entrance of the line of border zone tissue identified from DE-MR images. The local activation time presented some heterogeneities at the entrance of this border zone line, as in the case of the unipolar voltage map. The longitudinal strain showed reduced contraction in the inferior wall, with higher contraction at the entrance of the border zone channel identified from DE-MR images. It is also possible to observe the presence of stretching areas in the dense scar area.

The points of ablation were situated at the entrance of the corridor of border zone that was identified from both DE-MR images and the electrical maps.

5.4.3 Results for Case 3

Figure 5.6 shows the results for the third patient (male, aged 82, VT with IC). The DE-MR study allowed the identification of a scar in the anterior wall. The bipolar map showed a dense scar area 57% larger than the area identified from DE-MR images. On the other hand, the area of border zone tissue was 33% smaller compared to the results from DE-MR images.

The unipolar map showed very homogeneous low voltage values for the whole scar. On the other hand, the local activation time showed very heterogeneous patterns. The longitudinal strain was reduced in the whole wall, showing some stretching in the apex.

In this case, ablation was performed at the border zone channels identified from DE-MR images and the local activation time map, as seen from Figure 5.6.

5.5 Discussion

Three study cases were presented, showing multimodal myocardial tissue characterization based on different information sources. Results demonstrated the clinical feasibility of the approach and showed that there is a relation between the shape and extension of the scar identified from the different sources. However, as expected [55], there are also variations between the results from the different modalities. In the three cases presented, the extension of the dense scar area identified using electrical maps was larger than the dense scar area identified from DE-MR images (range 23% - 57%). It was possible to identify most of the conducting channels from DE-MR images prior to the intervention, although the electrical maps were necessary to

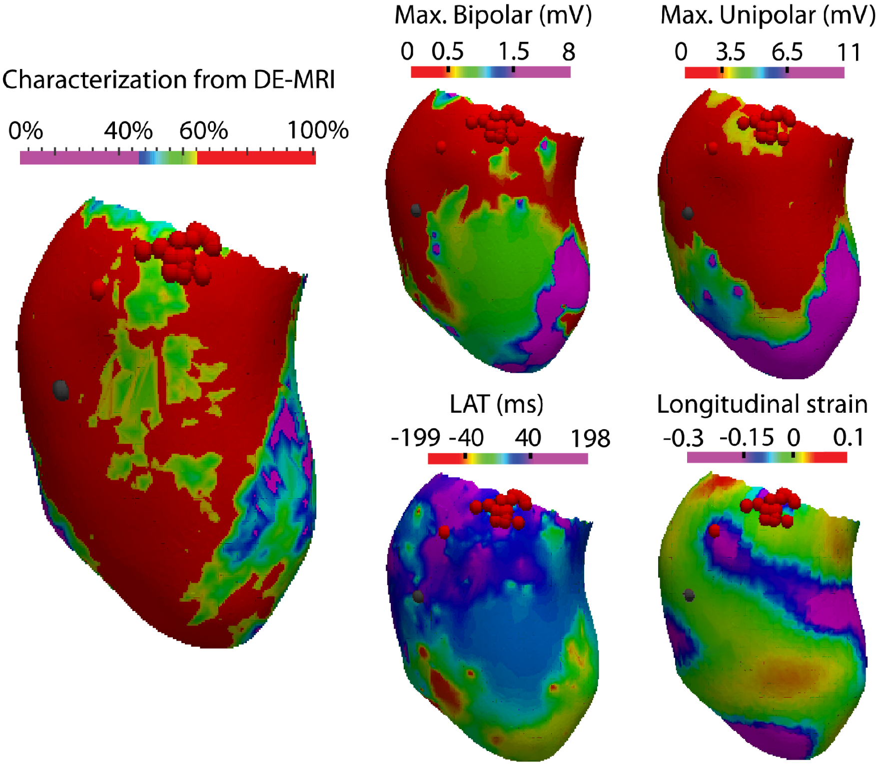

Figure 5.5: Information integrated by the framework for a 69-year-old man with VT associated to IC. In the scar characterization from DE-MR images, red color represents scar core, purple represents healthy tissue and the rest of the colors represent border zone according to the signal intensity maps. The electrical information is represented by the bipolar voltage map, the unipolar voltage map and the local activation time map. Longitudinal strain calculated at end systole is shown, where negative values represent contraction and positive values indicate stretching. End-systolic strain values are represented on the endocardium at end-diastolic phase to improve visual comparison with the other results. Red spheres represent the ablation targets identified pre-operatively from DE-MR images, while gray spheres represent the ones identified intra-operatively using the electrical maps. Color image in the Appendix, page xxxiii.

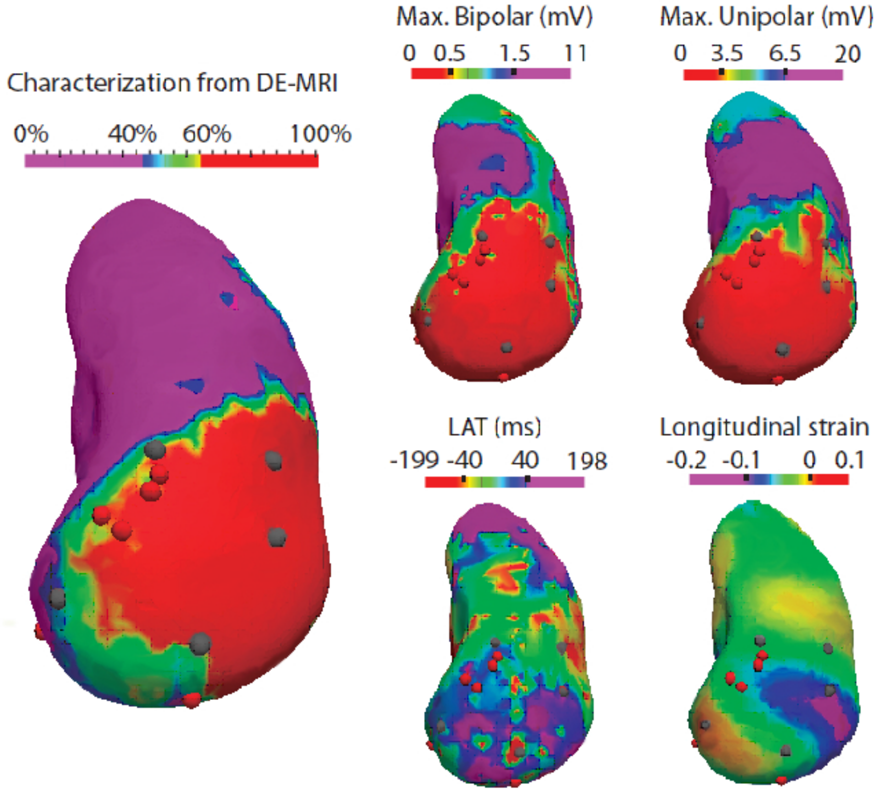

Figure 5.6: Information integrated by the framework for a 82-year-old man with VT associated to IC. In the scar characterization from DE-MR images, red color represents scar core, purple represents healthy tissue and the rest of the colors represent border zone according to the signal intensity maps. The electrical information is represented by the bipolar voltage map, the unipolar voltage map and the local activation time map. Longitudinal strain calculated at end systole is shown, where negative values represent contraction and positive values indicate stretching. End-systolic strain values are represented on the endocardium at end-diastolic phase to improve visual comparison with the other results. Red spheres represent the ablation targets identified pre-operatively from DE-MR images, while gray spheres represent the ones identified intra-operatively using the electrical maps. Color image in the Appendix, page xxxiv.

find all of them, as it can be observed from Figures 5.4-5.6.

Maximum bipolar and unipolar voltage maps showed a similar shape and extension of the scar. In the case of the second patient, the unipolar voltage map showed areas with low voltage values that were not identified by the bipolar voltage map. These differences could be explained because endocardial bipolar maps give information about subendocardial activation, while endocardial unipolar voltage maps give transmural information [93].

The local activation time map was able to detect the conducting channels for the three patients presented, showing delayed activation in comparison to the healthy myocardium. Unipolar and bipolar maps were not able to distinguish all conducting channels, showing a homogeneous scar core. Activation maps during sinus rhythm have been recently proposed to better define the areas of interest during substrate mapping as areas with ventricular activation after the QRS [92, 94].

The resulting longitudinal strain presented heterogeneous spatial patterns. For the cases analyzed, stretching areas at end systole were found in the scar core, with contraction around these areas. Heterogeneities in the scar areas could be explained by the tethering to adjacent tissue [57], being the contraction or stretching due to passive motion. Moreover, the presence of scar tissue affects the motion of the whole ventricle and thereby its deformation.

The example cases presented showed that the proposed framework is feasible and potentially useful for the analysis and integration of multimodal information for scar characterization. It could be used intraoperatively for guidance and monitoring of therapy by integrating it with any EAMS.

The results obtained show the feasibility of the technique in a clinical setting. They do not constitute, however, a detailed quantitative validation on the clinical impact of this technique (e.g., in terms of reduction of interventional time or X-ray radiation dose). A prospective study of clinical impact that includes a randomized population of subjects suffering from VT and undergoing radiofrequency ablation using this technique and the standard-of-practice is the natural next step. This work does, however, offer, as a first step, the preliminary proof-of-concept evidence for such a study.

Furthermore, the presented framework allows annotating both the electrical signals and the visualized meshes. In addition, all the information used can be exported for subsequent analysis or for research purposes.

A limitation of this framework is that motion and deformation were only estimated for the endocardium of the left ventricle. The reason is that the used spatiotemporal atlas only included shape and motion information about the endocardium of the left ventricle. However, the framework allows incorporating information about other cavities. Moreover, this framework could be extended in multiple ways (including algorithms for predictive analysis, automatic detection of conducting channels...).

5.6 Conclusion

A framework for the integrated analysis of DE-MR images, electrical and mechanical information has been presented. Integrating multi-modal information can be helpful for interventional guidance and monitoring of radiofrequency ablation procedures where myocardial scar tissue characterization is required. The three presented example cases show that the relevance of the information extracted from the different sources can vary depending on the patient analyzed (i.e., conducting channels that are visible in DE-MR images but not in the bipolar and unipolar maps and vice versa). The framework can also be helpful for research purposes, facilitating the study of the relation between electrical and mechanical properties of the tissue, as well as the information obtained from DE-MR images.

CHAPTER 6

Conclusions and outlook

6.1 Conclusions

The objective of this thesis was to develop methods for the integration of different types of images and information to characterize cardiac tissue. In particular:

- In Chapter 2, a method to estimate cardiac motion by integrating B-mode echocadiography and TD images has been proposed.
- In Chapter 3, an extension of the previous method to estimate cardiac motion from multi-plane images has been presented.
- In Chapter 4, a method to estimate cardiac motion intra-operatively using information from an EAMS and a pre-operative image has been proposed.
- In Chapter 5, a framework integrating tissue viability information from DE-MR images together with the electrical and motion information estimated using EAM data has been presented.

All the presented methods integrate different information sources to improve cardiac tissue characterization with respect to using a single source. Methods to estimate cardiac motion from image data were proposed in Chapter 2 and Chapter 3, while the methods presented in Chapter 4 and Chapter 5 were oriented to interventional planning and guidance, integrating data that are normally used in electrophysiology procedures.

6.2 Overview

In this section, the advances presented in this thesis are summarized, together with their limitations and future directions of research.

6.2.1 Improved motion estimation from US images

As reported in Chapter 2, many approaches to quantify cardiac motion from US image sequences have been developed during the last few years. However, widely used grayscale B-mode US images present some problems (i.e., artifacts, reverberations, limited spatiotemporal resolution) that may compromise the results obtained from tracking. Although TD images allow an objective quantification of tissue velocities, they are also affected by the intrinsic problems of US imaging and they only provide the velocity component in the beam direction.

Since both TD and B-mode echocardiography are tipically acquired in clinical practice for cardiac motion assessment, a method to use them together for an impoved cardiac motion estimation has been proposed. Its advantages are twofold:

1. Two different information sources are used, thus reducing the impact of the errors that may be present in each of them.
2. The use of a transformation model that is continuous both in space and time allows using information sources with different spatial and temporal resolutions without the need of compensating for this difference. Hence, it is not necessary to interpolate or discard information, unlike other methods in the literature [14, 32].

The improvements obtained with the proposed method can be particularly useful in cases where the temporal resolution is important (e.g., stress echocardiography, cardiac resynchronization therapy...), since TD images are normally acquired at higher frame rates than B-mode images. In this thesis, these improvements have been validated using synthetic data and illustrated using stress echocardiography from real volunteers, which is interesing to understand the relation between cardiac function and functional capacity during exercise.

Although cardiac motion estimation integrating B-mode and TD images showed to be more accurate than using a single modality, its results are still determined by the quality of the images acquired. In particular, improvements are mostly concentrated in the beam direction, so tracking in the azimuth direction is still compromised by B-mode image quality.

6.2.2 Cardiac motion estimation from multi-plane US images

In Chapter 3, the method presented in Chapter 2 was extended to estimate cardiac motion in the whole ventricle using multi-plane images. These images are acquired interleaved at the same time, so all the information is acquired from the same heart beat. This is an advantage with respect to using 3D volumetric US images, which are reconstructed using information acquired from different cardiac cycles. In addition, multi-plane US images also allow using quantitative information from TD measurements.

The transformation model was modified so that the low temporal resolution of the B-mode sequences did not limit the accuracy of the motion field estimated on the beam direction, where the TD images provide an increased temporal resolution. This modification is more important when using multi-plane images than when using 2D US images. In typically acquired 2D US images, the temporal resolution of the TD image sequence is normally 3 times higher than the resolution of the B-mode sequences (see Tables 2.2 and 2.3). However, in multi-plane images, this relation is incresed up to 7 times (see Tables 3.2 and 3.3).

The method was validated using a synthetic dataset and its utility to assess ischemic patients was also illustrated. This is particularly interesting because this kind of patients often present variable heart rythms and, therefore, a high-quality 3D US image cannot be reconstructed with clinically available US acquisition systems. Although results showed that the method allows estimating displacement and strain in the longitudinal and radial directions, the circumferential component cannot be estimated, since it corresponds to out-of-plane motion.

6.2.3 Cardiac motion estimation from EAM data

Intra-operative cardiac motion assessment can be useful for guidance purposes. To this end, a method to estimate cardiac motion using catheter position information recorded during an electrophysiology intervention, together with a pre-operative image, was proposed in Chapter 4. Because of the spatially sparse and noisy position information that is available, a cardiac atlas was used to help the motion estimation process.

The results obtained from the experiments with synthetic data showed that the proposed method can estimate cardiac motion and strain accurately. The experiments performed with the real cases showed the added value of using this method intra-operatively for scar characterization. One advantage of this approach is that it may help electrophysiologists in decision making by improving tissue characterization without using additional instruments or information during the intervention. Furthermore, the method would allow studying changes in heart motion produced intra-operatively.

A limitation of the method is that the radial strain cannot be estimated, since only endocardial motion was provided by the EAM data. Furthermore, it is important to remark that the results highly depend on the quality of the acquired data. In particular, if points are acquired when the catheter is not well positioned or if it slides on the endocardial wall, local motion estimation would be affected and may not be reliable.

6.2.4 Integration of electrical, motion and DE-MR image information

In many electrophysiology inteventions, DE-MR image information is used for interventional planning, while intra-operative electro-anatomical data are used to assess cardiac electrical activation and make decisions during the intervention. In Chapter 4, it was shown the the electrical information can be complemented with endocardial motion information estimated intra-operatively with an EAMS without using any additional device. Since DE-MR images can also be used intra-operatively for guidance purposes, a framework integrating tissue viability information from DE-MR, together with electrical and motion information obtained intra-operatively using an EAMS was proposed in Chapter 5.

The presented framework provides tissue characterization using information of different nature that may be very useful during an electrophysiology intervention. It also provides a powerful tool to study how the information obtained from the different sources are related.

The benefits of using this framework are constrained by the limitations of each of the methods used to characterize cardiac tissue from the different sources (e.g., poor DE-MR image quality leading to segmentation errors, acquisition errors both in catheter position and electrical signals...). In addition, possible registration errors between pre-operative and intra-operative information need to be taken into account.

6.2.5 Outlook and future research avenues

In Chapters 2 and 3, different US image modes (i.e., B-mode and TD) and different views (i.e., multi-plane US) have been integrated for an improved cardiac motion estimation. Novel advances in US image aquisition techniques will provide information of higher quality, which would be translated to more accurate results using the methods proposed in this thesis.

One of the main challenges in cardiac ultrasound imaging is to increase the temporal resolution of the acquired images. In the proposed approach to integrate B-mode and TD images for cardiac motion estimation, the temporal resolution was improved in the beam direction (where TD images provide information). However, it was still constrained by the relatively low resolution of the B-mode sequence in the azimuth direction. Multi-line transmit beam forming has proven to provide high quality B-mode images at high frame rates (about 450 Hz) [95, 96]. The implementation of multi-line transmit beam forming in comercial ultrasound aquisition systems in the near future will improve significantly the temporal resolution of the acquired B-mode images. Using sequences with higher number of frames would translate to results with improved temporal resolution, without modifying the implementation of the methods proposed in this thesis.

The number of frames that is tipically recorded in wide angle acquisitions using commercial systems is not adequate to estimate strain rate reliably [5]. In cases where a high temporal resolution is important (e.g., stress echocardiography, cardiac resynchronization therapy...), increased number of frames is achieved by reducing the size of the field of view and making different recordings to cover the whole left ventricle. In [97], a preliminary study showing the feasibility of using multi-line transmit beamforming for TD image acquisition was presented. In that study, they used this technique to obtain a wide field of view without reducing the temporal resolution of the recorded images. This would allow using the proposed methods to exploit the increased number of frames and estimate the strain rate.

The method proposed to integrate B-mode and TD images could also be used to integrate other image modalities that are acquired simultaneously. In paticular, it would be possible use it with phase-contrast MR images [98], which are acquired together with magnitude images (such as the ones acquired with conventional cine-MR). In this case, it would be necessary to modify the dissimilarity terms in Eq. 2.4 (page 19) to adapt better to the properties of the MR image sequences.

Beyond the motion information obtained from US images, other types of information acquired non-invasively could also be considered for a more complete characterization of the heart. Images obtained from MR or CT would provide high-resolution anatomical information compared to the one that can be extracted from US images. Moreover, improvements in inverse ECG [99], which consists in estimating the cardiac activity non-invasively from recorded body surface potentials, would also make possible to add information about heart's electrical activation. This information, together with the motion estimation that can also be obtained non-invasively (as with the methods proposed in Chapter 2 and Chapter 3), would provide an improved cardiac characterization with respect to using only image information. In addition, it would allow analyzing the relation between electrical and mechanical events in the heart.

Furthermore, information of different nature, such as electrophysiology data, catheter position data and DE-MR images, have been integrated in this thesis to improve cardiac tissue characterization intra-operatively. By integrating different types of information, a more complete characterization of the heart was obtained, which may be helpful for decision making during the intervention.

The spatiotemporal atlas used to estimate cardiac motion in Chapters 4 and 5 only included information about the left ventricle. This could be extended to consider the right ventricle and the atria, which would allow using this framework to plan and guide other catheter interventions, such as cardiac ablation to treat atrial fibrillation. Methods to estimate the quality of the acquired position signals could also be considered to provide information about the confidence in the motion reconstructed.

Novel advances in the acquisition of electro-anatomical maps, such as fast anatomical mapping using multi-electrode catheters (i.e., Pentaray NAV catheter, Biosense Webster, Haifa, Israel), reduce considerably the time of the intervention. In addition, the improved stability and the synchronous acquisition of multiple points would improve the quality of the infomation acquired and, therefore, the performance of the proposed methods. Other advances reducing the errors in electrical and position measurements from an EAMS, or increasing DE-MR image quality, would also improve the accuracy in the results.

In addition, the possibility of using intra-cardiac US images with modern EAMS improves shape modeling and registration with the points acquired during the intervention [100, 101]. Methods to estimate cardiac motion from these US acquisitions and to integrate this estimation with the electro-anatomical data may be explored in the future. Other advances reducing the size of the acquisition devices (i.e., portable US systems) would also facilitate their use in an environment with limited space, as in an intra-operative environment. Real-time motion information provided by an external US acquisition system would be very useful to analyze the changes produced during the procedure and would allow analyzing accurately the electro-mechanical coupling.

References

[1] B. H. Bijnens, M. Cikes, C. Butakoff, M. Sitges, and F. Crispi, “Myocardial motion and deformation: What does it tell us and how does it relate to function?,” *Fetal Diagn Ther*, vol. 32, no. 1-2, pp. 5–16, 2012.

[2] L. E. Teichholz, T. Kreulen, M. V. Herman, and R. Gorlin, “Problems in echocardiographic volume determinations: echocardiographic-angiographic correlations in the presence of absence of asynergy.,” *Am J Cardiol*, vol. 37, no. 1, pp. 7–11, 1976.

[3] N. B. Schiller, P. M. Shah, M. Crawford, A. DeMaria, R. Devereux, H. Feigenbaum, H. Gutgesell, N. Reichek, D. Sahn, and I. Schnittger, “Recommendations for quantitation of the left ventricle by two-dimensional echocardiography. american society of echocardiography committee on standards, subcommittee on quantitation of two-dimensional echocardiograms.,” *J Am Soc Echocardiogr*, vol. 2, no. 5, pp. 358–367, 1989.

[4] J. L. Gutiérrez-Chico, J. L. Zamorano, L. Pérez de Isla, M. Orejas, C. Almería, J. L. Rodrigo, J. Ferreirós, V. Serra, and C. Macaya, “Comparison of left ventricular volumes and ejection fractions measured by three-dimensional echocardiography versus by two-dimensional echocardiography and cardiac magnetic resonance in patients with various cardiomyopathies.,” *Am J Cardiol*, vol. 95, no. 6, pp. 809–813, 2005.

[5] G. Sutherland, L. Hatle, P. Claus, J. D’hooge, and B. H. Bijnens, *Doppler myocardial imaging-a textbook*. BSWK Bvba, 2006.

[6] C. M. Otto, *Practice of Clinical Echocardiography*. Elsevier Health Sciences, 2012.

[7] E. Agricola, M. Oppizzi, M. Pisani, F. Maisano, and A. Margonato, “Accuracy of real-time 3D echocardiography in the evaluation of functional anatomy of mitral regurgitation,” *Int J Cardiol*, vol. 127, no. 3, pp. 342–349, 2008.

[8] C. Szmigielski, K. Rajpoot, V. Grau, S. G. Myerson, C. Holloway, J. A. Noble, R. Kerber, and H. Becher, “Real-time 3D fusion echocardiography.,” *JACC Cardiovasc Imag*, vol. 3, no. 7, pp. 682–690, 2010.

[9] K. Rajpoot, V. Grau, J. A. Noble, H. Becher, and C. Szmigielski, “The evaluation of single-view and multi-view fusion 3D echocardiography using image-driven segmentation and tracking.,” *Med Image Anal*, vol. 15, no. 4, pp. 514–528, 2011.

[10] E. Oubel, M. De Craene, M. Gazzola, A. Hero, and A. Frangi, “Multiview registration of cardiac tagging MRI images,” in *IEEE ISBI*, pp. 388–391, 2007.

[11] V. Grau, C. Szmigielski, H. Becher, and J. Noble, “Combining apical and parasternal views to improve motion estimation in real-time 3D echocardiographic sequences,” in *IEEE ISBI*, pp. 516–519, 2008.

[12] G. Piella, M. De Craene, C. Butakoff, V. Grau, C. Yao, S. Nedjati-Gilani, G. P. Penney, and A. F. Frangi, “Multiview diffeomorphic registration: application to motion

and strain estimation from 3D echocardiography.," *Med Image Anal*, vol. 17, no. 3, pp. 348–364, 2013.

[13] B. H. Amundsen, J. Crosby, P. A. Steen, H. Torp, S. A. Sloerdahl, and A. Stoeylen, "Regional myocardial long-axis strain and strain rate measured by different tissue doppler and speckle tracking echocardiography methods: a comparison with tagged magnetic resonance imaging," *Eur J Echocardiogr*, vol. 10, no. 2, pp. 229–237, 2009.

[14] M. Suhling, M. Arigovindan, C. Jansen, P. Hunziker, and M. Unser, "Bimodal myocardial motion analysis from B-mode and tissue Doppler ultrasound," in *IEEE ISBI*, vol. 1, pp. 308–311, 2004.

[15] R. Kornowski, M. K. Hong, L. Gepstein, S. Goldstein, S. Ellahham, S. A. Ben-Haim, and M. B. Leon, "Preliminary animal and clinical experiences using an electromechanical endocardial mapping procedure to distinguish infarcted from healthy myocardium," *Circulation*, vol. 98, no. 11, pp. 1116–1124, 1998.

[16] J. Lessick, G. Hayam, A. Zaretsky, S. A. Reisner, Y. Schwartz, and S. A. Ben-Haim, "Evaluation of inotropic changes in ventricular function by NOGA mapping: comparison with echocardiography," *J Appl Physiol*, vol. 93, no. 2, pp. 418–426, 2002.

[17] H. U. Klemm, R. Ventura, O. Franzen, S. Baldus, K. Mortensen, T. Risius, and S. Willems, "Simultaneous mapping of activation and motion timing in the healthy and chronically ischemic heart," *Heart Rhythm*, vol. 3, no. 7, pp. 781–788, 2006.

[18] P. Psaltis and S. Worthley, "Endoventricular electromechanical mapping-the diagnostic and therapeutic utility of the NOGA®XP cardiac navigation system," *J Cardiovasc Transl*, vol. 2, no. 1, pp. 48–62, 2009.

[19] O. Camara, S. Oeltze, M. Craene, R. Sebastian, E. Silva, D. Tamborero, L. Mont, M. Sitges, B. H. Bijnens, and A. F. Frangi, "Cardiac motion estimation from intracardiac electrical mapping data: Identifying a septal flash in heart failure," in *FIMH*, vol. 5528 of *LNCS*, pp. 21–29, 2009.

[20] C. Petitjean, N. Rougon, and P. Cluzel, "Assessment of myocardial function: a review of quantification methods and results using tagged MRI.," *J Cardiovasc Magn R*, vol. 7, no. 2, pp. 501–516, 2005.

[21] A. P. Sarvazyan, O. V. Rudenko, S. D. Swanson, J. B. Fowlkes, and S. Y. Emelianov, "Shear wave elasticity imaging: a new ultrasonic technology of medical diagnostics.," *Ultrasound Med Biol*, vol. 24, no. 9, pp. 1419–1435, 1998.

[22] G. Montaldo, M. Tanter, J. Bercoff, N. Benech, and M. Fink, "Coherent plane-wave compounding for very high frame rate ultrasonography and transient elastography.," *IEEE T Ultrason Ferr*, vol. 56, no. 3, pp. 489–506, 2009.

[23] R. Jasaityte, B. Heyde, and J. D'hooge, "Current state of three-dimensional myocardial strain estimation using echocardiography.," *J Am Soc Echocardiogr*, vol. 26, no. 1, pp. 15–28, 2013.

[24] M. J. Ledesma-Carbayo, J. Kybic, M. Desco, A. Santos, M. Suhling, P. Hunziker, and M. Unser, "Spatio-temporal nonrigid registration for ultrasound cardiac motion estimation.," *IEEE Trans Med Imag*, vol. 24, no. 9, pp. 1113–1126, 2005.

[25] C. T. Metz, S. Klein, M. Schaap, T. van Walsum, and W. J. Niessen, "Nonrigid registration of dynamic medical imaging data using nd + t B-splines and a groupwise optimization approach.," *Med Image Anal*, vol. 15, no. 2, pp. 238–249, 2011.

[26] M. Yigitsoy, C. Wachinger, and N. Navab, "Temporal groupwise registration for motion modeling," in *Inf Process Med Imaging*, vol. 6801 of *LNCS*, pp. 648–659, 2011.

[27] M. De Craene, G. Piella, O. Camara, N. Duchateau, E. Silva, A. Doltra, J. D'hooge, J. Brugada, M. Sitges, and A. F. Frangi, "Temporal diffeomorphic free-form deformation: Application to motion and strain estimation from 3D echocardiography," *Med Image Anal*, vol. 16, no. 2, pp. 427–450, 2012.

[28] A. Trouvé, "Diffeomorphisms groups and pattern matching in image analysis," *Int J Comput Vis*, vol. 28, pp. 213–221, 1998.

[29] N. Paragios, "A level set approach for shape-driven segmentation and tracking of the left ventricle.," *IEEE Trans Med Imag*, vol. 22, no. 6, pp. 773–776, 2003.

[30] I. Dydenko, F. Jamal, O. Bernard, J. D'hooge, I. E. Magnin, and D. Friboulet, "A level set framework with a shape and motion prior for segmentation and region tracking in echocardiography," *Med Image Anal*, vol. 10, no. 2, pp. 162–177, 2006.

[31] C. Compas, E. Wong, X. Huang, S. Sampath, B. Lin, P. Pal, X. Papademetris, K. Thiele, D. Dione, M. Stacy, L. Staib, A. Sinusas, M. O'Donnell, and J. Duncan, "Radial basis functions for combining shape and speckle tracking in 4D echocardiography," *IEEE Trans Med Imag*, vol. 33, no. 6, pp. 1275–1289, 2014.

[32] V. Tavakoli, N. Bhatia, R. Longaker, M. Stoddard, and A. Amini, "Tissue Doppler imaging optical flow (TDIOF): A combined B-Mode and tissue Doppler approach for cardiac motion estimation in echocardiographic images," *IEEE Trans Biomed Eng*, vol. 61, no. 8, pp. 2264–2277, 2014.

[33] H. Liebgott, A. B. Salem, A. Basarab, H. Gao, P. Claus, J. D'hooge, P. Delachartre, and D. Friboulet, "Tangential sound field oscillations for 2D motion estimation in echocardiography," in *IEEE Int Ultrasonics Symp*, pp. 498–501, 2009.

[34] M. Alessandrini, A. Basarab, L. Boussel, X. Guo, A. Serusclat, D. Friboulet, D. Kouame, O. Bernard, and H. Liebgott, "A new technique for the estimation of cardiac motion in echocardiography based on transverse oscillations: A preliminary evaluation in silico and a feasibility demonstration in vivo," *IEEE Trans Med Imag*, vol. 33, no. 5, pp. 1148–1162, 2014.

[35] M. Wilhelm, L. Roten, H. Tanner, J. P. Schmid, I. Wilhelm, and H. Saner, "Long-term cardiac remodeling and arrhythmias in nonelite marathon runners," *Am J Cardiol*, vol. 110, pp. 1060–1065, 2012.

[36] B. M. Pluim, A. H. Zwinderman, A. van der Laarse, and E. E. van der Wall, "The athlete's heart: a meta-analysis of cardiac structure and function," *Circulation*, vol. 101, pp. 336–344, 2000.

[37] D. Cohen and I. Dinstein, "New maximum likelihood motion estimation schemes for noisy ultrasound images," *Pattern Recogn*, vol. 35, no. 2, pp. 455–463, 2002.

[38] R. H. Byrd, P. Lu, J. Nocedal, and C. Zhu, "A limited memory algorithm for bound constrained optimization," *SIAM J Sci Comput*, vol. 16, no. 5, pp. 1190–1208, 1995.

[39] M. De Craene, S. Marchesseau, B. Heyde, H. Gao, M. Alessandrini, O. Bernard, G. Piella, A. R. Porras, E. Saloux, L. Tautz, A. Hennemuth, A. Prakosa, H. Liebgott, O. Somphone, P. Allain, S. M. Ebeid, H. Delingette, M. Sermesant, and J. D'hooge, "3D strain assessment in ultrasound (Straus): A synthetic comparison of five tracking methodologies.," *IEEE Trans Med Imaging*, vol. 32, no. 9, pp. 1632–1646, 2013.

[40] J. Allard, S. Cotin, F. Faure, P.-J. Bensoussan, F. Poyer, C. Duriez, H. Delingette, and L. Grisoni, "SOFA - an open source framework for medical simulation," in *MMVR 15*, pp. 1–6, 2007.

[41] S. Marchesseau, H. Delingette, M. Sermesant, and N. Ayache, "Fast parameter calibration of a cardiac electromechanical model from medical images based on the unscented transform.," *Biomech Model Mechan*, vol. 12, no. 4, pp. 815–831, 2013.

[42] H. Gao, H. F. Choi, P. Claus, S. Boonen, S. Jaecques, G. Van Lenthe, G. Van der Perre, W. Lauriks, and J. D'hooge, "A fast convolution-based methodology to simulate 2-D/3-D cardiac ultrasound images," *IEEE T Ultrason Ferr*, vol. 56, no. 2, pp. 404–409, 2009.

[43] J. A. Jensen, *Estimation of Blood Velocities Using Ultrasound, A Signal Processing Approach*. Cambridge University Press, 1996.

[44] A. R. Porras, M. Alessandrini, M. De Craene, N. Duchateau, M. Sitges, B. H. Bijnens, H. Delingette, M. Sermesant, J. D'hooge, A. F. Frangi, and G. Piella, "Improved myocardial motion estimation combining tissue Doppler and B-mode echocardiographic images," *IEEE Trans Med Imag*, vol. 33, no. 11, pp. 2098–2106, 2014.

[45] M. Ahmad, "Real-time 3-dimensional echocardiography. technique and clinical applications.," *Minerva Cardioangiol*, vol. 51, no. 6, pp. 635–640, 2003.

[46] M. Ahmad, T. Xie, M. McCulloch, G. Abreo, and M. Runge, "Real-time three-dimensional dobutamine stress echocardiography in assessment of ischemia: comparison with two-dimensional dobutamine stress echocardiography.," *J Am Coll Cardiol*, vol. 37, no. 5, pp. 1303–1309, 2001.

[47] E. Eroglu, J. D'hooge, L. Herbots, D. Thijs, C. Dubois, P. Sinnaeve, J. Dens, J. Vanhaecke, and F. Rademakers, "Comparison of real-time tri-plane and conventional 2D dobutamine stress echocardiography for the assessment of coronary artery disease," *Eur Heart J*, vol. 27, no. 14, pp. 1719–1724, 2006.

[48] N. R. Van de Veire, G. B. Bleeker, C. Ypenburg, J. De Sutter, N. Ajmone Marsan, E. R. Holman, E. E. van der Wall, M. J. Schalij, and J. J. Bax, "Usefulness of tri-plane tissue doppler imaging to predict acute response to cardiac resynchronization therapy.," *Am J Cardiol*, vol. 100, no. 3, pp. 476–482, 2007.

[49] M. D. Cerqueira, N. J. Weissman, V. Dilsizian, A. K. Jacobs, S. Kaul, W. K. Laskey, D. J. Pennell, J. A. Rumberger, T. Ryan, and M. S. Verani, "Standardized myocardial segmentation and nomenclature for tomographic imaging of the heart: A statement for healthcare professionals from the cardiac imaging committee of the council on clinical cardiology of the american heart association," *Circulation*, vol. 105, no. 4, pp. 539–542, 2002.

[50] B. Heyde, D. Barbosa, P. Claus, F. Maes, and J. D'hooge, "Influence of the grid topology of free-form deformation models on the performance of 3D strain estimation in echocardiography," in *FIMH*, vol. 7945 of *LNCS*, pp. 308–315, 2013.

[51] M. Alessandrini, M. De Craene, O. Bernard, S. Giffard-Roisin, P. Allain, J. Weese, E. Saloux, H. Delingette, M. Sermesant, and J. D'hooge, "A pipeline for the generation of realistic 3D synthetic echocardiographic sequences: Methodology and open-access database.," *IEEE Trans Med Imag*, In-press.

[52] J. M. Miller and D. P. Zipes, "Catheter ablation of arrhythmias," *Circulation*, vol. 106, no. 25, pp. 203e–205, 2002.

[53] W. G. Stevenson, "Ventricular scars and ventricular tachycardia.," *Trans Am Clin Climatol Assoc*, vol. 120, pp. 403–412, 2009.

[54] H. E. Botker, J. F. Lassen, F. Hermansen, H. Wiggers, P. Sogaard, W. Y. Kim, M. Bottcher, L. Thuesen, and A. K. Pedersen, "Electromechanical mapping for detection of myocardial viability in patients with ischemic cardiomyopathy.," *Circulation*, vol. 103, no. 12, pp. 1631–1637, 2001.

[55] J. A. Fallavollita, U. Valeti, S. Oza, and J. J. M. Canty, "Spatial heterogeneity of endocardial voltage amplitude in viable, chronically dysfunctional myocardium.," *Basic Res Cardiol*, vol. 99, no. 3, pp. 212–222, 2004.

[56] D. Andreu, A. Berruezo, J. T. Ortiz-Perez, E. Silva, L. Mont, R. Borras, T. M. de Caralt, R. J. Perea, J. Fernandez-Armenta, H. Zeljko, and J. Brugada, "Integration of 3D electroanatomic maps and magnetic resonance scar characterization into the navigation system to guide ventricular tachycardia ablation.," *Circ-Arrhythmia Elec*, vol. 4, no. 5, pp. 674–683, 2011.

[57] J. Gorcsan, "Echocardiographic strain imaging for myocardial viability: An improvement over visual assessment?," *Circulation*, vol. 112, no. 25, pp. 3820–3822, 2005.

[58] H. Samady, Y.-H. Liu, C. Choi, M. Ragosta, S. E. Pfau, M. W. Cleman, E. R. Powers, C. M. Kramer, F. J. Wackers, G. A. Beller, and D. D. Watson, "Electromechanical mapping for detecting myocardial viability and ischemia in patients with severe ischemic cardiomyopathy," *Am J Cardiol*, vol. 91, no. 7, pp. 807–811, 2003.

[59] C. Hoogendoorn, F. M. Sukno, S. Ordas, and A. F. Frangi, "Bilinear models for spatio-temporal point distribution analysis, application to extrapolation of left ventricular, biventricular and whole heart cardiac dynamics," *Int J Comput Vision*, vol. 85, no. 3, pp. 237–252, 2009.

[60] Y. Suh, S. Dieterich, B. Cho, and P. J. Keall, "An analysis of thoracic and abdominal tumour motion for stereotactic body radiotherapy patients," *Phys Med Biol*, vol. 53, no. 13, p. 3623, 2008.

[61] H. C. van Assen, M. G. Danilouchkine, A. F. Frangi, S. Ordás, J. J. M. Westenberg, J. H. C. Reiber, and B. P. F. Lelieveldt, "SPASM: a 3D-ASM for segmentation of sparse and arbitrarily oriented cardiac MRI data.," *Med Image Anal*, vol. 10, no. 2, pp. 286–303, 2006.

[62] P. Besl and N. McKay, "A method for registration of 3D shapes," *IEEE T Pattern Anal*, vol. 14, no. 2, pp. 239–256, 1992.

[63] C. Butakoff, S. Balocco, F. M. Sukno, C. Hoogendoorn, C. Tobon-Gomez, G. Avegliano, and A. F. Frangi, "Left-ventricular epi- and endocardium extraction from 3D ultrasound images using an automatically constructed 3D ASM," *Comput Method Biomec: Imaging & Visualization*, pp. 1–16, 2014.

[64] T. Dickfeld, H. Calkins, M. Zviman, R. Kato, G. Meininger, L. Lickfett, R. Berger, H. Halperin, and S. B. Solomon, "Anatomic stereotactic catheter ablation on three-dimensional magnetic resonance images in real time.," *Circulation*, vol. 108, no. 19, pp. 2407–2413, 2003.

[65] F. E. Marchlinski, D. J. Callans, C. D. Gottlieb, and E. Zado, "Linear ablation lesions for control of unmappable ventricular tachycardia in patients with ischemic and nonischemic cardiomyopathy.," *Circulation*, vol. 101, no. 11, pp. 1288–1296, 2000.

[66] L. Rao, Y. Ling, R. He, A. L. Gilbert, N. G. Frangogiannis, J. Wang, S. F. Nagueh, and D. S. Khoury, "Integrated multimodal-catheter imaging unveils principal relationships among ventricular electrical activity, anatomy, and function," *Am J Physiol-Heart C*, vol. 294, no. 2, pp. H1002–H1009, 2008.

[67] S. A. Reisner, P. Lysyansky, Y. Agmon, D. Mutlak, J. Lessick, and Z. Friedman, "Global longitudinal strain: a novel index of left ventricular systolic function," *J Am Soc Echocardiogr*, vol. 17, no. 6, pp. 630–633, 2004.

[68] S. D. Roes, S. A. Mollema, H. J. Lamb, E. E. van der Wall, A. de Roos, and J. J. Bax, "Validation of echocardiographic two-dimensional speckle tracking longitudinal strain imaging for viability assessment in patients with chronic ischemic left ventricular dysfunction and comparison with contrast-enhanced magnetic resonance imaging," *Am J Cardiol*, vol. 104, no. 3, pp. 312–317, 2009.

[69] R. J. Kim, D. S. Fieno, T. B. Parrish, K. Harris, E. L. Chen, O. Simonetti, J. Bundy, J. P. Finn, F. J. Klocke, and R. M. Judd, "Relationship of MRI delayed contrast enhancement to irreversible injury, infarct age, and contractile function.," *Circulation*, vol. 100, no. 19, pp. 1992–2002, 1999.

[70] A. T. Yan, A. J. Shayne, K. A. Brown, S. N. Gupta, C. W. Chan, T. M. Luu, M. F. Di Carli, H. G. Reynolds, W. G. Stevenson, and R. Y. Kwong, "Characterization of the peri-infarct zone by contrast-enhanced cardiac magnetic resonance imaging is a powerful predictor of post-myocardial infarction mortality.," *Circulation*, vol. 114, no. 1, pp. 32–39, 2006.

[71] E. Wu, R. M. Judd, J. D. Vargas, F. J. Klocke, R. O. Bonow, and R. J. Kim, "Visualisation of presence, location, and transmural extent of healed Q-wave and non-Q-wave myocardial infarction.," *Lancet*, vol. 357, no. 9249, pp. 21–28, 2001.

[72] A. Codreanu, F. Odille, E. Aliot, P.-Y. Marie, I. Magnin-Poull, M. Andronache, D. Mandry, W. Djaballah, D. Régent, J. Felblinger, and C. de Chillou, "Electroanatomic characterization of post-infarct scars comparison with 3-dimensional myocardial scar reconstruction based on magnetic resonance imaging.," *J Am Coll Cardiol*, vol. 52, no. 10, pp. 839–842, 2008.

[73] J. Fernandez-Armenta, A. Berruezo, D. Andreu, O. Camara, E. Silva, L. Serra, V. Barbarito, L. Carotenutto, R. Evertz, J. T. Ortiz-Pérez, T. De Caralt, R. J. Perea, M. Sitges, L. Mont, A. Frangi, and J. Brugada, "Three-dimensional architecture of scar and conducting channels based on high resolution CE-CMR: insights for ventricular tachycardia ablation.," *Circ-Arrhythmia Elec*, vol. 6, no. 3, pp. 528–537, 2013.

[74] B. Desjardins, T. Crawford, E. Good, H. Oral, A. Chugh, F. Pelosi, F. Morady, and F. Bogun, "Infarct architecture and characteristics on delayed enhanced magnetic resonance imaging and electroanatomic mapping in patients with postinfarction ventricular arrhythmia.," *Heart Rhythm*, vol. 6, pp. 644–651, 2009.

[75] S. Gupta, B. Desjardins, T. Baman, K. Ilg, E. Good, T. Crawford, H. Oral, F. Pelosi, A. Chugh, F. Morady, and F. Bogun, "Delayed-enhanced MR scar imaging and intraprocedural registration into an electroanatomical mapping system in post-infarction patients.," *JACC-Cardiovasc imag*, vol. 5, no. 2, pp. 207–210, 2012.

[76] E. Perez-David, A. Arenal, J. L. Rubio-Guivernau, R. del Castillo, L. Atea, E. Arbelo, E. Caballero, V. Celorrio, T. Datino, E. Gonzalez-Torrecilla, F. Atienza, M. J. Ledesma-Carbayo, J. Bermejo, A. Medina, and F. Fernández-Avilés, "Noninvasive identification of ventricular tachycardia-related conducting channels using contrast-enhanced magnetic resonance imaging in patients with chronic myocardial infarction: comparison of signal intensity scar mapping and endocardial voltage mapping.," *J Am Coll Cardiol*, vol. 57, no. 2, pp. 184–194, 2011.

[77] E. Dikici, T. O'Donnell, R. Setser, and R. D. White, "Quantification of delayed-enhancement MR images," in *MICCAI*, vol. 3216 of *LNCS*, pp. 250–257, 2004.

[78] R. Berbari, N. Kachenoura, F. Frouin, A. Herment, E. Mousseaux, and I. Bloch, "An automated quantification of the transmural myocardial infarct extent using cardiac de-mr images.," *IEEE EMBC*, pp. 4403–4406, 2009.

[79] X. Alba, R. M. Figueras i Ventura, K. Lekadir, and A. F. Frangi, "Conical deformable model for myocardial segmentation in late-enhanced MRI," in *IEEE ISBI*, pp. 270–273, 2012.

[80] E. Heiberg, H. Engblom, J. Engvall, E. Hedström, M. Ugander, and H. Arheden, "Semi-automatic quantification of myocardial infarction from delayed contrast enhanced magnetic resonance imaging.," *Scand Cardiovasc J*, vol. 39, no. 5, pp. 267–275, 2005.

[81] Q. Tao, J. Milles, K. Zeppenfeld, H. J. Lamb, J. J. Bax, J. H. C. Reiber, and R. J. van der Geest, “Automated segmentation of myocardial scar in late enhancement MRI using combined intensity and spatial information.,” *Magn Reson Med*, vol. 64, no. 2, pp. 586–594, 2010.

[82] X. Alba, R. M. Figueras i Ventura, K. Lekadir, and A. F. Frangi, “Healthy and scar myocardial tissue classification in DE-MRI,” in *STACOM*, vol. 7746 of *LNCS*, pp. 62–70, 2013.

[83] V. Positano, A. Pingitore, A. Giorgetti, B. Favilli, M. F. Santarelli, L. Landini, P. Marzullo, and M. Lombardi, “A fast and effective method to assess myocardial necrosis by means of contrast magnetic resonance imaging.,” *J Cardiovasc Magn Reson*, vol. 7, no. 2, pp. 487–494, 2005.

[84] T. P. O’Donnell, N. Xu, R. M. Setser, and R. D. White, “Semi-automatic segmentation of nonviable cardiac tissue using cine and delayed enhancement magnetic resonance images,” in *Proc. SPIE*, vol. 5031, pp. 242–251, 2003.

[85] I. Larrabide, P. Omedas, Y. Martelli, X. Planes, M. Nieber, J. Moya, C. Butakoff, R. Sebastian, O. Camara, M. De Craene, B. H. Bijnens, and A. F. Frangi, “GIMIAS: An open source framework for efficient development of research tools and clinical prototypes,” in *FIMH*, vol. 5528 of *LNCS*, pp. 417–426, 2009.

[86] S. Ordas, E. Oubel, R. Leta, F. Carreras, and A. F. Frangi, “A statistical shape model of the heart and its application to model-based segmentation,” in *SPIE*, vol. 6511, 2007.

[87] C. Hoogendoorn, N. Duchateau, D. Sánchez-Quintana, T. Whitmarsh, F. M. Sukno, M. De Craene, K. Lekadir, and A. F. Frangi, “A high-resolution atlas and statistical model of the human heart from multislice CT.,” *IEEE Trans Med Imag*, vol. 32, no. 1, pp. 28–44, 2013.

[88] C. Tobon-Gomez, C. Butakoff, S. Aguade, F. Sukno, G. Moragas, and A. Frangi, “Automatic construction of 3D-ASM intensity models by simulating image acquisition: Application to myocardial gated SPECT studies,” *IEEE Trans Med Imag*, vol. 27, no. 11, pp. 1655–1667, 2008.

[89] C. Tobon-Gomez, F. M. Sukno, C. Butakoff, M. Huguet, and A. F. Frangi, “Automatic training and reliability estimation for 3D ASM applied to cardiac MRI segmentation.,” *Phys Med Biol*, vol. 57, no. 13, pp. 4155–4174, 2012.

[90] K. U. Bauner, O. Muehling, D. Theisen, C. Hayes, B. J. Wintersperger, M. F. Reiser, and A. M. Huber, “Assessment of myocardial viability with 3D MRI at 3 T.,” *Am J Roentgenol*, vol. 192, no. 6, pp. 1645–1650, 2009.

[91] A. Arenal, S. del Castillo, E. Gonzalez-Torrecilla, F. Atienza, M. Ortiz, J. Jimenez, A. Puchol, J. García, and J. Almendral, “Tachycardia-related channel in the scar tissue in patients with sustained monomorphic ventricular tachycardias: influence of the voltage scar definition.,” *Circulation*, vol. 110, no. 17, pp. 2568–2574, 2004.

[92] A. Berruezo, J. Fernández-Armenta, L. Mont, H. Zeljko, D. Andreu, C. Herczku, T. Boussy, J. M. Tolosana, E. Arbelo, and J. Brugada, “Combined endocardial and epicardial catheter ablation in arrhythmogenic right ventricular dysplasia incorporating scar dechanneling technique.,” *Circ-Arrhythmia Elec*, vol. 5, no. 1, pp. 111–121, 2012.

[93] M. D. Hutchinson, E. P. Gerstenfeld, B. Desjardins, R. Bala, M. P. Riley, F. C. Garcia, S. Dixit, D. Lin, W. S. Tzou, J. M. Cooper, R. J. Verdino, D. J. Callans, and F. E. Marchlinski, “Endocardial unipolar voltage mapping to detect epicardial ventricular tachycardia substrate in patients with nonischemic left ventricular cardiomyopathy.,” *Circ-Arrhythmia Elec*, vol. 4, no. 1, pp. 49–55, 2011.

[94] P. Vergara, N. Trevisi, A. Ricco, F. Petracca, F. Baratto, M. Cireddu, C. Bisceglia, G. Maccabelli, and P. Della Bella, “Late potentials abolition as an additional technique for reduction of arrhythmia recurrence in scar related ventricular tachycardia ablation.,” *J Cardiovasc Electr*, vol. 23, no. 6, pp. 621–627, 2012.

[95] L. Tong, H. Gao, and J. D’hooge, “Multi-transmit beam forming for fast cardiac imaging-a simulation study,” *IEEE T Ultrason Ferr*, vol. 60, no. 8, pp. 1719–1731, 2013.

[96] L. Tong, A. Ramalli, R. Jasaityte, P. Tortoli, and J. D’hooge, “Multi-transmit beam forming for fast cardiac imaging - experimental validation and in vivo application,” *IEEE Trans Med Imag*, vol. 33, no. 6, pp. 1205–1219, 2014.

[97] L. Tong, A. Ramalli, G. Fradella, C. Huang, P. Tortoli, J. Luo, and J. D’hooge, “Wide-angle tissue Doppler imaging at high frame rate using multi-line transmit beamforming: An in-vivo pilot study,” in *IEEE Int Ultrasonics Symp Proc*, pp. 1217–1220, 2014.

[98] N. J. Pelc, R. J. Herfkens, A. Shimakawa, and D. R. Enzmann, “Phase contrast cine magnetic resonance imaging,” *Magn Reson Q*, vol. 7, no. 4, pp. 229–254, 1991.

[99] R. Gulrajani, “The forward and inverse problems of electrocardiography,” *IEEE Eng Med Biol*, vol. 17, no. 5, pp. 84–101, 122, 1998.

[100] D. Schwartzman and H. Zhong, “On the use of CartoSound for left atrial navigation,” *J Cardiovasc Electr*, vol. 21, no. 6, pp. 656–664, 2010.

[101] A. C. Kean, S. K. Gelehrter, I. Shetty, I. Dick, Macdonald, and D. J. Bradley, “Experience with CartoSound for arrhythmia ablation in pediatric and congenital heart disease patients,” *J Interv Card Electr*, vol. 29, no. 2, pp. 139–145, 2010.

List of publications

International journal articles:

1. **A. R. Porras**, M. Alessandrini, O. Mirea, J. D'hooge, A. F. Frangi, and G. Piella. Integration of multi-plane tissue Doppler and B-mode echocardiographic images for left ventricular motion estimation. Submitted to IEEE Transactions on Medical Imaging.
2. **A. R. Porras**, M. Alessandrini, M. De Craene, N. Duchateau, M. Sitges, B. H. Bijnens, H. Delingette, M. Sermesant, J. D'hooge, A. F. Frangi, G. Piella. Improved myocardial motion estimation combining tissue Doppler and B-mode echocardiographic images. IEEE Transactions on Medical Imaging, vol. 33, no. 11, pp. 2098-2106. 2014.
3. **A. R. Porras**, G. Piella, A. Berruezo, C. J. Fernandez-Armenta, and A. Frangi. Pre to Intraoperative Data Fusion Framework for Multimodal Characterization of Myocardial Scar Tissue. IEEE Journal of Translational Engineering in Health and Medicine, vol. 2, pp. 1-11. 2014.
4. M. De Craene, S. Marchesseau, B. Heyde, H. Gao, M. Alessandrini, O. Bernard, G. Piella, **A. R. Porras**, L. Tautz, A. Hennemuth, A. Prakosa, H. Liebgott, O. Somphone, P. Allain, S. Makram Ebeid, H. Delingette, M. Sermesant, J. D'hooge, and E. Saloux. 3D Strain Assessment in Ultrasound (Straus): A Synthetic Comparison of Five Tracking Methodologies. IEEE Transactions on Medical Imaging, vol. 32, no. 9, pp. 1632-1646. 2013.
5. **A. R. Porras**, G. Piella, A. Berruezo, C. Hoogendoorn, D. Andreu, J. Fernandez-Armenta, M. Sitges, and A. F. Frangi. Interventional endocardial motion estimation from electroanatomical mapping data: Application to scar characterization. IEEE Transactions on Biomedical Engineering, vol. 60, pp. 1217-1224. 2013.

International conference articles:

1. **A. R. Porras**, M. De Craene, N. Duchateau, M. Sitges, B. H. Bijnens, A. F. Frangi and G. Piella. Myocardial Motion Estimation Combining Tissue Doppler and B-mode Echocardiographic Images. Medical Image Computing and Computer-Assisted Intervention (MICCAI), LNCS, vol. 8150, pp. 484-491, 2013.

2. G. Piella, **A. R. Porras**, M. De Craene, N. Duchateau, A. F. Frangi. Temporal Diffeomorphic Free Form Deformation to Quantify Changes Induced by Left and Right Bundle Branch Block and Pacing. Statistical Atlases and Computational Models of the Heart. Imaging and Modelling Challenges (STACOM'12), LNCS, vol. 7746, pp. 134-141. 2012.
3. **A. R. Porras**, G. Piella, C. Hoogendoorn, D. Andreu, A. Berruezo, A. F. Frangi. Endocardial motion estimation from electro-anatomical data. IEEE International Symposium on Biomedical Imaging (ISBI), pp. 282-285. 2012.
4. **A. R. Porras**, G. Piella, O. Cámara, E. Silva, D. Andreu, A. Berruezo, A. F. Frangi. Cardiac Deformation from Electro-Anatomical Mapping Data: Application to Scar Characterization. Functional Imaging and Modeling of the Heart (FIMH), LNCS, vol. 6666, pp. 47-54. 2011.

National conference publications:

1. **A. R. Porras**, G. Piella, O. Cámara, E. Silva, D. Andreu, L. Mont, A. Berruezo, A. F. Frangi. Análisis de la deformación cardíaca a partir del movimiento de la punta del catéter en los sistemas de navegación. Congreso de la Sociedad Española de Cardiología: El Congreso de las Enfermedades Cardiovasculares. 2011.

Biography

Antonio R. Porras was born in Córdoba, Spain. He graduated of Technical Engineering in Computer Systems in 2006 and Computer Science Engineering in 2008 at the *Universidad de Córdoba*. He obtained his M.Sc. Biomedical Engineering in 2010 at the *Universitat de Barcelona* and *Universitat Politècnica de Catalunya* after an academic stay of 6 months at the Chalmers University of Technology, Gothenburg, Sweden. In 2010, he joined the Center for Computational Imaging and Simulation Technologies in Biomedicine (CISTIB) as a researcher in training and, in 2011, he enrolled in the Ph.D. program of the Department of Information and Communication Technologies, *Universitat Pompeu Fabra*, Barcelona, Spain. His research fields are medical image processing and computer vision.

Appendix: Color figures

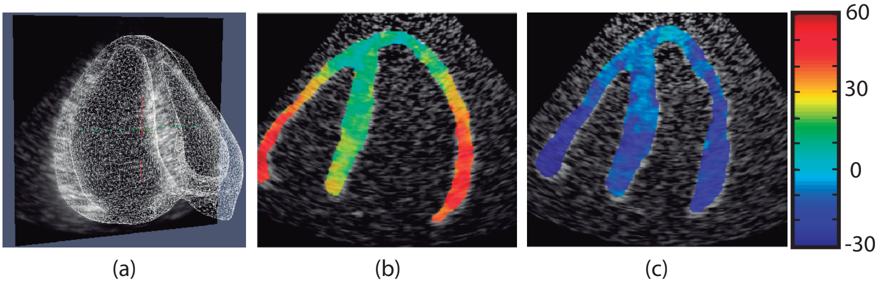

Figure 2.5, page 24: (a) A simulated US frame together with the wireframe of the mesh from the electromechanical model are represented. Example of TD images are shown in (b) early systole and (c) early diastole. Colors represent the velocity in mm/s, which is considered positive when directed towards the transducer.

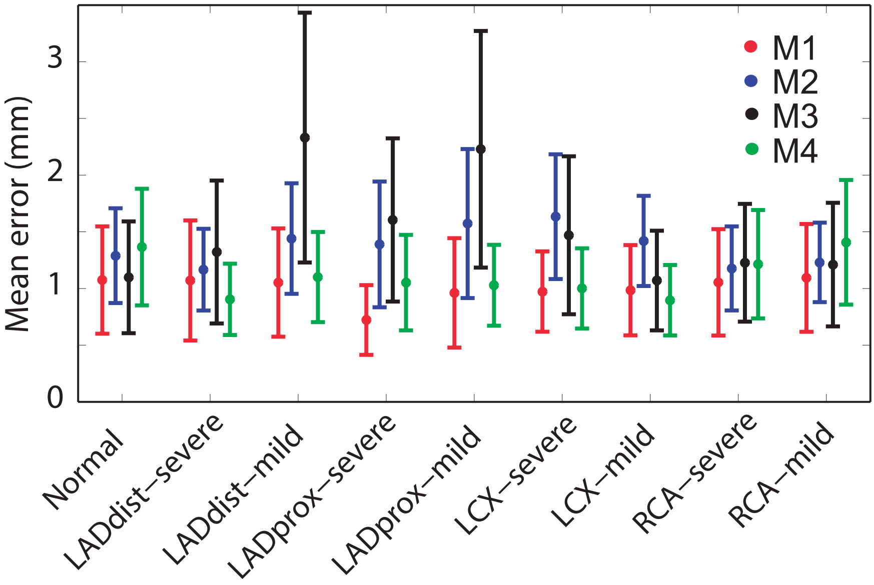

Figure 2.6, page 26: Mean errors (circles) and standard deviations (lines) calculated for the 9 synthetic datasets during one cardiac cycle with the methods summarized in Table 2.1.

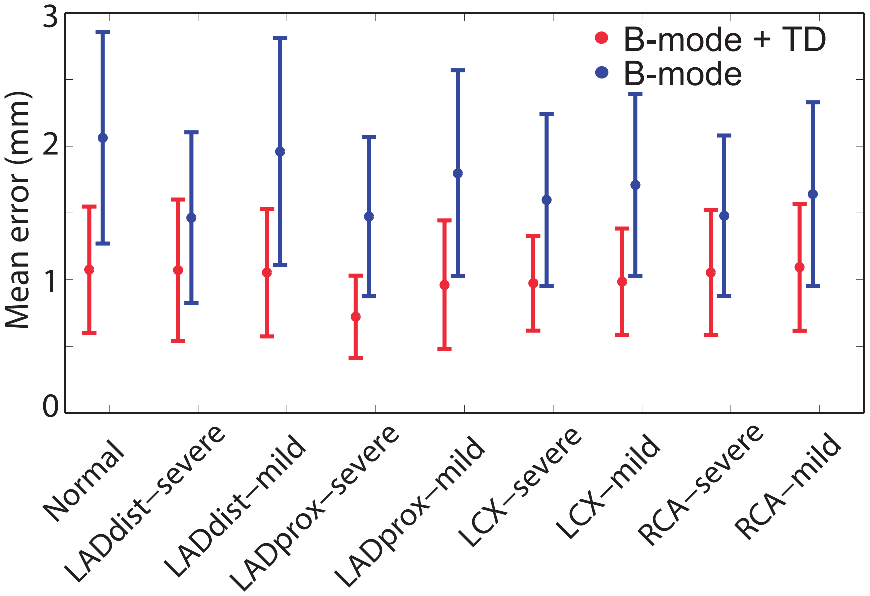

Figure 2.7, page 27: Mean errors (circles) and standard deviations (lines) calculated for the 9 synthetic patients during one cardiac cycle with method M1 (red) and using only B-mode images (blue).

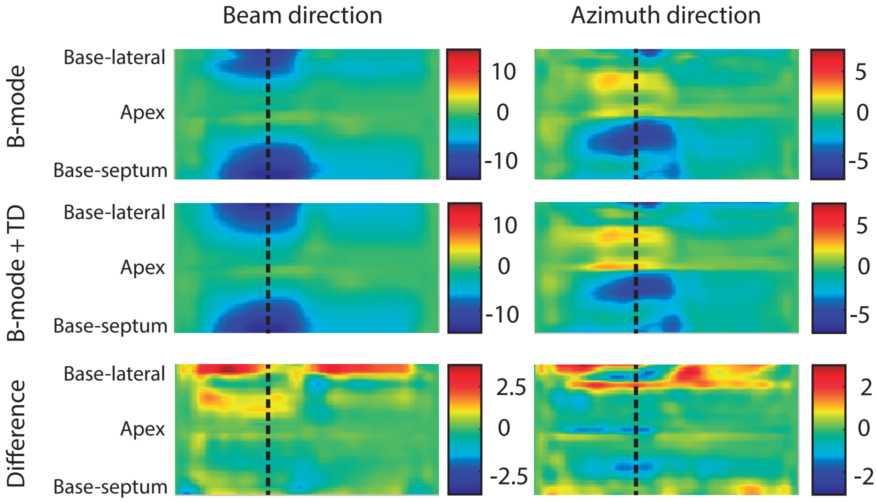

Figure 2.10, page 29: Displacements (in mm) estimated using only B-mode images (top row), using B-mode and TD together (middle row) and the difference between both approaches (bottom row) for one patient at rest.

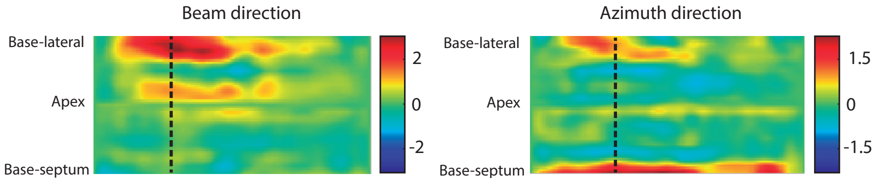

Figure 2.11, page 30: Mean difference between displacements (in mm) estimated using only B-mode and using both B-mode and TD at rest.

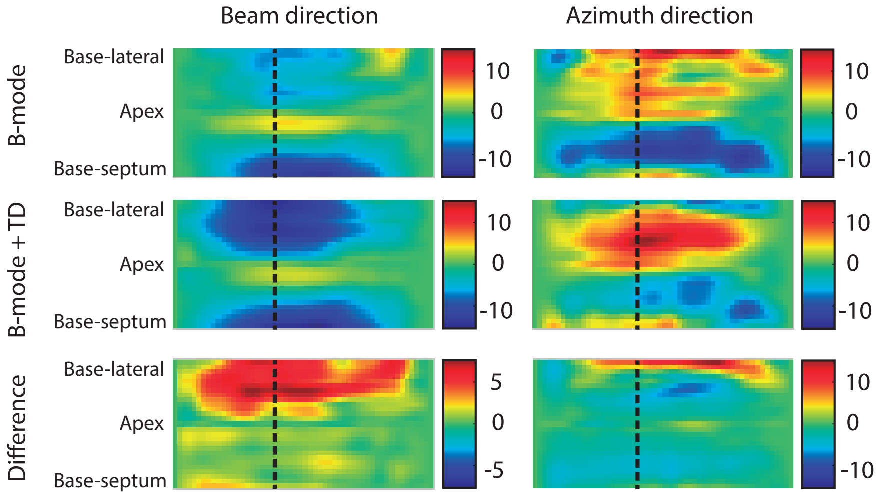

Figure 2.13, page 31: Displacements (in mm) estimated using only B-mode images (top row), using B-mode and TD together (middle row) and the difference between both approaches (bottom row) for one patient during exercise.

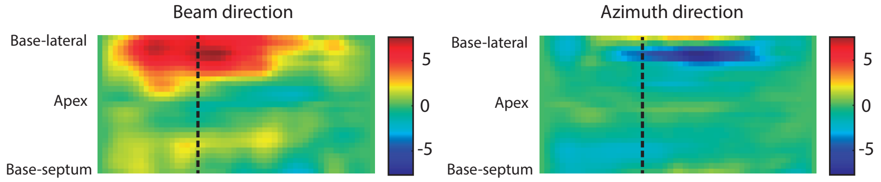

Figure 2.14, page 31: Mean difference between displacements (in mm) estimated using only B-mode and using both B-mode and TD during exercise.

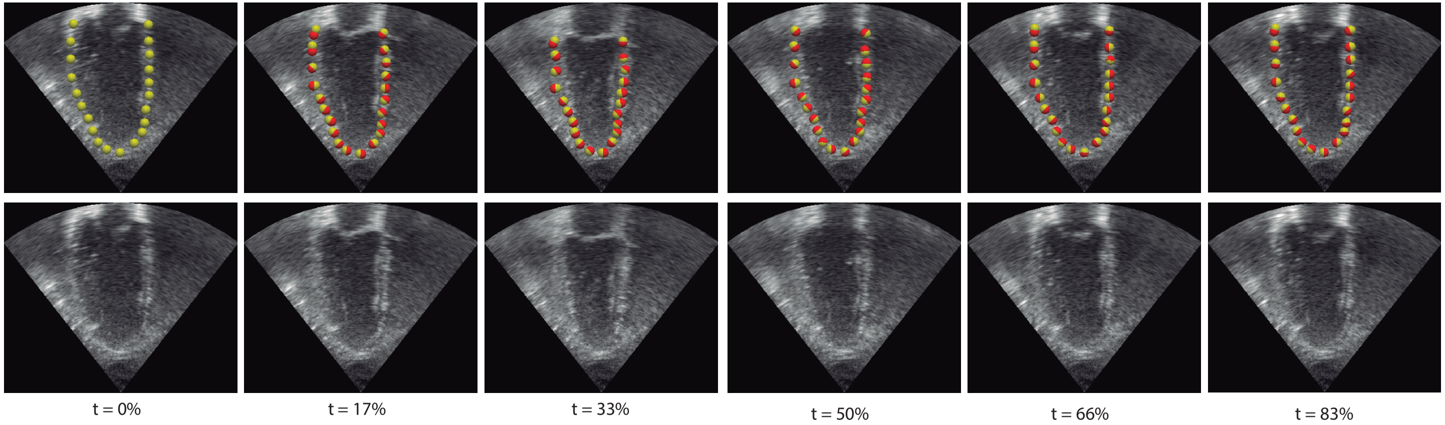

Figure 2.8, page 28: The top row shows a set of landmarks placed on the left ventricle and displaced according to the transformation calculated using only B-mode (yellow), and using both B-mode and TD together (red) at different times of the cardiac cycle for one example patient at rest. The bottom row shows the corresponding B-mode images.

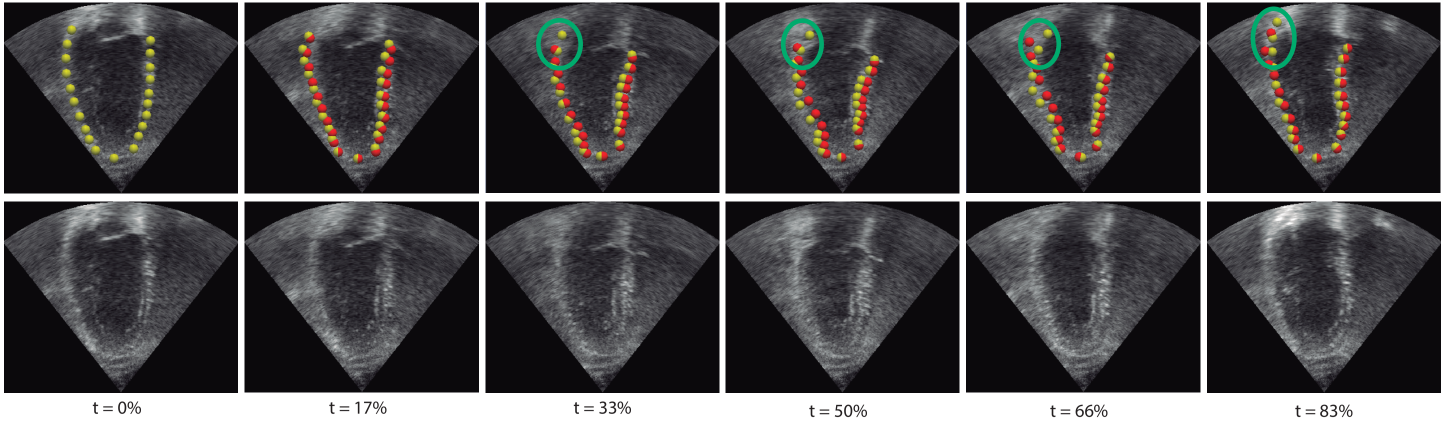
t = 0% t = 17% t = 33% t = 50% t = 66% t = 83%

Figure 2.12, page 30: The top row shows a set of landmarks placed on the left ventricle and displaced according to the transformation calculated using only B-mode (yellow), and using both B-mode and TD together (red) at different times of the cardiac cycle during exercise for the patient in Figure 2.8. Green circles indicate where tracking using B-mode only has problems due to image quality. The bottom row shows the corresponding B-mode images.

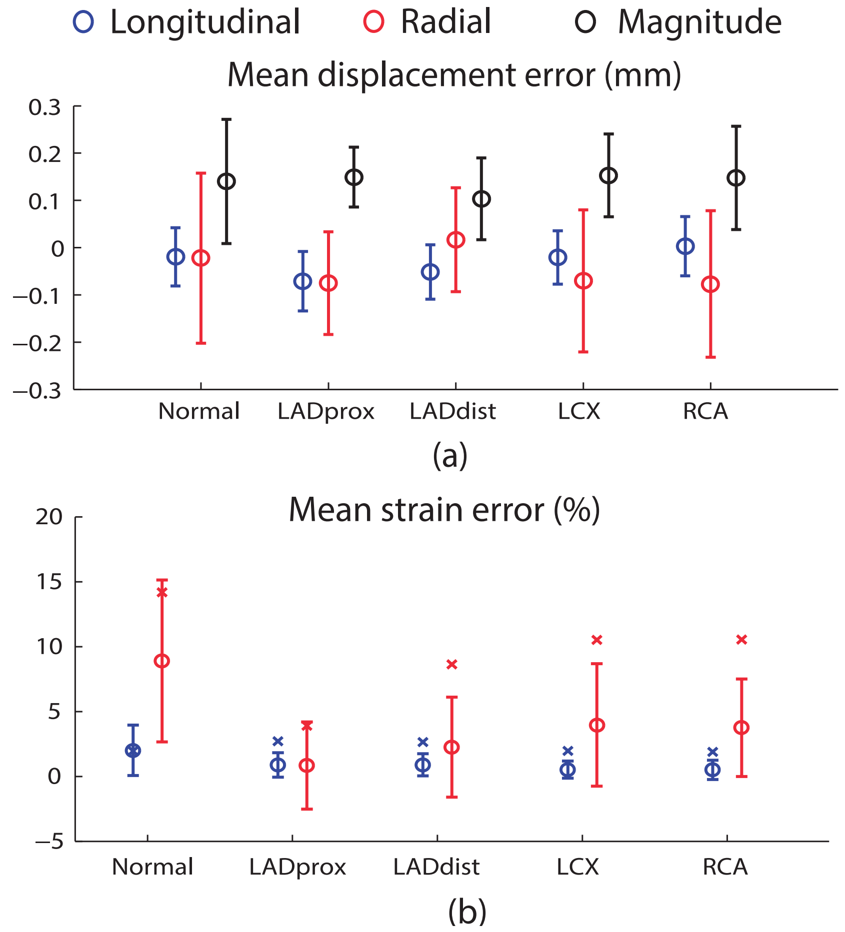

Figure 3.4, page 46: (a) Mean displacement and (b) strain errors and standard deviations for each synthetic case. The crosses in (b) represent the end-systolic strain errors for each case.

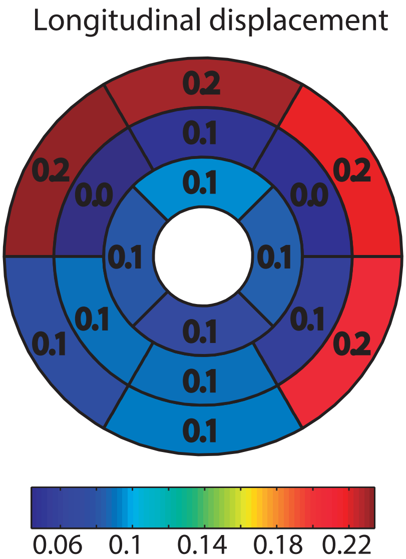

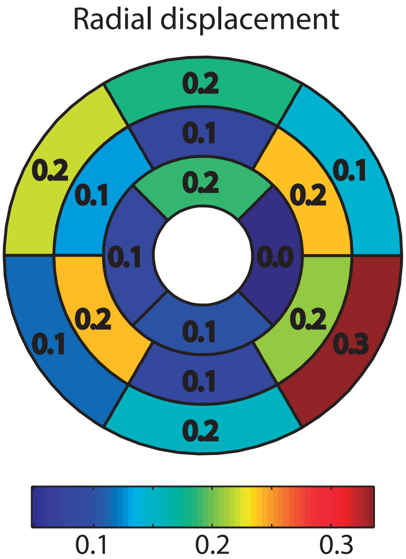

Figure 3.5, page 47: Absolute value of mean displacement errors (mm) averaged for all the synthetic cases.

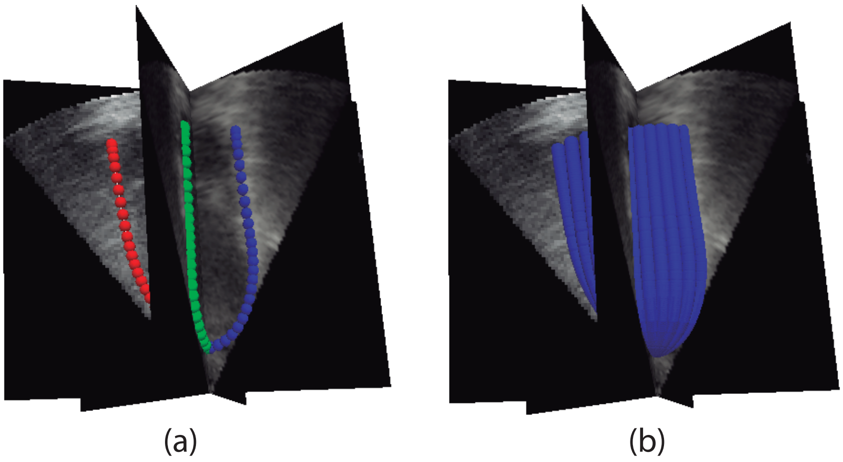

Figure 3.7, page 49: Example of the 3D interpolation to calculate segmental strain and displacements for one patient. (a) shows the initial segmented points at each plane, representing each of the segmentations with a different color. (b) represents the 3D interpolated shape of the left ventricle.

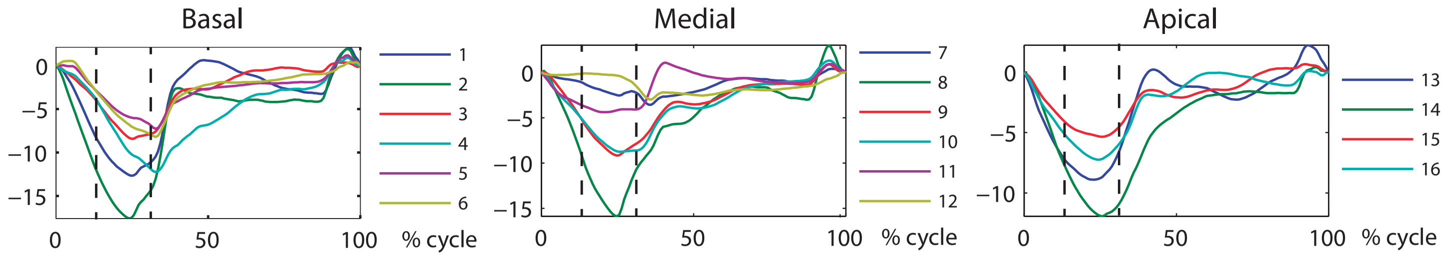

(a) Longitudinal strain curves

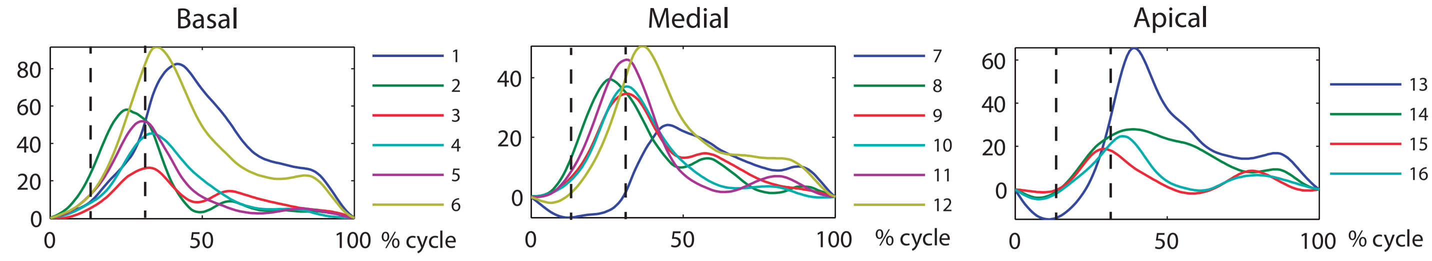

(b) Radial strain curves

Figure 3.8, page 52: (a) Longitudinal and (b) radial strain curves estimated for Case 1 (58 years old patient with ischemia in the infero-lateral wall). For each plot, the first dotted vertical line indicates aortic valve opening, while the second one indicates aortic valve closing.

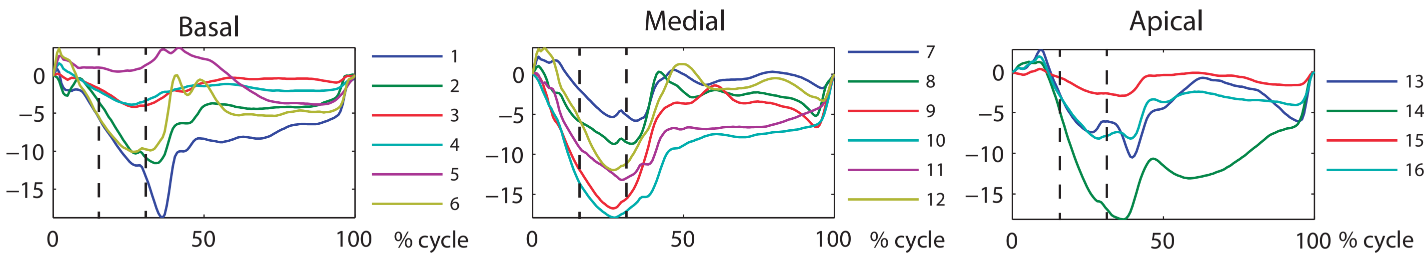

(a) Longitudinal strain curves

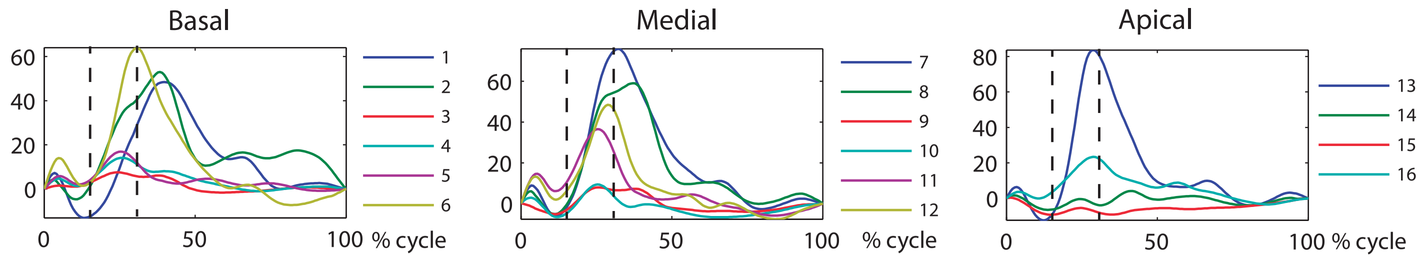

(b) Radial strain curves

Figure 3.9, page 52: (a) Longitudinal and (b) radial strain curves estimated for Case 2 (49 years old patient with ischemia in the inferior wall). For each plot, the first dotted vertical line indicates aortic valve opening, while the second one indicates aortic valve closing.

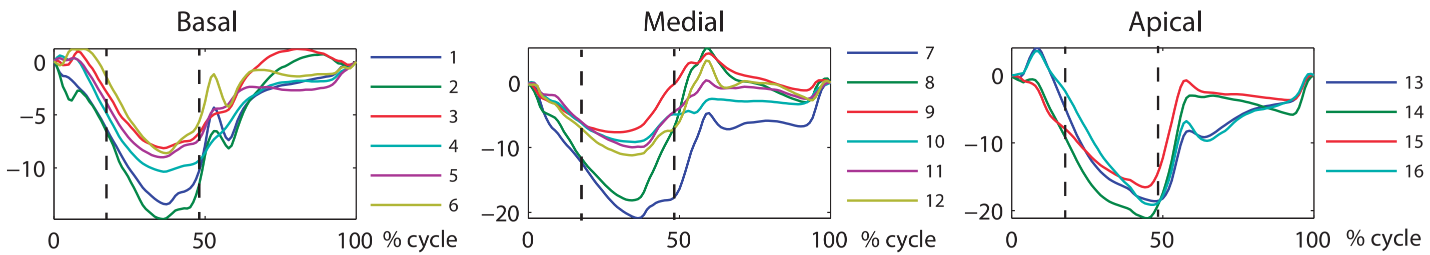

(a) Longitudinal strain curves

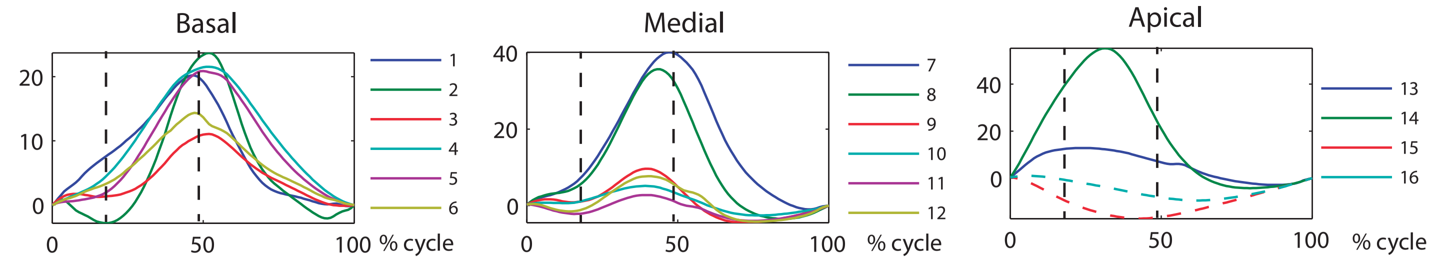

(b) Radial strain curves

Figure 3.10, page 53: (a) Longitudinal and (b) radial strain curves estimated for Case 3 (31 years old healthy volunteer). For each plot, the first dotted vertical line indicates aortic valve opening, while the second one indicates aortic valve closing. Dotted strain curves indicate areas that are not visible in the B-mode image sequence.

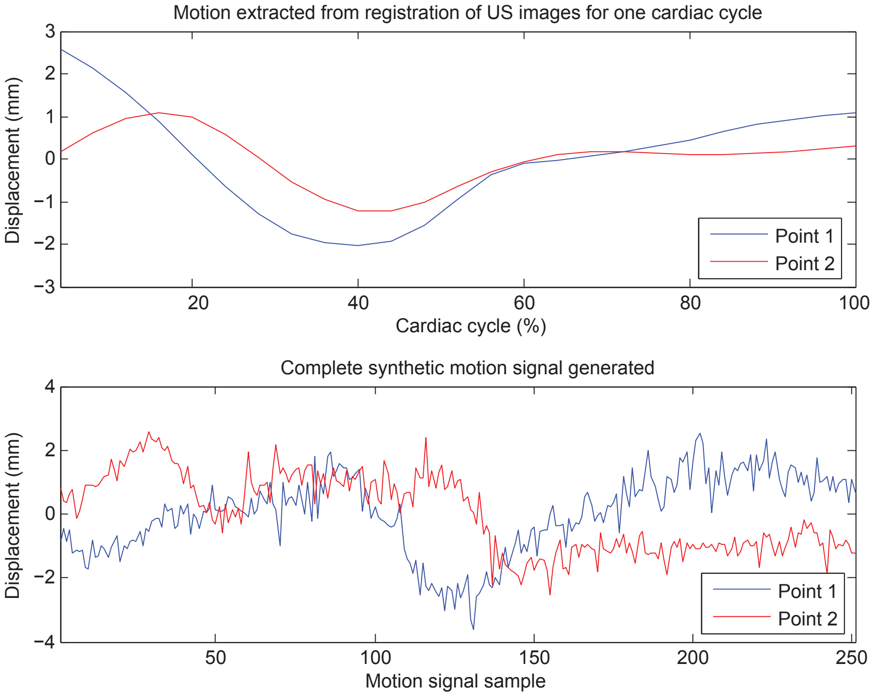

Figure 4.3, page 68: On the top image, motion signals extracted from 3D+t US images for 2 different points. On the bottom image, synthetic motion signals generated with 251 samples for the same points.

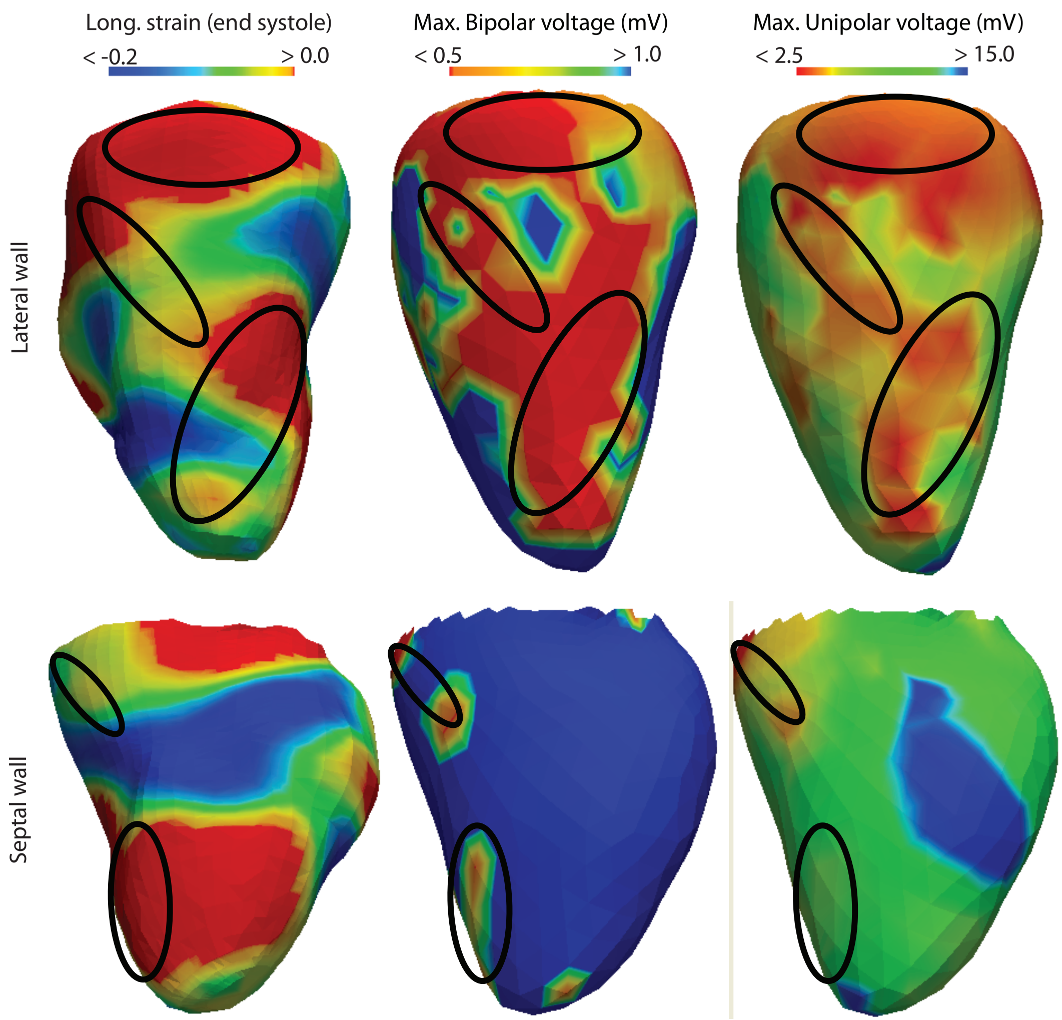

Figure 4.10, page 74: Comparison of longitudinal strain at end systole (left), maximum bipolar (center) and maximum unipolar (right) voltages interpolated at the end-diastolic phase for one ischemic patient. On the top row, a view of the left ventricle from the lateral wall. On the bottom row, a view from the septal wall. Red color represents tissue classified as scar core. Blue color represents tissue classified as healthy. Black oval lines represent the areas where scar core is present according to bipolar thresholds.

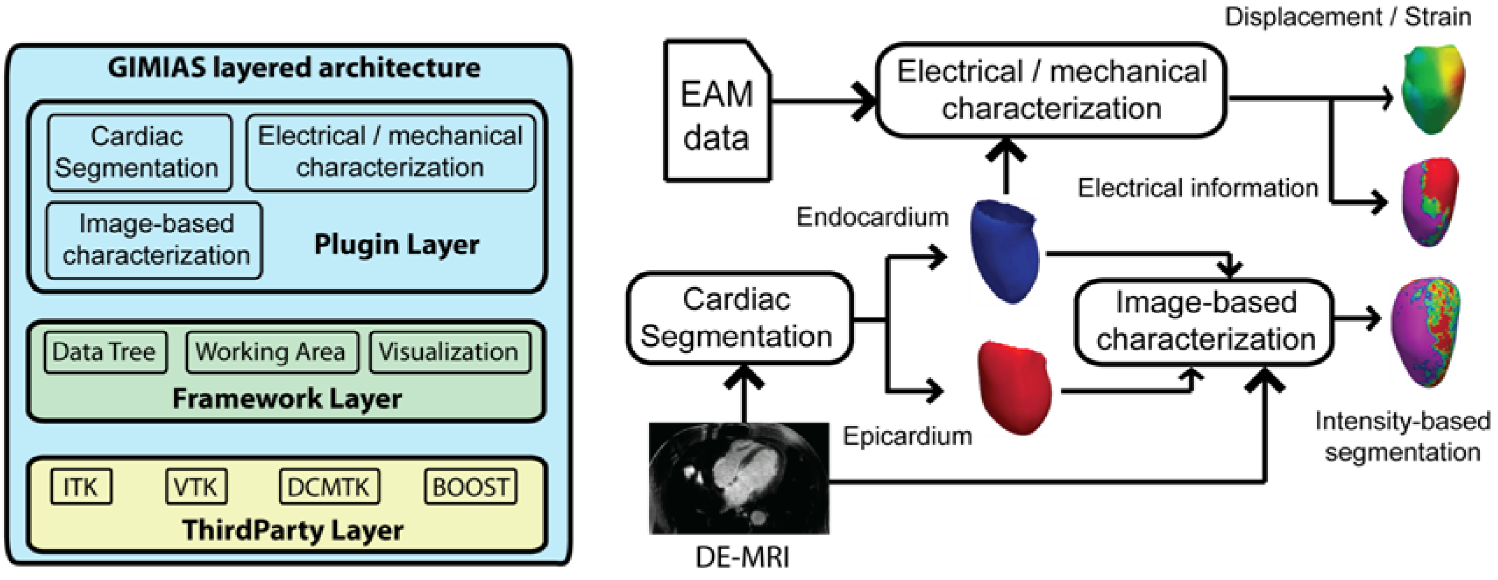

(a) (b)

Figure 5.1, page 84: (a) Layered architecture of GIMIAS. The Plugin layer is on the top and plugins can interoperate through the elements at the framework layer. The Third Party layer is at the bottom, to which all modules have access. (b) Presented pipeline. Both endocardium and epicardium meshes are segmented from DE-MR images using the cardiac segmentation module. The output meshes are used by the image-based characterization module to characterize the scar based on voxel intensities. The segmented endocardium is also used, together with electro-anatomical mapping data, for electrical and mechanical characterization of the left ventricle.

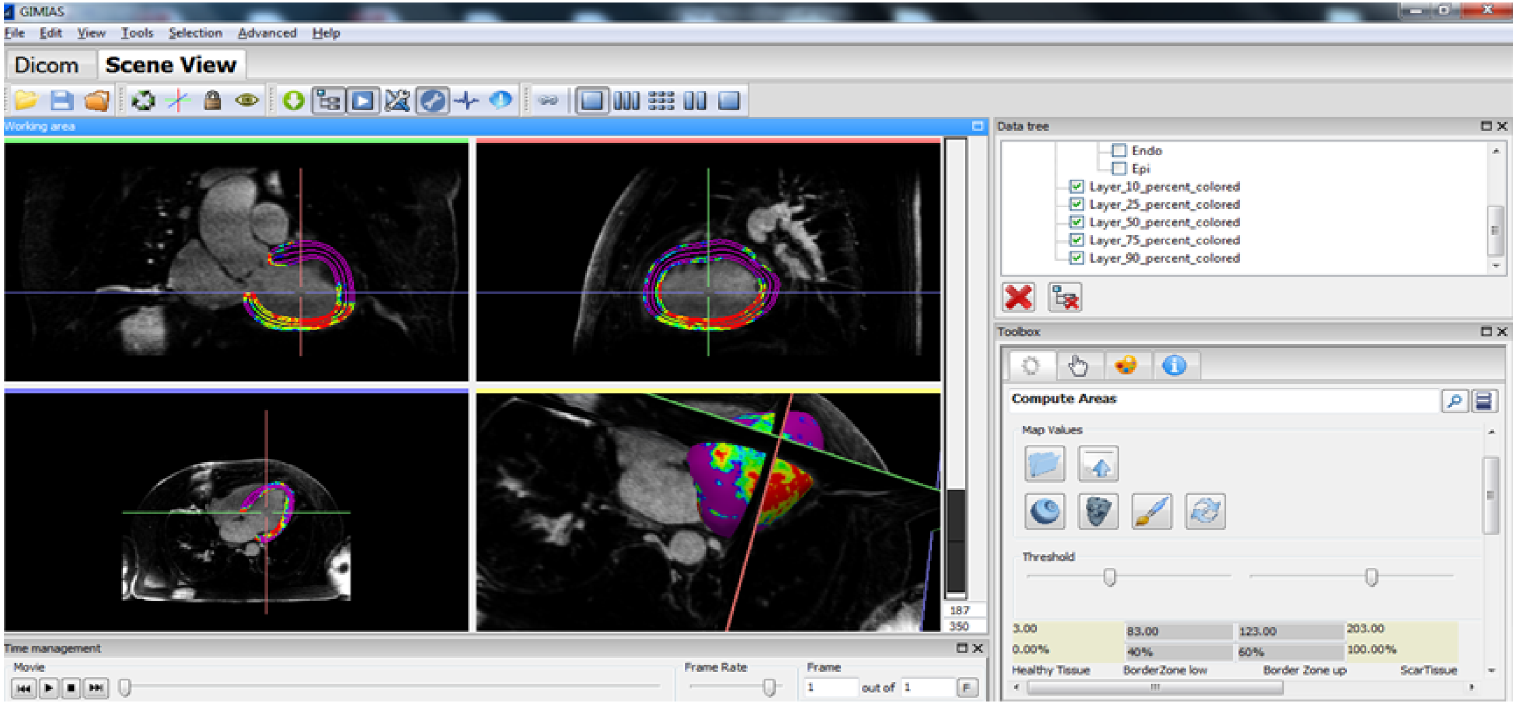

Endo
Epi
Layer_10_percent_colored
Layer_25_percent_colored
Layer_50_percent_colored
Layer_75_percent_colored
Layer_90_percent_colored

Healthy Tissue	BorderZone low	Border Zone up	ScarTissue
3.00	83.00	123.00	203.00
0.00%	40%	60%	100.00%

Frame 1 out of 1

Figure 5.2, page 86: Layers extracted from the left ventricle model segmented with the cardiac segmentation module. Tissue classification based on image intensities is color coded. Red represents dense scar tissue, green represents viable tissue (border zone) and purple represents healthy myocardium.

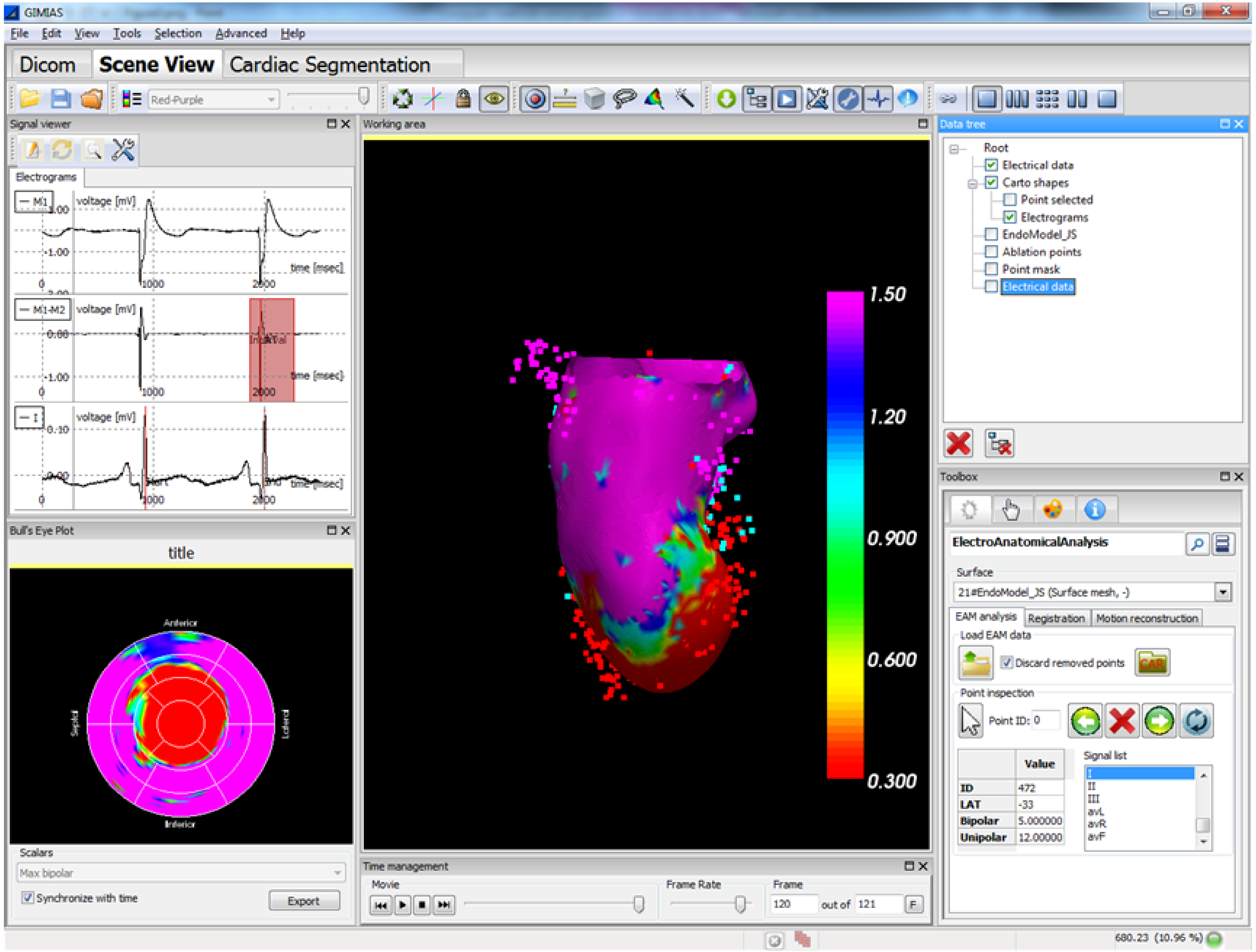

	Value
ID	472
LAT	-33
Bipolar	5.000000
Unipolar	12.00000

Figure 5.3, page 87: Electrical characterization of the tissue. EAM points are registered to the left ventricle endocardium. Electrical parameters derived from the recorded electrograms are interpolated on the mesh. The image shows the maximum bipolar voltage color coded. Purple color represents healthy tissue (> 1.5 mV) and red color represents dense scar (< 0.5 mV). The information is also represented using the 17-segments model proposed by the American Heart Association. Bipolar, unipolar electrograms and superficial ECG (lead I) are also shown in the upper left corner for one selected point.

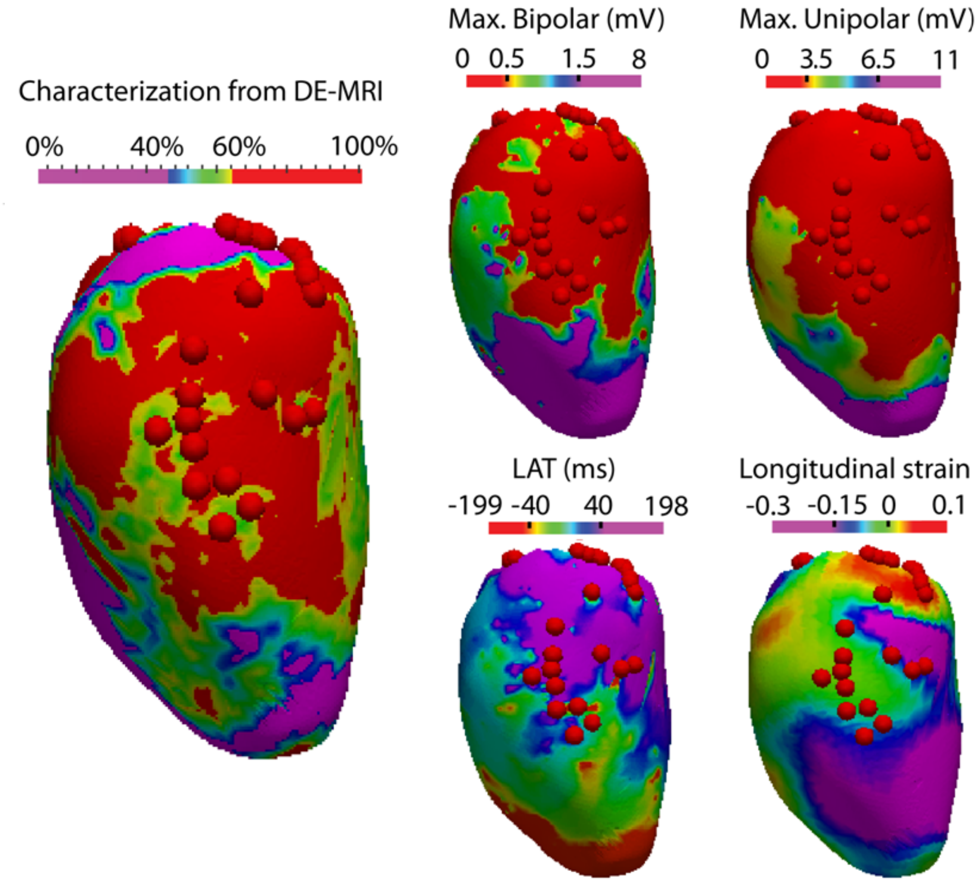

Figure 5.4, page 90: Information integrated by the framework for a 75-year-old man with VT associated with IC. In the scar characterization from DE-MR images, red color represents scar core, purple represents healthy tissue and the rest of the colors represent border zones according to the signal intensity maps. The electrical information is represented by the bipolar voltage map, the unipolar voltage map and the local activation time map. Longitudinal strain calculated at end systole is shown, where negative values represent contraction and positive values indicate stretching. End-systolic strain values are represented on the endocardium at end-diastolic phase to improve visual comparison with the other results. Red spheres represent the ablation targets identified pre-operatively from DE-MR images.

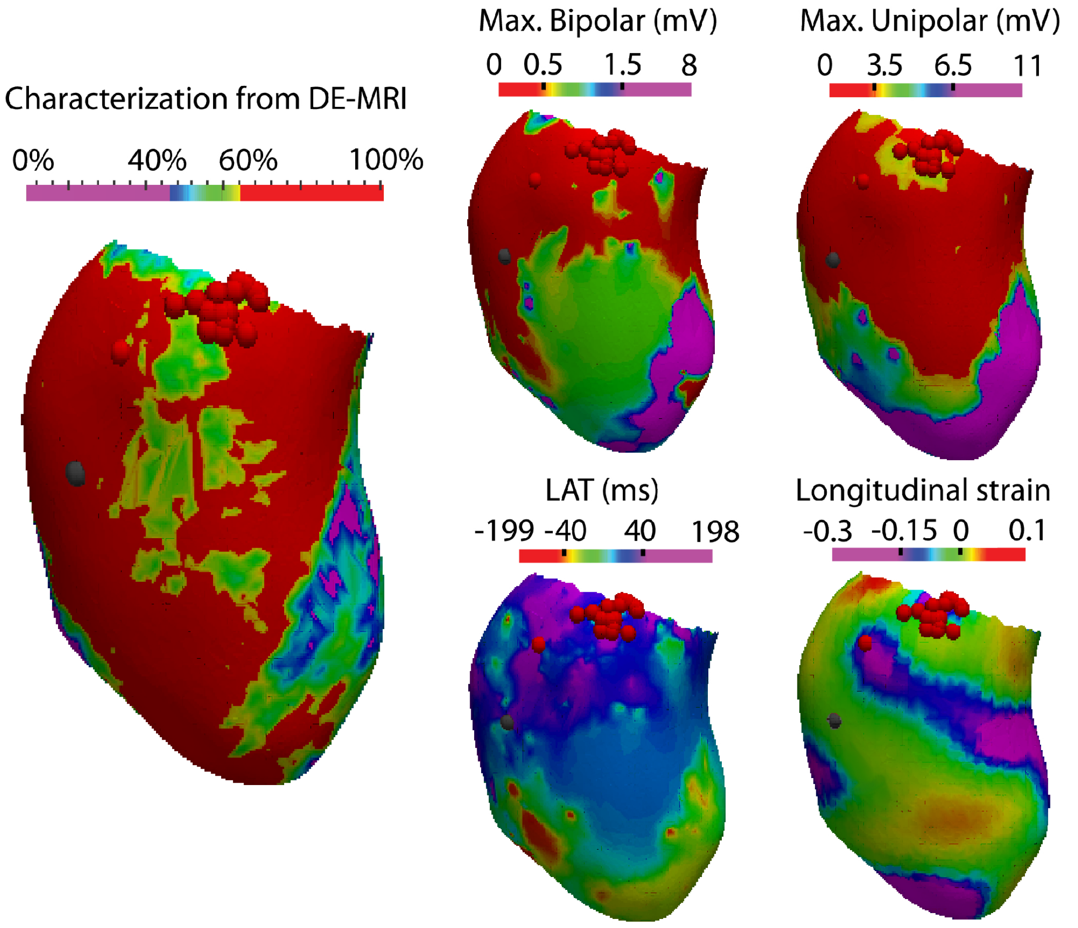

Figure 5.5, page 92: Information integrated by the framework for a 69-year-old man with VT associated to IC. In the scar characterization from DE-MR images, red color represents scar core, purple represents healthy tissue and the rest of the colors represent border zone according to the signal intensity maps. The electrical information is represented by the bipolar voltage map, the unipolar voltage map and the local activation time map. Longitudinal strain calculated at end systole is shown, where negative values represent contraction and positive values indicate stretching. End-systolic strain values are represented on the endocardium at end-diastolic phase to improve visual comparison with the other results. Red spheres represent the ablation targets identified pre-operatively from DE-MR images, while gray spheres represent the ones identified intra-operatively using the electrical maps.

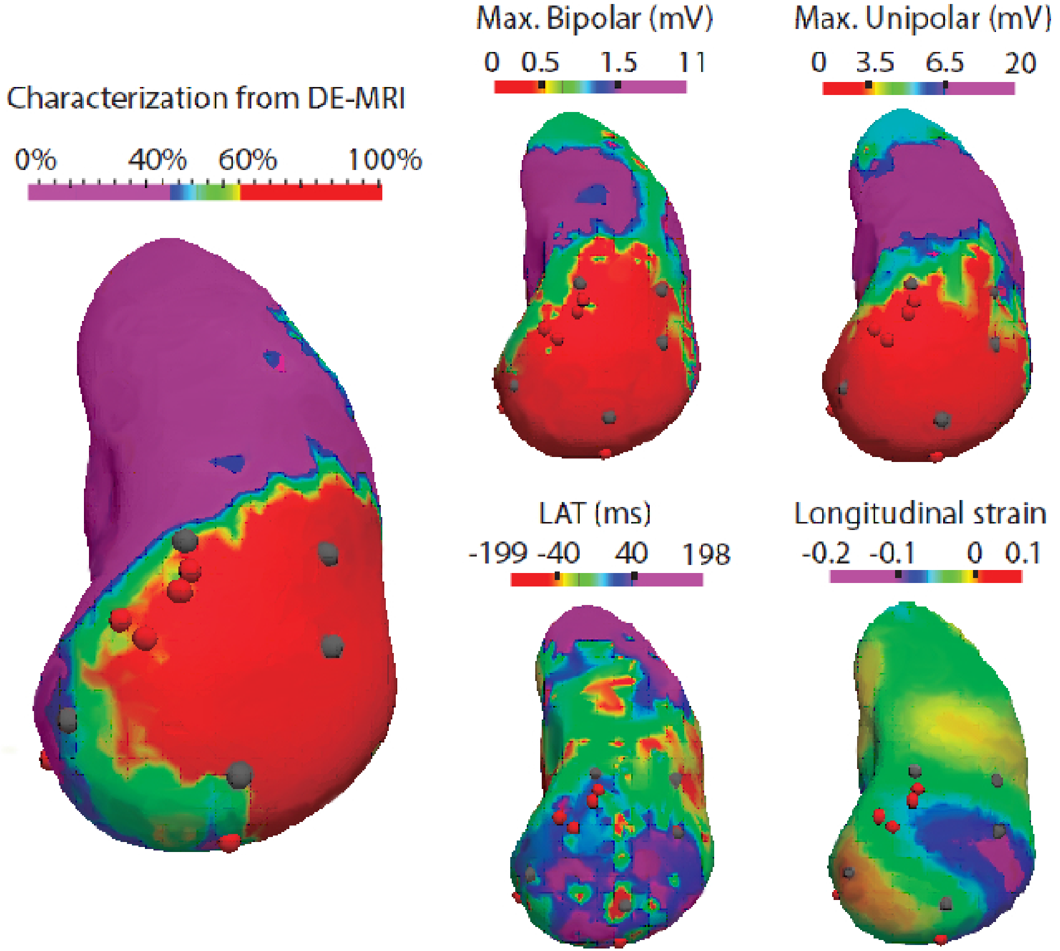

Figure 5.6, page 93: Information integrated by the framework for a 82-year-old man with VT associated to IC. In the scar characterization from DE-MR images, red color represents scar core, purple represents healthy tissue and the rest of the colors represent border zone according to the signal intensity maps. The electrical information is represented by the bipolar voltage map, the unipolar voltage map and the local activation time map. Longitudinal strain calculated at end systole is shown, where negative values represent contraction and positive values indicate stretching. End-systolic strain values are represented on the endocardium at end-diastolic phase to improve visual comparison with the other results. Red spheres represent the ablation targets identified pre-operatively from DE-MR images, while gray spheres represent the ones identified intra-operatively using the electrical maps.